Seismic properties of carbonate rocks with emphasis on effects of the pore structure

Remy Agersborg

Thesis submitted to the University of Bergen towards the fulfilment of the requirements for the Ph.D. degree.

Department of Earth Science
and
Centre for Integrated Petroleum Research
University of Bergen

April 13, 2007

Preface

This Ph.D. thesis counts for four papers written in the period from December 2002 to January 2007. The following introduction will give a short description of the geology, the acoustic observations and the theory of the models used in the papers.

The work with all papers is done at the Centre for Integrated Petroleum Research (CIPR) and Department of Earth Science (DES) at the University of Bergen. The project was financed by Hydro. The project leader has been Professor Tor Arne Johansen at DES with co-supervisor associate Professor Morten Jakobsen. The title of this thesis was defined by Professor Tor Arne Johansen.

The preliminary results from paper 1 were presented at SEG conference in Houston 2005, and submitted in Geophysical Prospecting 2007. The preliminary results from paper 2 were presented in the workshop "Sound of Geology" in Bergen 2006 and submitted to Geophysics 2007. Paper 3 was presented at "workshop meeting on seismic waves in laterally inhomogeneous media VI" in Czech Republic 2005 and published in Studia Geophysica et Geodaetica 2007. Paper 4 is submitted to Journal of Seismic Exploration.

I would like to express my gratitude to my supervisors Professor Tor Arne Johansen and associate Professor Morten Jakobsen for stimulating discussions and guidance during the work with my thesis. I would also like to thank Dr.Philos. Bent Ole Ruud for sharing his knowledge and giving me ideas and suggestions. I am thankful for the finical support which has been provided by Hydro. Erling Jensen is acknowledged for always having time to discuss technical computer issues. Past colleague and now good friend Anders Dræge is also appreciated for fruitful discussions on various topics of my work. Last but not least, I would like to thank my family for their support and encouragement and especially, my two children, Anton and Elias for sharing their curiosity to everything and always giving me a good time together with them.

Remy Agersborg
Bergen, April 13, 2007

Contents

1 Introduction

Understanding the seismic properties of carbonate rocks are important in the exploration both before and during production of hydrocarbons since more than half of the world's hydrocarbon reservoirs are found in these rocks. Today, there are hydrocarbon producing carbonate reservoirs in Canada, the North Sea, Russia, the Middle East and Africa amongst others. Exploration of these reservoirs have high priority because the challenges with these rocks are huge with respect to recovery of hydrocarbons.

Carbonate reservoirs deviate from sandstone reservoirs in many ways. Siliciclastic rocks are formed when sediments are transported, deposited and lithified or compacted and cemented to solid rocks. Most carbonates develop from biological sediments of coral reefs or accumulation of dead organisms on the seafloor. Fragments of carbonates are mostly formed in situ or near by the deposition. When first deposited, carbonates are highly porous and permeable and because they are less chemically stable than silica, carbonates may undergo significant changes under diagenesis. Diagenesis may start at the same time as deposition. Processes such as cementation, dissolution, compaction and dolomitization can dissolve grains and make new pores. Solutions of fracture boundary surfaces can build vugs and caves or cementation of pores may lead to the complex pore structure of this rock.

When an acoustic wave is propagating through a sedimentary rock, the wavelength is much greater than the size of the pores and the grains in the rock. This implies that the wave only can sense the average or effective properties of the rock. However, when probing the rock for the underlying structure and fluid content of the pores, the average properties will of course depend on all this, and the aim of rock physics modelling is to couple these average properties to the underlying microstructure of the rock. Obviously, the overall elastic properties of the rock will depend on the distribution of the mineral constituents

and the porosity. While elastic properties of the minerals are reasonably well understood, the challenges of the rock physics models are to describe the porosity and the geometry of the constituents in the rock. The geometry, shape and distribution of the pores and the grains in the rock may give a large variability in the observable parameters of the acoustic wave. If the microstructure in the rock has a preferred direction, the average response will be anisotropic. Phenomena such as wave-induced fluid flow, or squirt flow, can occur at different frequencies if the porosity consists of cracks or compliant pores. Also how the cavities are connected and fluid content will affect the acoustic properties.

For most rock physics models developed the total porosity and mineral compositions of the rock are emphasized and generally, this is often proven to be enough when describing siliciclastic rocks. These models can be divided into three general classes: Heuristic, empirical and theoretical (Avseth et al., 2005). The most used heuristic model is the time average equation (Wyllie et al., 1956) which relates the P-wave velocity and porosity to the rock. This relation can not be justified theoretically, but it is often used to estimate the seismic velocities or to estimate the porosity from seismic velocities when mineralogy and pore fluid is known. Also, empirical models (such as e.g. Castagna et al., 1993) have proven to be a good tool for estimating the unknown parameters of measurements. The approach is to assume a polynomial function and through regression analysis find the coefficients to the trends of the rock under consideration. One of the most used theoretical model for estimating the seismic velocities or fluid contents in the rocks are the Gassmann equation (Gassmann, 1951). This is a zero frequency model and can be extended to all frequencies by the poroelastic model of Biot (1956a,b). As the frequency of the wave is increasing, there are numerous theories which try to explain phenomena such as the wave-induced fluid flow or squirt flow. Often, the approximations of these theories are violated for carbonate rocks and we have to be careful when using them.

From measurements of core plugs we can learn in more detail about the properties of

the rock. By studying pressure dependent ultrasonic velocities data with different fluids, it is possible to determine a model of the pore types, as compliant pores or cracks are closing with raising pressure and stiffer the rock. By measuring velocities for different angles the anisotropy of the microstructure can be established and by measuring the velocities for different fluid saturations the effects of fluid can be found.

For carbonate rocks, studies have shown that the established rock physics models do not always give satisfying predictions of the velocities (Adam et al., 2006; Anselmetti and Ebreli, 1999; Assefa et al., 2003; Baechle et al., 2005; Rossebø et al., 2005; Wang, 1997,2000). The high-frequency inclusion based model of Kuster and Toksöz (1974), which considers isolated pores, has reproduced laboratory measurements (Toksöz et al., 1976; Wang, 1997). However, when considering ultrasonic experiments where the squirt flow mechanism can be prominent, we have to consider other models. The aim of this Ph.D. study is to investigate the seismic properties of carbonate rocks which are known for the complex pore structure and texture (Eberli et al., 2003), with use of recently developed formulae for deformation of communicating and interacting cavities, the T-matrix approach of Jakobsen et al. (2003a,b). In section 2 the geological aspects and in section 3, the acoustic observations of carbonate rocks are discussed. In section 4, the parameters which had most focus in this study are discussed. The four papers can be found in sections 5 to 8, followed by a short summary of the thesis in section 9.

In paper 1 we have studied the effect of how the cavities are connected with respect to fluid flow on the seismic properties of carbonate rocks. The study concerns a dual porosity model where the cavities can exist on two scales and how the different characteristic pore types of carbonate rocks (Choquette and Pray, 1970) can be described in virtue of a visco-elastic effective medium theory (Jakobsen et al., 2003a,b).

The concept of the dual porosity model was in paper 2 applied on pressure dependent velocity and attenuation data of calcite core plugs. The cavities were on the same scale and

in this study a method for finding the model of the pore structure was developed. By using a distribution of cracks and a dual porosity model, where the smaller pores and cracks in the core plugs contained residual water, it was shown that this model could reproduce the dry measured P- and S-wave velocities and attenuations caused by wave-induced fluid flow.

In paper 3 fractures in a carbonate reservoirs were discussed. By using an expression derived by Chapman (2003), which relates the relaxation time parameter for the fractures to the relaxation time of the microstructure, combined with formulae for inclusions undergoing deformation (Jakobsen and Johansen, 2005), it was shown that the fractures may cause wave-induced fluid flow even at seismic frequencies when the effective pressure was changing. The visco-elastic effective stiffness tensor was then applied in a finite difference code to investigate the seismic signature of the reservoir as the effective pressure was changing.

Paper 4 considers a 2-layer model consisting of a cap rock of shale and some of the reservoir models from paper 1. When injecting a fluid in a reservoir for maintaining the pore pressure, the introduced fluid may alter the connectivity of the pores and/or due to capillary forces flood certain scales before others. The focus was on how the various pore to pore connectivities and different fluids in the porosity systems of two scales affected the Amplitudes Versus Angle parameters. The study indicated that it should be possible to determine directly or indirectly from the reflection coefficients how the injected fluid is distributed in the pore systems of the reservoir or which scale the pore to pore connectivity is altered.

2 The geology of carbonates

If carbonate sediments are formed at the time of deposition and not much modified by later diagnesis, the resulting pore system may closely resemble that of many well sorted sandstones. However, this is unusual and much greater complexity in the pore space is the general rule (Choquette and Pray, 1970). The diagenesis of carbonates involves many different processes and takes place in near-surface marine down into the deep burial environments. It is the most important in occluding and generating porosity in the sediments (Tucker, 2001). Carbonate rocks are sensitive to post-depositional diagnesis which involves processes such as dissolution, cementation, compaction and dolomitization. The unstable carbonate mineral aragonite can convert to more stable calcite which again can be dolomitized. Just after carbonate sediments are deposited, the porosity is commonly of 40-70%, while ancient carbonates with more than a few percent porosity are rare. The porosity is lost through cementation and compaction and gained through dissolution, dolomitization and fracturing. In carbonate sediments porosity can be divided into primary and secondary porosity depending on how it originated. Primary porosity is porosity formed during final sedimentation and includes all pre-depositional and depositional porosity of a particle, sediment or rock while secondary porosity is formed in sediment or rock subsequently to final deposition (Choquette and Pray, 1970).

The most important and frequently observed pore types of primary origin are intercrystaline and interparticle porosity which denote porosity between crystals and particles, respectively (Wang, 1997). These types can occasionally be of secondary origin. Interparticle porosity is the dominant type of porosity in most carbonate sediments (Choquette and Pray, 1970) and such pores are usually irregular and angular in shape so they are easy to deform (Wang, 1997). In terms of seismic velocities, carbonate rocks with these pore types have relatively low velocities and they are strongly dependent on pressure. Intra-

particle porosity is also formed before deposition and is porosity within individual grains and particles. It is abundant in carbonate sediments and can play an important part in the preserved porosity of carbonate rocks (Choquette and Pray, 1970). Intraparticle porosity origins from internal chambers or openings within skeletal organisms and secondary intrapaticle porosity are formed from solution and borings. These pores are hard to deform and carbonate rocks consisting of intraparticle pores generally gives high velocities and are insensitive to pressure (Wang, 1997).

Secondary porosity such as moldic pores are normally formed by solution of individual constituents such as shells, grains, salt or plant roots. They are regular in shape and hard to deform. This implies in terms of seismic properties, high velocities and resistance to pressure changes. Vugs have had the most widely definitions and usage (Choquette and Pray, 1970). Most vugs are formed from solution enlargements and can vary from 1/16 mm to 256 mm in size (Choquette and Pray, 1970). Vugs are equant according to the definition of Choquette and Pray (1970) which gives generally high velocities and low pressure dependency. If the pores are elongated or openings in the rock are irregular and elongated, then they are defined as channel porosity (Choquette and Pray, 1970). Channel porosity originates by solutions along fractures systems or enlargement of other types of pores and is easy to deform. This gives low velocities and carbonates consisting of channel porosity will be relatively sensitive to pressure. Finally, the pore type which might have the largest impact on seismic velocities is fracture porosity. Fractures are formed through tectonic pressure and through collapse and brecciation of carbonate rocks. The presence of fractures may make the rock anisotropic and the velocities will depend on the direction of the wave propagation relative to the directions of the fractures. If the fractures are randomly oriented the rock will be isotropic. Fractures contribute little to the total porosity and are easy to deform which will make the velocity very sensitive to pressure changes (Wang, 1997).

Only the important and commonly observed pore types are listed here and these pore types can coexist in carbonate rocks which contribute to the complexity of the pore space of such rocks. Generally, the most compliant pores control the pressure dependency of the velocities and the compressibility of the rock.

3 Seismic observations of carbonate rocks

The most controlling factor for seismic and sonic velocities is probably the porosity and perhaps equally important for carbonate rocks, the pore types (Eberli et al. 2003). P-wave velocity versus porosity from Eberli et al. (2003) is plotted for different pore types in Figure 1. As the figure shows, there is a large scatter of P-wave velocities around the exponential best fit curve with a difference of about of 2500 m/s between the extreme values at 40% porosity. The study of limestones by Assefa et al. (2003) shows also this

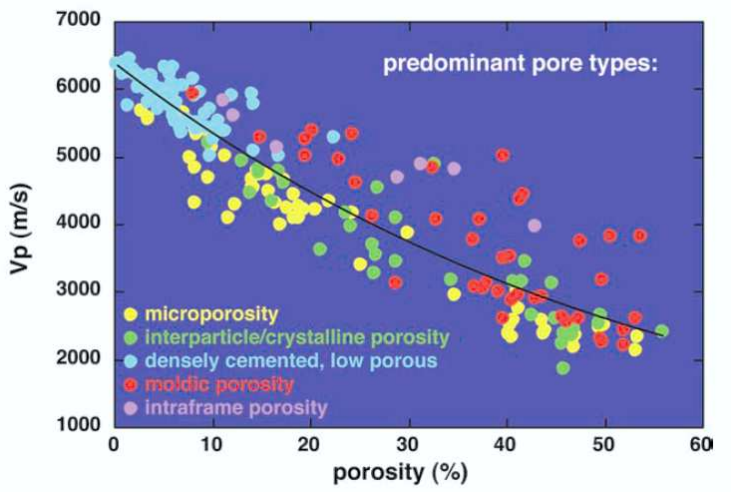

Figure 1: P-wave velocity versus porosity for different pore types of carbonates at 8 MPa effective pressure (from Eberli et al., 2003).

scattering for both the P- and S-wave velocities for equal porosities. The different pore types in carbonate rocks are evident from measured pressure dependent velocities. As the effective pressure, which is the difference between the confining pressure and pore fluid pressure, increases, the compliant pores and cracks will eventually close, causing the velocity to increase. Several carbonate core plug studies have shown great variation in how the velocities increases with increasing effective pressure (Nur and Simmons, 1969; Anselmetti and Eberli, 1999; Wang, 1997; Baechle et al., 2005; Adam et al., 2006).

Another observation of carbonate rocks is the shear weakening and strengthening. Since the S-wave is not very sensitive to the pore fluid, it is often assumed that the shear modulus of the dry and fluid saturated rock is equivalent. Shear weakening is defined as the saturated shear modulus being lower than the dry shear modulus. Shear strengthening is defined as the saturated shear modulus being larger than the dry shear modulus. In several carbonate studies changes of 5% up to 20% in shear modulus have been observed for brine or water saturated core plugs compared to the dry ones (Assefa et al., 2003; Baechle et al., 2005; Rossebø et al., 2005; Adam et al., 2006). The cause of this phenomena is ambiguous. Adam et al. (2006) found that surface energy reductions and crack growth will weaken the shear modulus, while modulus dispersion due to local or global flow will strengthen the shear modulus. Baechle et al. (2005) associated carbonate core plugs containing intercrystaline or interparticle pore types to have extremely high shear modulus variations. Grainstones, which is defined as mud-free grain-supported carbonates (Dunham, 1961), with lots of microscopic porosity have shown shear modulus weakening, while recrystallized limestones with large grain to grain contact areas have shown shear modulus strengthening (Baechle et al., 2005). Chemical interaction between the rock and the pore fluid is also a mechanism which can alter the properties of the rock. The pore fluid can either soften the rock or alter the porosity trough dissolution of the carbonate minerals and cementations.

When comparing ultrasonic with seismic measurements, we have to consider modulus dispersion. Especially for carbonates which often consist of cracks and compliant pores, wave-induced fluid flow (local flow or squirt flow) can alter the moduli at ultrasonic frequencies. In paper 2 of this thesis it was observed that attenuations of the dried core plugs were caused by the squirt flow mechanism. This indicated there was significant residual fluid in the so-called dry core plugs and gave a modified dry bulk and shear modulus for the samples. If there were not measured any attenuations, the moduli found could be

wrongly interpreted as the dry ones. So the wave-induced fluid flow is maybe the most important mechanism for carbonate rocks. Also, this mechanism can dominat at ultrasonic frequencies whereas other mechanisms can arise at low frequency measurements. This is observed in the study of Adam et al. (2006) where shear weakening is observed for 100 Hz measurements whereas the opposite was observed for 8 kHz measurements. Also when the rock consists of fractures or very large compliant cracks or pores, wave-induced fluid flow can even occur at seismic frequencies. In the largely fractured carbonate reservoirs in the Naith field in Oman, anisotropic and fluid effects such as larger S-wave splitting and lower S-wave velocities in areas which contained gas compared with areas which contained oil are observed (Sayers, 2002).

4 Modelling carbonate rocks

From the observed seismic features of carbonate rocks, where complex pore structure and effects such as wave-induced fluid flow can be significant, many assumptions of the rock physics models commonly used today are violated. The equation of Gassmann (1951), which assumes the rock to be macroscopically homogeneous, isotropic and that the pores are well connected regarding to the pore structure, or heuristic relations such as the time average equation (Wyllie et al., 1956), often mispredict the velocities for carbonates (Adam et al., 2006; Anselmetti and Eberli, 1999; Assefa et al., 2003; Baechle et al., 2005; Rossebø et al., 2005; Wang, 1997,2000). The effective medium theory of Kuster and Toksöz (1974) has succeeded to reproduce laboratory measurements (Toksöz et al. 1976; Wang, 1997), but this model is restricted to isolated pores and must be regarded as a high-frequency model when the pores are connected.

Since attenuation caused by wave-induced fluid flow is important for explaining the velocity dispersions observed for carbonate rocks, it is natural to consider frequency dependent models when modelling such rocks. This effect can even occur at seismic frequencies for low permeable carbonates and for high-permeable carbonates saturated with fluids of high viscosity (Batzle et al., 2006). Biot's model (1956a,b) for frequency dependent velocities treats mechanisms for viscose interactions between pore fluid and the mineral of the rock, however it does not include the squirt flow effect. Chapman et al. (2002) have developed a first order microstructural poroelastic model which considers compliant cracks together with spherical pores. However, since the pore structures and the pore types seem to be dominant factors for carbonate rocks (Eberli et al., 2003), this model may only be appropriate for only a few cases of pore types. The visco-elastic effective medium theory of Jakobsen et al. (2003a,b), allows higher crack densities than the model of Chapman et al. (2002) and a wide range of shapes of pores and cracks. In addition, the T-matrix

approach includes mechanical interaction between two inclusions and effects such as local and global flow. All this appears to be important for explaining many of the observed seismic properties of carbonate rocks. The pore types in an inclusion based model can be considered as grain-boundary cracks (intercrystaline and interparticle porosity), porous inclusions (intraparticle porosity) and rounded pores (vugs and fenestral porosity).

The effective stiffness tensor of the T-matrix approach is derived in Appendix A and the derivation of the t-matrix for a communicating cavity in Appendix C. In the following, the parameters in the T-matrix approach which had the highest focus in this study, the relaxation time constant (τ), pore geometry and the concept of dual porosity, are discussed.

4.1 The relaxation time constant τ

The relaxation time constant in the T-matrix approach is assumed to be determined empirically for each rock and fluid under consideration (Jakobsen et al., 2003b). If we only consider cracks with same aspect ratios, the characteristic frequency of the squirt flow mechanism associated with the peak of the attenuation is determined as

$$f_c = \frac{1}{\gamma^{(n)}\tau}, \tag{1}$$

where

$$\gamma^{(n)} = 1 + \kappa_f (K_d^{(n)} - S^{(0)})_{uuvv}. \tag{2}$$

κ_f is the bulk modulus of the fluid, $K_d^{(n)}$ is the dry response of the cracks, $S^{(0)}$ is the compliance tensor of the reference matrix and u and v represent a summation ($u, v =$ 1,2,3). When there are pores and cracks with various aspect ratios in the porosity, the characteristic frequency will be approximately equal to equation (1) for each pores or cracks of equal family n.

As for all squirt flow models proposed over the years, the characteristic frequency

depends on details of the grains and pore microgeometry (Mavko et al., 1998) as well as the properties of the fluid. O'Connell and Budiansky (1977) found the characteristic frequency to be

$$f_c = \frac{\kappa\alpha^3}{\eta}, \tag{3}$$

where κ is the bulk modulus of the frame matrix, α is the aspect ratio of the cracks and η is the viscosity of the fluid. Hudson et al. (1996) found an expression for the relaxation time to be

$$\tau = \frac{\phi_m \eta l^2}{\kappa_f K_m}, \tag{4}$$

where ϕ_m is the porosity and K_m is the permeability of the uncracked rock and l is the inter-crack spacing. Chapman et al. (2002) derived the expression for the relaxation time as

$$\tau = \frac{\eta c_v (1 + \frac{\sigma_c}{\kappa_f})}{6k\zeta\sigma_c}, \tag{5}$$

where c_v is the volume of one crack, σ_c is defined as $\frac{\pi\mu\alpha}{2(1-\nu)}$, μ is the shear modulus of the frame rock, ν is the Poisson's ratio, k is the permeability and ζ is the grain size.

The reason for the different expressions of the relaxation time derived for squirt flow are partly due to that the different models consider different pore spaces. Jakobsen and Hudson (2003) have shown that the T-matrix approach can reproduce the Hudson model (Hudson, 1996) and if we compare the τ-parameter of the T-matrix approach to the one found by Chapman et al. (2002), the analysis of Agersborg et al. (2007) suggest that

$$\gamma^{(n)} \tau_{T-matrix} = \tau_{chapman} = \frac{\eta c_v (1 + \frac{\sigma_c}{\kappa_f})}{6k\zeta\sigma_c}. \tag{6}$$

From this relation, we find that the τ-parameter in the T-matrix approach can be expressed as

$$\tau = \frac{\eta c_v (1 + \frac{\sigma_c}{\kappa_f})}{6k\zeta\sigma_c} \frac{1}{\gamma^{(n)}} = \frac{\eta c_v (1 + \frac{\sigma_c}{\kappa_f})}{6k\zeta\sigma_c} \frac{1}{1 + \kappa_f (K_d^{(n)} - S^{(0)})_{uuvv}}, \tag{7}$$

when only considering cracks in the porosity. This expression for the τ parameter suggest that it will be dependent on pore geometry, size of the pores, the bulk modulus of the reference matrix, permeability, viscosity and bulk modulus of the fluid. Since some of these quantities are difficult to measure, the relaxation time constant in the T-matrix approach should be determined empirical when frequency or, as done in paper 2, pressure dependent velocity and attenuation data are available. If there is no pressure dependent attenuation data, we have chosen the τ-paramter to be proportional to the viscosity and since the bulk modulus of the fluid is considered by the γ-parameter, it can be written as

$$\tau = C_m \eta, \tag{8}$$

where C_m is a constant of all the parameters independent of the fluid. From this relation it is possible to estimate all the other relaxation time constants for different fluids as done in paper 1 when the relaxation time for one fluid is known.

4.2 Finding the pore geometry

In real rocks, the pores and cracks will have a range of aspect ratios. Indeed, Scanning Electron Microscope (SEM) image analysis studies of carbonate rocks such as Anselmetti et al. (1998) and Rossebø et al. (2005) shows this. When modelling rocks with inclusion based models, it is impractical to have more than just a few inclusions with different aspect ratios and concentrations to varying when tuning the model to predict measurements. If there is no pressure dependent measurements, a few inclusions characterizing the porosity may be enough to get satisfying results. However, if there are pressure dependent measurements, the pores and cracks with low aspect ratios will close as the pressure increases with resulting increase in the velocity. If there are only a few inclusions describing the porosity, there will be a stepwise increase in the velocity as the pressure raising or the model can not explain

the high pressure measurements as the low aspect ratio cracks are closed. Therefore a distribution of compliant pores and cracks are better to use for obtaining a more realistic model of the porosity. How steep the increase in velocity is with increasing pressure depends on how many inclusions (cracks) with low aspect ratio there are in the sample. In this study we have chosen a generalized beta distribution similar to the one used by Tod (2001) to characterize the distribution of cracks. With only four parameters, it is possible to obtain almost any shape of the distribution (see Figure 2). The crack density distribution

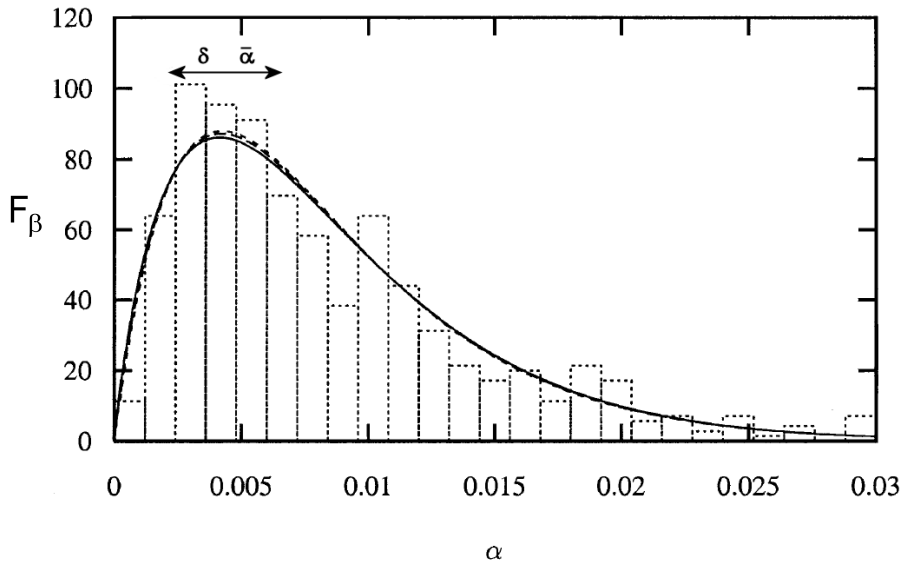

Figure 2: The generalized Beta distribution function, with $\bar{\alpha} = 0.00837$, δ=0.703 and u=0.2 (solid line), u=0.5 (long dashes), and the Gamma distribution governed by the same values of $\bar{\alpha}$ and δ (medium dashes) to approximate the sum of the crack aspect ratio observations of Hay et al. (1988) (bars) (from Tod, 2001).

can be written as (Tod, 2001):

$$\epsilon = \epsilon_0 F_\beta(\alpha), \tag{9}$$

where ϵ_0 is the total crack density and $F_\beta(\alpha)$ is the generalized beta probability density function, which can be written as

$$F_\beta(\alpha) = \frac{1}{u}\frac{\Gamma(p+q)}{\Gamma(p)\Gamma(q)}(1-\frac{\alpha}{u})^{q-1}(\frac{\alpha}{u})^{p-1}, \tag{10}$$

with

$$p = \frac{u-\bar{\alpha}-\bar{\alpha}\delta^2}{u\delta^2}, \tag{11}$$

and

$$q = \frac{u-\bar{\alpha}}{\bar{\alpha}}p. \tag{12}$$

Here u and δ are parameters for tuning the beta density probability function, $\bar{\alpha}$ denote the average aspect ratio of the cracks and Γ is the gamma function. The shape of the distribution are mainly determined from the average aspect ratio and the δ-parameter. This distribution can also be used with SEM imaging analysis to characterize the pore structure of the rock. In Figure 3, SEM imaging analysis done by Rossebø et al. (2005) are shown where they have used a form factor defined as $4\pi(area/perimeter^2)$ for evaluating the shape of the pores and cracks.

In this Ph.D. study there was no SEM image available for the core samples, but the crack distribution was used in paper 2 and 3, where good fit was achieved for the velocity versus pressure measurements of carbonates.

4.3 Dual porosity

The concept of a dual porosity system is incorporated into the T-matrix approach to model different acoustic signatures observed for carbonates. Such acoustic observations are: large scattering of velocities of equal porosity and lithology; attenuation for the dried core plugs due to residual fluids in the pore space; and anisotropy due to large fractures

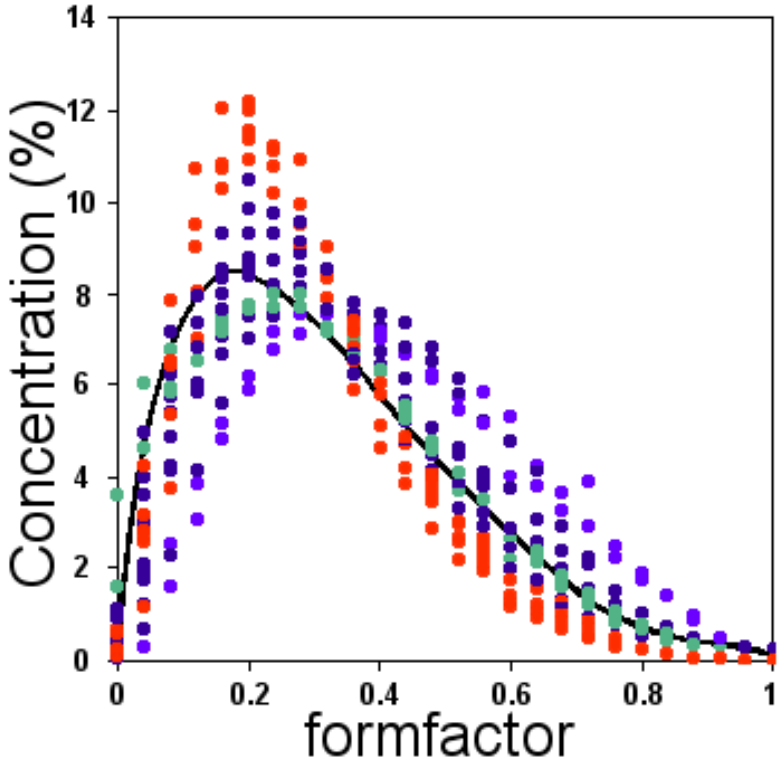

Figure 3: Pore form spectra found for different core samples by using Scanning Electron Microscope image analysis (from Rossebø et al., 2005). The colour represent the dominant porosity where red is intergranual (interparticle) porosity, green is intercrystallinge porosity and blue is moldic porosity. The solid black line represent the pore form obtained from a thin slice image.

or to the microscopic structure. The different porosity systems can either be on the same scale or on different scales and are modelled as either two separated systems or as two connected systems where scale is considered in terms of number of connections that each pore has.

The large velocity scattering of carbonates with same porosity and lithology is explained in paper 1 by dividing the pore space into two separate systems of different scales. Then, considering the pore types and whether these pores are connected on each scale, the model was able to show how this velocity dispersion can be reproduced.

In velocity and attenuation measurements for calcite core plugs in paper 2, attenuation was observed for the dried core plugs caused by residual fluid in the pore space. This fluid and the squirt flow effect can be modelled either as partially saturated pores or by two separate pore systems where one is fully saturated and the other is dry. The model of partially saturated cracks (saturated with two fluids) can be done in a similar way as Walsh (1965), Mavko and Nur (1979), and Hudson (1988), as discussed by Pointer et al. (2000) and Jakobsen and Hudson (2003). Here the wave-induced fluid flow takes place in a single crack. However, this model is developed for isolated cracks and in order to have a consistent model for both the dry and saturated core plug measurements, the model of two separated pore systems on the same scale was chosen.

Finally, the last dual porosity model used in paper three was adopted from Chapman (2003) in order to investigate the effect of fractures in a reservoir as the pore pressure was changing. In this model, the idea was that the larger fractures, due to their size, were connected to more nearby microscopic pores and cracks than the microscopic pores and cracks were to each other. The effect of scale was modelled by assuming that the relaxation time constant was dependent on the scale and each relaxation time constant of the scale was related by the size of the fractures and the grains.

Paper 1

Velocity variations in carbonate rocks due to dual porosity and wave-induced fluid flow

Remy Agersborg[1,2*], Tor Arne Johansen[1] and Morten Jakobsen[1,2]

[1]*Department of Earth Science and* [2]*Centre for Integrated Petroleum Research, University of Bergen, allégt. 41, 5007 Bergen, Norway.*

ABSTRACT

The many acoustic observations of carbonate rocks, such as large scattering of velocities with equal porosity and mineralogy, or shear modulus alteration under fluid substitution, can not be explained using traditional rock physics theories such as the Gassmann equation. The complex pore structure often seen in carbonate rocks is possibly the main reason for these variations. Attenuation caused by wave-induced fluid flow is often the source of the misprediction of porosity and pore fluid effects on the velocities with use of traditional rock physics models. For carbonates this effect can occur for all frequencies and when modelling these characteristics we assume that the porosity occur at two scales, one microscopic and one mesoscopic, combined with a visco-elastic effective medium theory. The characteristic pore types of the carbonate rocks are modelled as grain-boundary cracks (intercrystaline and interparticle porosity), porous inclusions (intraparticle porosity) and rounded pores (vugs and fenestral porosity). By studying various conditions of the connectivity of pores and cracks within the various pore systems and how the total porosity is distributed with respect to scale, we are able to model the often seen large variations of the P and S wave velocities and attenuations for equal total porosity. The shear modulus alteration is studied in virtue of wave-induced fluid flow and for a range of different fluids saturating various scale dependent porosities.

For porosities made up of pores of different scale, fluid substitution may lead to heterogeneous pore fluid distributions. We here also show how such effects can be estimated considering various pore systems and fluid saturations.

Keywords: Dual porosity, pore structure, carbonates, two-scaled modelling, wave-induced fluid flow, T-matrix approach, fluid substitution.

[*]E-mail: remy.agersborg@geo.uib.no

INTRODUCTION

Seismic velocities depend on the elastic moduli and the density of the rock, and they are mainly affected by the fluid content in the rock, mineralogy, porosity and pore types i.e. shapes and sizes. Especially, the concentration of compliant cavities such as cracks and flat pores, and the stiffer rounded pores will have a major impact on the acoustic velocities. However, other factors such as whether the cavities are isolated or connected with respect to fluid flow also need to be considered. If there is a large portion of isolated cavities, the velocity will be larger than if they are connected. When the pore space is saturated with a viscous fluid, velocity dispersion occurs and we have to be careful when comparing ultrasonic with seismic measurements for understanding fluid substitution effects.

Unlike siliciclastics, where compositional variations are the main factor for the difference in the seismic velocities, various carbonate rocks often have very similar composition (Eberli *et al*. 2003). The principal constituents of carbonate rocks are calcite ($CaCO_3$), aragonite ($CaCO_3$) and dolomite ($CaMg(CO_3)_2$). These minerals are easily soluble in acid water and can be deposited nearby, which in turn can give a complex microscopic texture. In overall, the seismic velocities of carbonate rocks will depend on all the factors mentioned above, but the pore structure and the texture appear to be the most dominant ones.

The porosity in carbonate rocks have been described by different approaches (Archie 1952; Dunham 1962; Choquette and Pray 1970; Lucia 1995). Archie (1952) and Dunham (1962) focused on carbonate textures, while Choquette and Pray (1970) and Lucia (1995) emphasized on pore types. Both Choquette and Pray (1970) and Lucia (1995) classification systems have divided the porosity of carbonates into three main pore sizes: i) The microscopic (micro) pores, with a cross section diameter less than 20 μm (Lucia 1995) and 1/16 mm (Choquette and Pray 1970), ii) the mesoscopic (meso) pores with cross section diameter 20-100 μm (Lucia 1995) and 1/16-4 mm (Choquette and Pray 1970) , and iii) the mega pores with cross section diameter larger than 100 μm (Lucia 1995) and 4 mm (Choquette and Pray 1970). In the following we adopt definitions of pore sizes of Lucia (1995).

The most common pore types constituting the porosity of carbonate rocks are intercrystalline, interparticle, intraparticle, moldic, vug, fenestral porosity and fractures. Crude descriptions of the various types are: Intercrystalline or interparticle porosity are both irregular in shape, and intraparticle porosity occurs within individual particles or grains originating from internal chambers or other openings in skeletal organisms. Moldic porosity is

developed through solution of constituents of the sediment formed from organic materials and making up a so-called secondary porosity, while vugs of round shape are usually often formed by solution of moulds. Intraparticle, moldic and vugs are not easily deformed. Fenestral porosity is round, lenticular or more irregular in shape and is primary porosity formed in algal mats by evolution of gas. Fractures are formed from collapse of pore space opened by solutions, sudden pressure changes, or various kinds of tectonic deformations. A more thorough summary of each pore type can be found in Wang (1997) or Choquette and Pray (1970).

In addition to pore type, it is important to know if the pores are isolated or connected with respect to pore pressure relaxation for prediction of seismic velocities. For high porous carbonates there are for instance observed P-wave velocity differences of 2500 m/s at equal porosity (Eberli *et al*. 2003). Figure 1 shows P and S wave velocities versus porosity for data compiled from Anselmetti and Eberli (1993) and for 12 calcite samples taken at 2 km depth of a well. The calcite samples were studied for various effective pressures (P_e) but with constant pore fluid pressure (P_f) equal to 5 MPa. The figure shows large variations in velocities and our dataset reveals differences up to 1000 m/s even for the low porous samples. These differences in P velocities are mainly caused by the alteration of the pore shapes (e.g. closing/opening of cracks) as P_e is changing. In the study of Anselmetti, Luthi and Eberli (1998), two extreme fluid pathways were found in the carbonate samples. First, fluid flow can occur through connected meso pores and, second, the fluid can flow through the micro pores. In their studies of carbonates with homogeneous texture, one of these two fluid pathways was the dominant one, but in a real reservoir they expected a mixing of such sort (pore types) and both fluid flow processes can occur.

The aim of this study is to show how large velocity variations for similar lithology, porosity and pore fluid of carbonate rocks can be modelled by using visco-elastic effective medium theory. We consider the so-called T-matrix approach of Jakobsen *et al*. (2003a,b) applied to the pore types of two classes; cracks (representing the compliant part of the porosity) and pores (representing the stiff part of the porosity). We also take into account scale and the various connection models of the various pore types. Furthermore, a dual porosity system is used to include porosity of micro and meso scales, and to reveal how the different connection models of pores, pore shapes and fluid content may imply observed seismic properties of carbonates.

ROCK PHYSICS OF CARBONATES

In general we have to let go of the details of the geometrical descriptions of the porosity (with many pore classes) when we discuss carbonate rocks with mathematical models dealing with idealized shapes. The equation of Gassmann (1951) does not have any explicit assumptions of the pore structure (with respect to pore shape) other than that it must be connected to ensure the fluid in the rock to be in a relaxed state. Heuristic relations such as the time average equation (Wyllie, Gregory and Gardner 1956), often fail to predict the velocities for carbonate rocks when the porosity is made up of compliant pores and cracks (Adam, Batzle and Brevik 2006; Anselmetti and Eberli 1999; Assefa, McCann and Sothcott 2003; Baechle *et al*. 2005; Rossebø *et al*. 2005; Wang 1997,2000). The effective medium theory of Kuster and Toksöz (1974) does manage to reproduce laboratory measurements (Toksöz, Cheng and Timur 1976; Wang 1997), but it is restricted to consider isolated pores, and it must be regarded as a high frequency model since no fluid flow occurs. Thus, inclusion based theories using pore shapes are appealing to use for carbonates since a dominant factor for the acoustic properties appears to be the pore structure (Eberli *et al*. 2003). The pore types can be considered as grain-boundary cracks (intercrystaline and interparticle porosity), porous inclusions (intraparticle porosity) and rounded pores (vugs and fenestral porosity).

The model of Kuster and Toksöz (1974) can be used for predicting the effective bulk modulus in the high frequency range and then when combined with Gassmann (1951) through the dry properties, it can be used for modelling the low frequency behaviour. However, neither of these models includes squirt flow effects, which often are present in both laboratory and seismic experiments (Batzle, Han and Hofmann 2006). Therefore inclusion based models which consider fluid flow (e.g. Chapman, Zatsepin and Crampin 2002 or Jakobsen *et al*. 2003a,b) need to be considered when modelling rocks with potentially large fractions of crack-like pores. In the following, we shall use the approach of Jakobsen *et al*. (2003a,b) to describe velocity scattering caused by the pore structure. A brief review of the theory is outlined before the modelling results are presented.

THE T-MATRIX APPROACH TO CARBONATE ROCK PHYSICS

The effective stiffness tensor of the medium

The visco-elastic effective medium theory of Jakobsen *et al*. (2003a,b) considers a model of a homogeneous matrix material embedded with inclusions of same scale which are

divided into families having the same concentrations and shape/orientations, labelled by r = 1,2,…,N. This can again be divided into cavities (r = 1,2,…,N_c) and inclusions of solids or porous materials (r = N_c+1,…,N). The effective stiffness $\mathbf{C}^*$ is given by (Jakobsen *et al.* 2003a,b)

$$\mathbf{C}^* = \mathbf{C}^{(0)} + \mathbf{C}_1(\mathbf{I}_4 + \mathbf{C}_1^{-1}\mathbf{C}_2)^{-1}, \tag{1}$$

$$\mathbf{C}_1 = \sum_{r=1}^{N} v^{(r)}\mathbf{t}^{(r)}, \tag{2}$$

$$\mathbf{C}_2 = \sum_{r=1}^{N}\sum_{s=1}^{N} v^{(r)}\mathbf{t}^{(r)}\mathbf{G}_d^{(rs)}\mathbf{t}^{(s)}v^{(s)}, \tag{3}$$

where $\mathbf{C}^{(0)}$ is the fourth-rank stiffness tensor of the homogeneous matrix material, $\mathbf{I}_4$ is the identity for fourth-rank tensors, $v^{(r)}$ is the volume concentration for inclusion of type r, $\mathbf{t}^{(r)}$ is the T-matrix, $\mathbf{G}_d^{(rs)}$ is given by the strain Green's functions integrated over a characteristic ellipsoid having the same symmetries as $p^{(slr)}(\mathbf{x}\text{-}\mathbf{x}')$ which, in turn, gives the probability density for finding an inclusion of type s at point $\mathbf{x}'$ given there is an inclusion of type r at point $\mathbf{x}$. The T-matrix of a single inclusion of type r is given by (Jakobsen *et al.* 2003a,b)

$$\mathbf{t}^{(r)} = (\mathbf{C}^{(r)} - \mathbf{C}^{(0)})[\mathbf{I}_4 - \mathbf{G}^{(r)}(\mathbf{C}^{(r)} - \mathbf{C}^{(0)})]^{-1}, \tag{4}$$

where $\mathbf{C}^{(r)}$ is the stiffness tensor for the inclusion and $\mathbf{G}^{(r)}$ is a fourth rank tensor depending only on the aspect ratio of the inclusion and $\mathbf{C}^{(0)}$. If the inclusion represent a visco-elastic porous material, equation (4) will be dependent on the frequency.

From the effective stiffness tensor of the isotropic reservoir found from Equation (1) the P- and S-wave velocity and corresponding attenuations can be expressed as (Jakobsen *et al.* 2003b)

$$V_P = \left[\mathrm{Re}\left(\frac{C_{11}^*}{\rho^*}\right)\right]^{-1}, \tag{5}$$

$$V_S = \left[\mathrm{Re}\left(\frac{C_{44}^*}{2\rho^*}\right)\right]^{-1}, \tag{6}$$

$$Q_P = \frac{\mathrm{Re}\left(C_{11}^*\right)}{\mathrm{Im}\left(C_{11}^*\right)}, \text{ and} \tag{7}$$

$$Q_S = \frac{\mathrm{Re}\left(C_{44}^*\right)}{\mathrm{Im}\left(C_{44}^*\right)}. \tag{8}$$

Here ρ^* is the effective density and V_S is divided by 2 because of the stiffness tensor is in Kelvin notation.

The t-matrix for communicating cavities

A detailed derivation of the t-matrix equations where the effects of communicating cavities are incorporated can be found in Jakobsen *et al.* (2003b). In this paper we only list the important equations which concern the allowance of one fully saturated cavity to exchange fluid mass with other cavities. The t-matrix for a fully saturated cavity can be expressed by a dry t-matrix and a term which considers the fluid effects (Jakobsen *et al.* 2003a,b; Jakobsen and Hudson 2003)

$$\mathbf{t}^{(r)} = \mathbf{t}_d^{(r)} + \frac{\Theta \mathbf{Z}^{(r)} + i\omega\tau\kappa_f \mathbf{X}^{(r)}}{1 + i\omega\gamma^{(r)}\tau}, \tag{9}$$

$$\mathbf{X}^{(r)} = \mathbf{t}_d^{(r)} \mathbf{S}^{(0)} (\mathbf{I}_2 \otimes \mathbf{I}_2) \mathbf{S}^{(0)} \mathbf{t}_d^{(r)}, \tag{10}$$

$$\mathbf{Z}^{(r)} = \mathbf{t}_d^{(r)} \mathbf{S}^{(0)} (\mathbf{I}_2 \otimes \mathbf{I}_2) \mathbf{S}^{(0)} \left(\sum_{r=1}^{N_c} \frac{v^{(r)} \mathbf{t}_d^{(r)}}{1 + i\omega\gamma^{(r)}\tau} \right), \tag{11}$$

$$\Theta = \kappa_f \left\{ \left(1 - \kappa_f \mathbf{S}^{(0)}_{uuvv}\right) \left(\sum_{r=1}^{N_c} \frac{v^{(r)}}{1 + i\omega\gamma^{(r)}\tau} \right) + \kappa_f \left(\sum_{r=1}^{N_c} \frac{v^{(r)} (\mathbf{K}_d^{(r)})_{uuvv}}{1 + i\omega\gamma^{(r)}\tau} \right) - \frac{i k_u k_v \Gamma_{uv} \kappa_f}{\eta_f \omega} \right\}^{-1}, \tag{12}$$

$$\gamma^{(r)} = 1 + \kappa_f \left(\mathbf{K}_d^{(r)} - \mathbf{S}^{(0)} \right)_{uuvv}, \tag{13}$$

$$\mathbf{K}_d^{(r)} = \left(\mathbf{I}_4 + \mathbf{G}^{(r)} \mathbf{C}^{(0)} \right)^{-1} \mathbf{S}^{(0)}. \tag{14}$$

Here $\mathbf{t}_d^{(r)}$ is the t-matrix for the dry cavity of family r, $\mathbf{S}^{(0)} = \left(\mathbf{C}^{(0)}\right)^{-1}$, ω is the frequency, τ is the relaxation time constant, κ_f and η_f are the bulk modulus and viscosity of the fluid, k_u and k_v are components of the wave number vector, Γ_{uv} is the permeability tensor of the rock and the subscription u and v represent summation over u and v, respectively (u,v = 1,2,3). I_2 is a second rank tensor and $\otimes$ denotes a dyadic tensor product.

The relaxation time constant (τ) is assumed to be an empirical constant in Jakobsen *et al.* (2003b) and is suggested to be dependent on the scale of the pores and cracks, on the properties of the fluid and the mineral the cavities are embedded in. The constant must under these assumptions be determined for each fluid under consideration where attenuation due to wave induced fluid flow are significant. In order to discuss fluid effects in this study we will in the following assume that the τ-parameter can be expressed as

$$\tau = C_m \eta, \tag{15}$$

where C_m is an empirical constant independent on the fluid under consideration. With this expression the characteristic frequency ($f_c = \frac{1}{\gamma^{(r)}\tau}$) of the squirt flow mechanism will be inverse proportional to the viscosity and proportional to the fluid bulk modulus. From equation (15) we can estimate the τ-parameter from the empirical determined τ-parameter from one fluid when substituting the fluid with another as

$$\tau^{\text{fluid2}} = \tau^{\text{fluid1}} \frac{\eta^{\text{fluid2}}}{\eta^{\text{fluid1}}}. \tag{16}$$

DUAL POROSITY MODELS

Pores within the oil column of reservoirs are either within the mineral particle size or significantly larger and connected through the interparticle porosity. They are oil saturated because of their relative large size and that the oil migrations into these pores are controlled by the interparticle pore size (Lucia 1995). The intraparticle micro porosity may, due to the small pore size implying high capillary forces, trap the water and lead to anomalously high water saturation within a productive interval (Lucia 1995). For the modelling of a porosity which also may contain two fluids with different wettability, we have chosen to divide the porosity into two separate pore spaces. The porosity system can be made up of pores on the same scale (see e.g. Agersborg *et al*. (2007b)) or on different scales. Here we focus on the effects of micro and meso porosity within the same rock.

The dual porosity is modelled by first finding the effective properties of the micro porous constituent made up of aragonite, calcite or dolomite and with a specific porosity φ_{micro}. Similarly the elastic properties of the constituent, again made up of calcite, aragonite or dolomite, with meso porosity φ_{meso} is modelled. Finally, an effective composite is modelled with the constituents holding the meso porosity as a host medium embedding a volume fraction φ_{inc} of spherical inclusions made up of the constituent with porosity φ_{micro}. The effective micro porosity will be $\varphi^*_{\text{micro}} = v_{\text{inc}}\varphi_{\text{micro}}$. With the meso porosity φ_{meso}, the total porosity is then $\varphi_{\text{tot}} = \varphi_{\text{meso}} + \varphi^*_{\text{micro}}$.

The effect of scale is modelled by embedding the pores and cracks as visco-elastic inclusions with micro porosity one scale smaller, or more, than for the meso porosity. Figure 2 shows conceptual models were the micro and meso porosities are always isolated with

respect to each other. However, the pore systems can have different pore fluids and individually have connected or unconnected pores. For our modelling, we shall consider φ_{micro}, φ^{*}_{micro} and φ_{meso} to be held constant (if not otherwise stated). The different pore types are represented as spheroidal inclusions where cracks are defined with aspect ratio (α: ratio of the length of minor to major axis of an ellipsoid) less than 0.001. The relevant properties of the minerals and fluids used are listed in Tables 1 and 2, while the τ-parameter is chosen to be 10^{-7}s for water saturated rocks and according to equation (16) for oil and gas saturations. In the following we consider four porosity models (see Figure 2), where **model 1**) has no cracks in both porosity systems, **model 2**) has cracks in φ^{*}_{micro} and no cracks in φ_{meso}, **model 3**) has no cracks in φ^{*}_{micro} and cracks in φ_{meso} and **model 4**) with cracks in both porosity systems. The aspect ratios and concentrations of the cracks and pores are listed in Table 3.

Model 1 – No cracks

In model 1, aragonite is chosen as host mineral for the micro porosity while calcite is host for the meso porosity. The concentration and aspect ratios of the micro and meso pores are listed in Table 3. In Figure 3, low-frequency P and S wave velocities (V_P and V_S) for a water saturated rock are plotted as the various porosities are decreasing from the maximum total porosity ($\varphi_{tot} = 17\%$). At $\varphi_{tot} = 11\%$ and water as pore fluid , the difference between the extreme values for V_P is about 300 m/s and 100 m/s for V_S when the pores are individually connected. Modelling shows that the differences will be even larger if the porosity contains cracks and/or that the contrasts in the minerals properties are greater. Figure 4 shows V_P and V_S and the corresponding attenuations Q_P^{-1} and Q_S^{-1} as function of frequency with various pore models (connectivity). The velocity differences between individually connected and isolated pore systems are large (650 m/s for the V_P and 190 m/s for the V_S). V_P obtained from the generalized Gassmann model (Berryman and Milton 1991) and the formulations of Kuster and Toksöz (1974) are also shown in Figure 4a. Here the applied dry bulk modulus was modelled considering the pores fully connected on both scales. In the generalized Gassmann equation the two porous constituents mixed are of the same scale and the fluid can flow within and between both constituents (Berryman and Milton 1991). This is in contrast with the present model, where the porous within the porous inclusions are one scale-size smaller than the pores in the porous matrix. However, in absence of a better model to use we find the generalized Gassmann appropriate for our comparison. From Figure 4a, we see that the

frequency of the attenuation peak for connected micro pores and isolated meso pores are lower than when both the pore systems are individually connected. However, the opposite can be observed for the S-wave attenuation peak (Figure 4b).

To study the combined effects of mineralogy and pore fluid, we limit ourselves to fully individual connected micro and meso porosity. Figure 5 shows V_P, V_S, Q_P^{-1} and Q_S^{-1} using calcite, dolomite and aragonite mixed in 9 different ways and with water as pore fluid. Comparing the results where aragonite is in the micro scale and calcite in the meso scale, to where dolomite is in the micro scale and aragonite is in the meso scale, we see that their low-frequency responses are equivalent, while their high-frequency responses differ. Also, there is a frequency shift of the attenuation peak compared to when only the micro pores or the meso pores are connected (Figure 4a). This occurs due to the different properties of the mineralogies used. Furthermore, the attenuation peak of the P-wave for pure calcite appears at higher frequency than for the pure aragonite, caused by the fact that aragonite is stiffer than the calcite. If the mineralogy is equivalent for both scales, we do not see this frequency effect for the various pore connection models. This is because the wavelength being much greater than the pores (the long wavelength approximation) and that pores with equal shape and τ-parameter have equal response regardless of size. The S-wave shows almost no difference in the frequency shift of the attenuation peak for pure calcite or pure aragonite.

Figure 6 shows V_P, V_S, Q_P^{-1} and Q_S^{-1} for various combinations of pore fluids saturating the micro and meso pores. Here water, oil and methane with properties listed in Table 2 are combined in 9 ways. Equation (16) is used to evaluate the relaxation time for each fluid from the value of the water saturated model ($\tau = 10^{-7}$s). To obtain the relaxation times we thus need to consider only one pore fluid within the pore system. We see three classes where the fluid in the meso porosity dominates the behaviour of the P-wave velocity for low frequencies. For ultrasonic frequencies, the picture is more complicated. In the squirt flow mechanism window, between the low- and high-frequency limits, V_P for various combinations of pore fluids in the pore systems fluctuates. In the high-frequency limit, there are no longer distinct classes for the oil and water saturated meso porosity. The V_S differences are caused by the different densities of the fluids. With methane in the meso porosity (which is almost equal to the dry rock) and water or oil in the micro porosity we see the dominant effect of the fluid saturating the micro cracks. The attenuation signature also indicates the presence of the fluid types in the compliant pores e.g. when they are gas saturated instead of oil or water saturated, the attenuation peak shift towards higher frequencies.

Model 2 – Micro cracks

Model 2 includes micro cracks as defined in Table 3. Calcite is used as host material for both micro and meso porosity, while the two pore systems may be differently saturated with water, oil or methane. The values used in the modelling are given in Tables 1 and 2. Figure 7 shows V_P, V_S, Q_P^{-1} and Q_S^{-1} for various fluid combinations and different connection models. V_P shows a similar trend as for model 1 due to fluid flow, but now there are two additional attenuation peaks appearing at lower frequencies due to the cracks defined in the micro porosity. Also when the cracks are within the micro porosity the frequency band yielding squirt flow is expanded toward lower frequencies compared to model 1. For gas saturation, the attenuation peaks due to the cracks interfere with the attenuation peak caused by the meso porosity. A similar picture can be seen for V_S. The difference in velocities of connected and isolated porosity is for V_P 1100 m/s and for V_S 200 m/s.

Model 3 – Meso cracks

In model 3 there are meso cracks as defined in Table 3. The micro porosity is as in model 1, while the mineral and fluids are as in model 2. The modelled V_P, V_S, Q_P^{-1} and Q_S^{-1} are plotted in Figure 8. Note that even though the total crack density ($\varepsilon^{(r)} = \frac{3v^{(r)}}{4\pi\alpha^{(r)}}$) in models 2 and 3 are identical, both V_P and V_S are here significantly lower. This is because in addition to the cracks in the meso porosity, the micro porous material with cracks has larger concentration of spherical pores, and thus, appears to be stiffer than in the case of no cracks (see Table 3). The differences in velocities between the connected and isolated pores in the systems are now about 1000 m/s for V_P and about 250 m/s for V_S. Also the differences for various fluids are greater compared to the previous modelling. The attenuation is increased with the inclusion of meso cracks compared to model 2. The choice of only one aspect ratio to characterize the cracks in the meso porosity is the cause of only one wage additional attenuation peak in this model.

Model 4 – Micro and meso crack

Finally, model 4 includes cracks on both scales and the same micro porosity as in model 2 and meso porosity as in model 3. Calcite is still the host mineral for both porosities. The effects of the various connection models on velocities and attenuations are seen in Figure 9. There are larger differences in the velocities between the connected and the isolated pores,

up to 1200 m/s for V_P and 300 m/s for V_S compared with previous results. Surprisingly, when having both micro and meso cracks, both V_P and V_S are larger for the case of isolated pores in both scales than for model 3. Again, this is because the micro porous material is stiffer when including micro cracks.

DISCUSSION

Effects of pore types

The modelling related to the four models reveals several possible seismic signatures of carbonate rocks. The scattering of the velocities for equal total porosity may be explained in context of pore types, scale of the pores and cracks and whether they are isolated with respect to fluid flow or not. Figure 3 shows the importance of the scale of the porosity. Even though there were two mineral constituents in model 1, the effect of the scale is significant. When the total porosity is constant, the model which consists of the larger portion of the micro porosity gives higher velocities. In this case it is because the mineral containing the micro pores are stiffer than the mineral containing the meso pores. Figure 4 shows the effects of connected and isolated pores and cracks. With same micro and meso porosity there is a difference in V_P of 500 m/s between connected to isolated pores. In Figure 9a, where cracks are in both porosity systems there is a difference of about 1200 m/s for V_P.

In addition to pores, fractures have a great effect on fluid flow pathways. Fractures can be open or closed due to mineralization and they may have different resistance to fluid flow of fluids due to capillary forces. A partially mineralized fracture can provide a better hydrocarbon recovery because the mineral can act as a natural prop, thus keeping the fracture open during depletion. If the fracture is totally mineralized, the fracture could act as a permeability barrier (Dürrast and Siegesmund 1999). Open fractures can be modelled with the use of the T-matrix approach by considering the relaxation time constant (Equation (16)) to be scale dependent (Agersborg *et al*. 2007a). When the fractures are connected to the nearby and smaller cavities, the relaxation time for the fractures can be related to relaxation time of the micro porosity of similar shapes as (Chapman 2003; Agersborg *et al*. 2007a)

$$\tau^{\text{fracture}} = \frac{s^{\text{fracture}}}{s^{\text{grain}}} \tau^{\text{micro porosity}}, \tag{17}$$

where s^{fracture} and s^{grain} are the radii of the fracture and the grains, respectively.

The models considered are isotropic. However, the modelling can include anisotropy as outlined in Agersborg *et al*. (2007b). Such pore models are of particular value when

considering effects of pressure on seismic velocities. Also, in this modelling we have considered a discrete crack/pore model whereas in Agersborg *et al* (2007a,b) a distribution of cracks was considered. Formulation of continuous distributions implies a smooth change in seismic properties as pressure is altered instead of a step wise behaviour often seen using discrete pore models. The formula for the crack distribution depend on four parameters which can be determined from measured pressure dependent velocities and attenuations as shown in Agersborg *et al*. (2007b), or by analyses of scanning electron microscope images of thin sections as in the study of Rossebø *et al*. (2005) or Anselmetti *et al*. (1998).

Effects of fluids

Physical properties of some fluids are shown in Figure 6. The τ-parameter for each fluid should ideally be defined from the attenuation and/or the velocity measurements, but with use of equation (16) τ can be evaluated. The attenuation peaks due to wave induced fluid flow is seen to decrease with frequency as the viscosity increases, as is in agreement with the observation of Batzle *et al*. (2006). With compliant cracks the squirt flow effects will occur in a broader frequency band. This is shown for various pore connection models and various pore fluids in Figure 7 (micro cracks), Figure 8 (meso cracks) and Figure 9 (both types of cracks).

Since fluids have no shear modulus it is often assumed that the saturated and dry shear moduli of the rock are equivalent. However, for many carbonate rocks either shear weakening or shear strengthening is observed (Adam *et al*. 2006; Assefa *et al*. 2003; Baechle *et al*. 2005). Adam *et al*. (2006) identified evidence of at least three mechanisms causing this. Weakening can occur due to surface-energy reduction or crack growth, while strengthening can occur due to shear modulus dispersion inferred from squirt or global flow in the pore space. They also observed weakening of the shear modulus at low frequencies and shear strengthening at high frequencies. This implies that more than one rock-fluid mechanism is active. Also, since carbonate minerals are easily soluble mineral dissolution may also cause altered pore space and thereby an altered shear modulus.

The modelling study discussed can not explicitly account for the chemical interaction or dissolution of the minerals, but many of the mechanism causing the alteration of the shear modulus can be explained. Agersborg *et al*. (2007b) showed that if residual fluid exists in undrained cracks of a dried sample, this may stiffen or weaken the frame of the rock with respect to shear forces, since this may control the opening or closing of compliant pores. Since the T-matrix approach accounts for both global and squirt flow mechanisms, it may also

apply for describing the mechanism behind shear modulus strengthening. In model 1 in Figure 4b, with an effective dry density of 2273.6 kg/m^3 and an effective water saturated density of 2450.5 kg/m^3, the saturated and dry shear modulus is 16.6 GPa and 14.3 GPa, respectively. This gives a shear strengthening of about 16% when the pores are isolated with respect to fluid flow on both pore systems. In the case where all the pores are connected, the saturated and dry shear modulus is equal.

CONCLUDING REMARKS

The use of a visco-elastic effective medium theory for modelling the stiffness tensor of complex porous materials as carbonate rocks has been discussed. In this paper we have focused on the role of the scale of porosity on seismic parameters, i.e. when the pore systems contain micro and meso pores which are connected or isolated with respect to pore fluid flow. Both P and S wave velocities, attenuations and dispersion effects are modelled for various systems of pore fluids and porosity scenarios.

The pore types characterized for carbonates can be modelled by their shapes and sizes. The modelling showed that we can obtain a spectrum of velocity and attenuation signatures with the same mineralogy and porosity, by varying the pore types, the connectivity between them and the pore fluid distribution. Shear modulus strengthening can occur due to squirt flow effects, and alteration of the pore to pore connection can occur due to chemical interaction between fluid and rock minerals.

Different scales of pores influence on the draining properties, i.e. a fluid substitution processes may cause different pore fluids in the micro and meso porosity. Our modelling also points to possible acoustic signatures of such heterogeneous pore fluid saturation scenarios. In essence, our results point to the necessity of realistic modelling to assist in quantitative seismic interpretation of fluid substitution and 4D effects. The present work may help to develop more such realistic models.

ACKNOWLEDGMENT

We would like to thank Hydro for providing the core materials and financing of both the Ph.D. scholarship to R.A. and the experimental work.

REFERENCES

Adam, L., Batzle, M. and Brevik, I. 2006. Gassmann's fluid substitution and shear modulus variability in carbonates at laboratory seismic and ultrasonic frequencies. Geophysics **71**, F173-F183.

Agersborg, R., Jakobsen, M., Ruud. B.O. and Johansen, T.A. 2007a. Effect of pore fluid pressure on the seismic response of a fractured carbonate reservoir. Studia Geophysica et Geodaetica **51**, 89-118.

Agersborg, R., Johansen T.A., Jakobsen, M., Sothcott, J. and Best, A.I. 2007b. Effects of fluids and dual pore systems on velocities and attenuations of carbonates. Submitted to Geophysics.

Anselmetti, F.S. and Eberli, G.P. 1993. Controls on sonic velocity in carbonates. Pure and Applied Geophysics **141**, 287-323.

Anselmetti, F.S. and Eberli, G.P. 1999. The velocity-deviation log: A tool to predict pore type and permeability trends in carbonate drill holes from sonic and porosity or density logs. AAPG Bulletin **83**, 450-466.

Anselmetti, F.S., Luthi, S. and Eberli, G.P. 1998. Quantitative characterization of carbonate pore systems by digital image analysis. AAPG Bulletin **82,** 1815-1836.

Archie, G.E. 1952. Classification of carbonate reservoir rocks and petrophysical considerations. AAPG Bulletin **36**, 278-298.

Assefa, S., McCann, C. and Sothcott, J. 2003. Velocities of compressional and shear waves in limestones. Geophysical Prospecting **51**, 1-13.

Baechle, G.T., Weger, R.J., Eberli, G.P., Massaferro, J.-L., and Sun, Y.-F. 2005. Changes of shear moduli in carbonate rocks: Implications for Gassmann applicability. The Leading Edge **24**, 507-510.

Batzle, M.L., Han, D.-H., and Hofmann, R. 2006. Fluid mobility and frequency-dependent seismic velocity – Direct measurement. Geophysics **71**, N1-N9.

Batzle, M. and Wang, Z. 1992. Seismic properties of pore fluids. Geophysics **57**, 1396-1408.

Berryman, J.G. and Milton, G.W. 1991. Exact results for generalized Gassmann equations in composite porous-media with two constituents. Geophysics **56**, 1950-1960.

Chapman, M., Zatsepin, S.V. and Crampin, S. 2002. Derivation of a microstructural poroelastic model. Geophysical Journal International **151**, 427-451.

Chapman, M. 2003. Frequency-dependent anisotropy due to meso-scale fractures in the presence of equant porosity. Geophysical Prospecting **51**, 369-379.

Choquette, P. and Pray, L. 1970, Geologic nomenclature and classification of porosity in sedimentary carbonates. AAPG Bulletin **54**, 207-250.

Dunham, R.J. 1962. Classification of carbonate rocks according to texture. In: Classification of carbonate rocks – a symposium: AAPG Memoir 1 (Ed. W.E. Ham) pp. 108-121. AAPG. ISBN 0891812768.

Dürrast, H. and Siegesmund, S. 1999. Correlation between rock fabrics and physical properties of carbonate reservoir rocks. International Journal of Earth Sciences **88**, 392-409.

Eberli, G.P., Baechle, G.T., Anselmetti, F.S. and Incze, M.L. 2003. Factors controlling elastic properties in carbonate sediments and rocks. The Leading Edge **22**, 654-660.

Gassmann, F. 1951. Über die Elastizität poröser Medien. Viereljahrscrift der Naturforschende Gesellschaft in Zürich **96**, 1-23.

Jakobsen, M. and Hudson J.A. 2003. Visco-elastic waves in rock-like composites. Studia Geophysica et Geodaetica **47**, 793-826.

Jakobsen, M., Hudson, J.A. and Johansen, T.A. 2003a. T-matrix approach to shale acoustic. Geophysical Journal International **154**, 533-558.

Jakobsen, M., Johansen, T.A. and McCann, C. 2003b. The acoustic signature of fluid flow in a complex porous media. Journal of Applied Geophysics **54**, 219-246.

Kuster, G.T. and Toksöz, M.N. 1974. Velocity and attenuation of seismic-waves in two-phase media: part I. Theoretical formulations. Geophysics **39**, 587-606.

Lucia, F.J. 1995. Rock-fabric/petrophysical classification of carbonate pore space for reservoir characterization. AAPG Bullitin **79**, 1275-1300.

Mavko, G., Mukerji, T. and Dvorkin, J. 1998. The rock physics handbook: tools for seismic analysis in porous media. Cambridge University Press. ISBN 0521620686.

Rossebø, Ø.H., Brevik, I. Gholam, R.A. and Adam, L. 2005. Modeling of acoustic properties in carbonate rocks: 75th Annual International Meeting, SEG, Expanded Abstracts, 1505-1508.

Toksöz, M.N., Cheng, C.H. and Timur, A. 1976. Velocities of seismic waves in porous rocks. Geophysics, **41**, 621-645.

Wang, Z. 1997. Seismic properties of carbonate rocks. In: Carbonate Seismology, Geophysical Developments Vol. 6 (eds. I. Palaz and K.J. Marfurt), pp. 29-52. SEG. ISBN 1560800380.

Wang, Z. 2000. The Gassmann equation revisited: Comparing laboratory data with Gassmann's prediction. In: Seismic and acoustic velocities in reservoir rocks, Recent developments Vol. 3 (eds. Z. Wang, and A. Nur), pp. 8-23. SEG. ISBN 1560800887.

Wyllie, M.R.J., Gregory, A.R., and Gardner, L.W. 1956. Elastic wave velocities in heterogeneous and porous media. Geophysics **21**, 41-70.

APPENDIX A

The generalized Gassmann equation for composite porous media with two constituents can be written as (Berryman and Milton 1991)

$$K^*_{sat} = K^*_{dry} + \alpha^* C, \tag{A-1}$$

$$C = \frac{\alpha^*}{\frac{\alpha^*}{K^*_s} + \langle\varphi\rangle\left(K_f^{-1} - K_\varphi^{*-1}\right)}, \tag{A-2}$$

$$\alpha^* = 1 - \frac{K^*_{dry}}{K^*_s}, \tag{A-3}$$

where the average porosity can be found from

$$\langle\varphi\rangle = f^{(1)}\varphi^{(1)} + f^{(2)}\varphi^{(2)}. \tag{A-4}$$

Here index 1 and 2 refers to the two phases and f is the concentration such that $f^{(1)} + f^{(2)} = 1$. K_f is the bulk modulus of the fluid and

$$K^*_s = \left(\frac{1}{K^*_{dry}} - \frac{\alpha^{(1)}}{K^*_{dry}} - \frac{\left(K^*_{dry} - K^{(1)}_{dry}\right)\left(\alpha^{(2)} - \alpha^{(1)}\right)}{K^*_{dry}\left(K^{(2)}_{dry} - K^{(1)}_{dry}\right)} \right)^{-1}, \tag{A-5}$$

$$\alpha^{(1)} = 1 - \frac{K^{(1)}_{dry}}{K^{(1)}_0} \tag{A-6}$$

and

$$\alpha^{(2)} = 1 - \frac{K^{(2)}_{dry}}{K^{(2)}_0}. \tag{A-7}$$

Here K_{dry} and K_0 is the dry and mineral bulk modulus of the constituents. The constant K^*_φ is

$$K^*_\varphi = \langle\varphi\rangle \left(\frac{\alpha^*}{K^*_s} - \langle\lambda\rangle - \left(\langle\alpha\rangle - \alpha^*\right)\left(\frac{\alpha^{(1)} - \alpha^{(2)}}{K^{(1)}_{dry} - K^{(2)}_{dry}} \right) \right)^{-1}, \tag{A-8}$$

where

$$\langle\lambda\rangle = f^{(1)}\left(\frac{\alpha^{(1)} - \varphi^{(1)}}{K^{(1)}_0} \right) + f^{(2)}\left(\frac{\alpha^{(2)} - \varphi^{(2)}}{K^{(2)}_0} \right). \tag{A-9}$$

The shear modulus, the effective density and the P- and S-wave velocity of the saturated medium can be expressed as

$$\mu^*_{sat} = f^{(1)}\mu^{(1)}_{dry} + f^{(2)}\mu^{(2)}_{dry}, \tag{A-10}$$

$$\rho^* = \left(1 - \langle\varphi\rangle\right)\left(f^{(1)}\rho^{(1)} + f^{(2)}\rho^{(2)}\right) + \langle\varphi\rangle\rho_f, \tag{A-11}$$

$$V_P = \sqrt{\frac{K_{sat}^* + \frac{4}{3}\mu_{sat}^*}{\rho^*}}, \tag{A-12}$$

and

$$V_S = \sqrt{\frac{\mu_{sat}^*}{\rho^*}}. \tag{A-13}$$

List of Figures

List of Tables

FIGURES

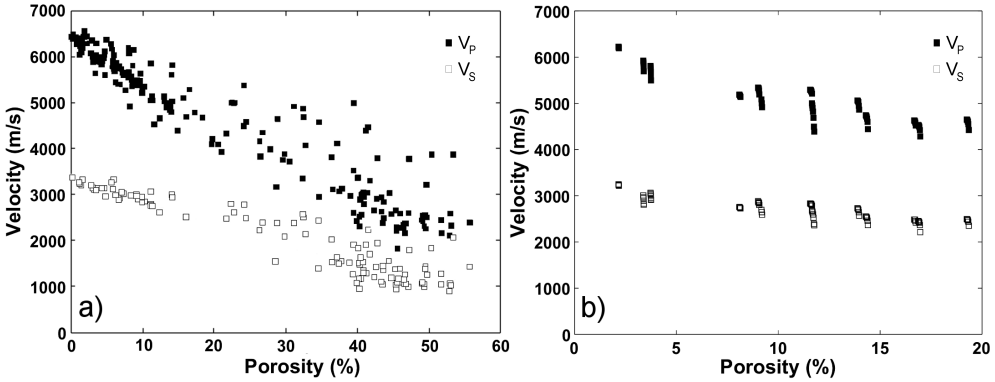

Figure 1: Observed velocity variations with porosity.
a) Water saturated aragonite, calcite and dolomite samples compiled from Anselmetti and Eberli (1993). (P_f=2 MPa and P_e=10 MPa)
b)Own data (also see Agersborg *et al*. 2007b) obtained from 12 brine saturated calcite samples at various pressures. (P_f=5 MPa and P_e= 5, 10, 20, 30, 40, 50, 60 MPa. Estimated alteration in porosity with pressure is included).

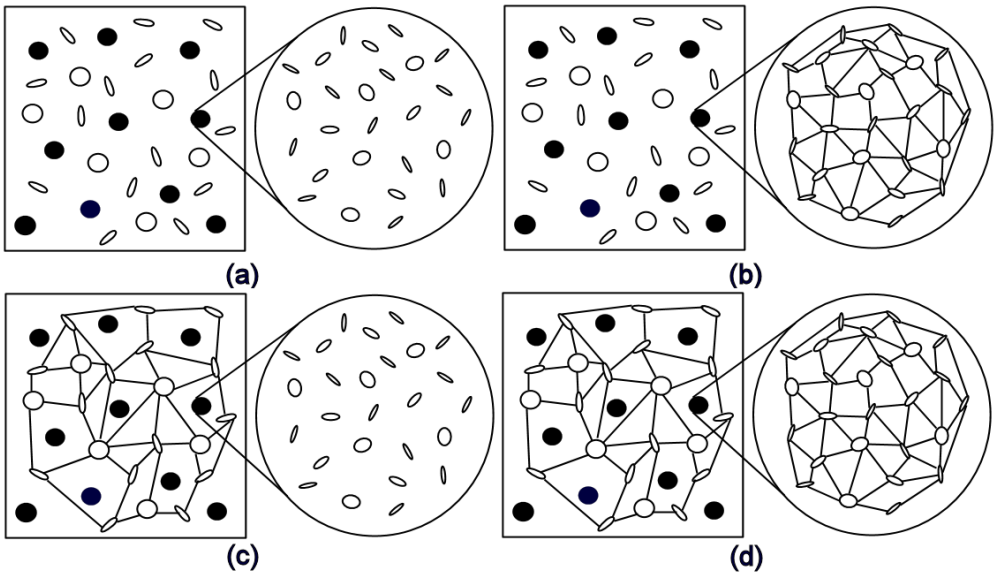

Figure 2: Conceptual sketches of the models where the pores exist both on micro and meso scale and with different connections. (a) The pores are isolated in both porosity scales; (b) The micro pores are connected and meso pores are isolated; (c) The micro pores are isolated and the meso pores are connected; (d) The pores in both the scales are connected. The porosity systems are isolated with respect to each other in all the models.

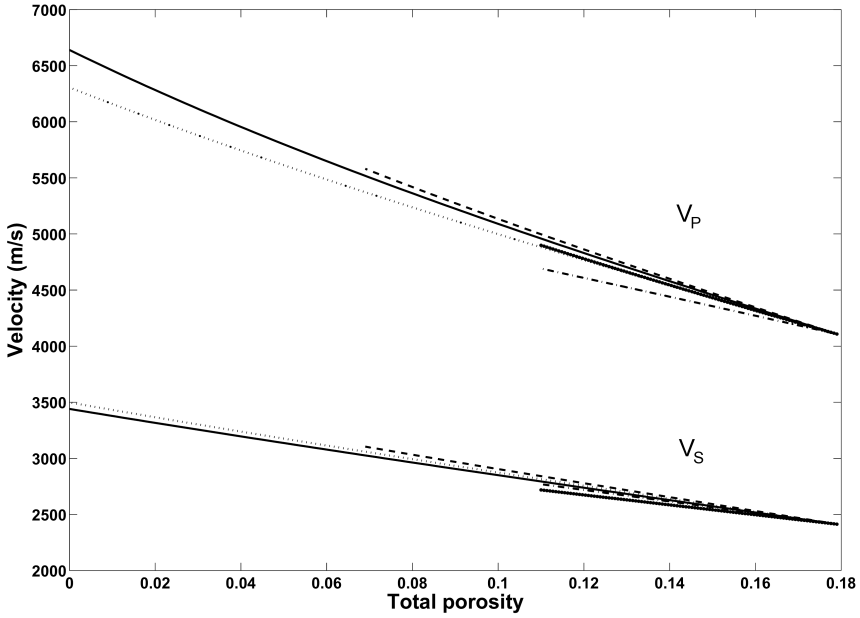

Figure 3: V_P and V_S as function of porosity. Case 1: The micro porosity varies (dashed-dotted line); Case 2: meso porosity varies (dashed line); Case 3: Both the micro and the meso porosity varies (dotted line); Case 4: The concentration of the visco-elastic inclusions varies (dense solid line); Case 5: Both the visco-elastic inclusion and the meso porosity varies (solid line).

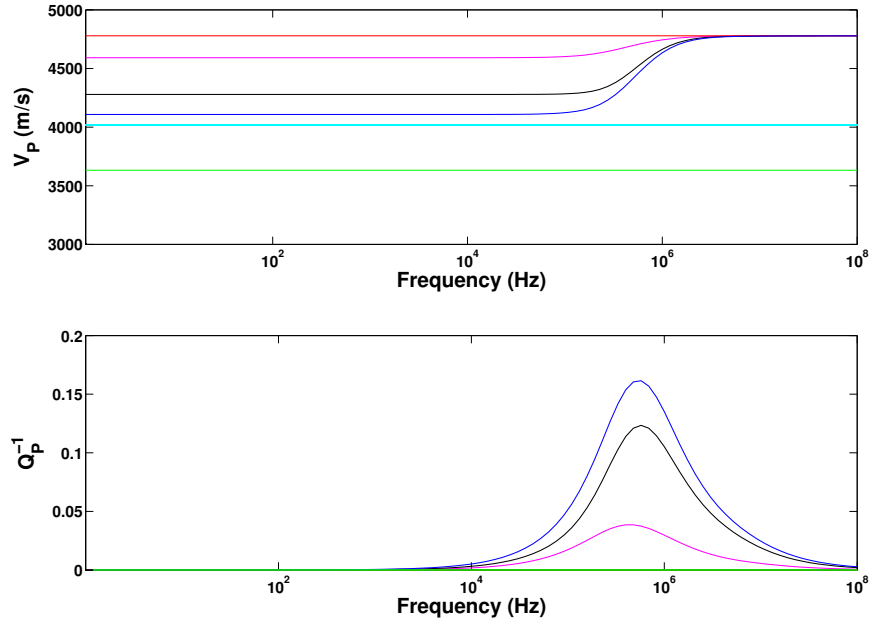

Figure 4a: V_P and Q_P^{-1} as functions of frequency. Case 1: connected pores in the micro and meso porosity, but isolated with respect to each other (blue). Case 2: connected pores in the micro porosity and isolated pores in the meso porosity (magenta). Case 3: connected pores in the meso porosity and isolated pores in the micro porosity (black). Case 4: isolated pores in both the micro and meso porosity (red). Dry (green) and generalized Gassmann calculated V_P (cyan). Case 2 is equivalent to V_p calculated by the formulations of Kuster and Tolsöz (1974).

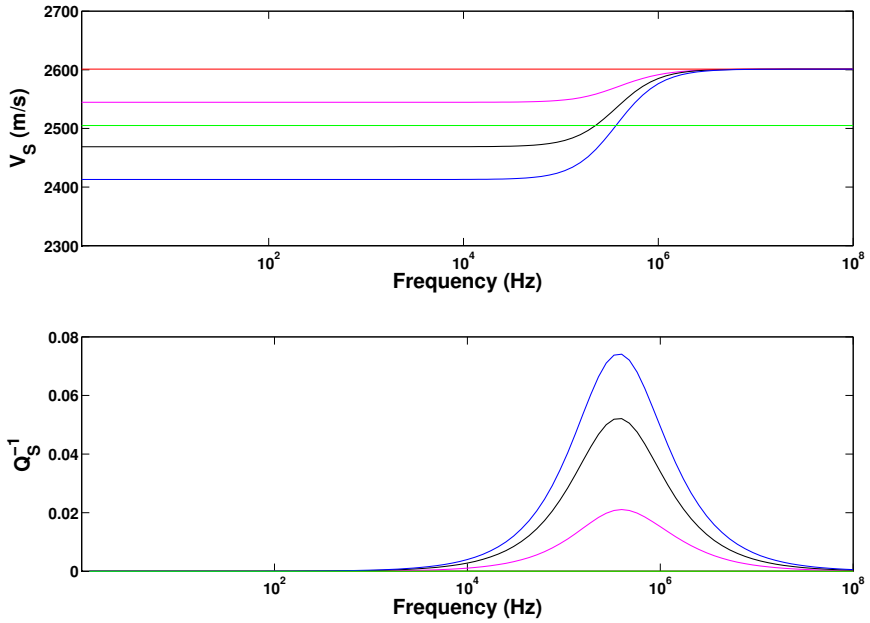

Figure 4b: V_S and Q_S^{-1} as functions of frequency. Case 1: connected pores in the micro and meso porosity, but isolated with respect to each other (blue). Case 2: connected pores in the micro porosity and isolated pores in the meso porosity (magenta). Case 3: connected pores in the meso porosity and isolated pores in the micro porosity (black). Case 4: isolated pores in both micro and meso porosity (red). Dry (green).

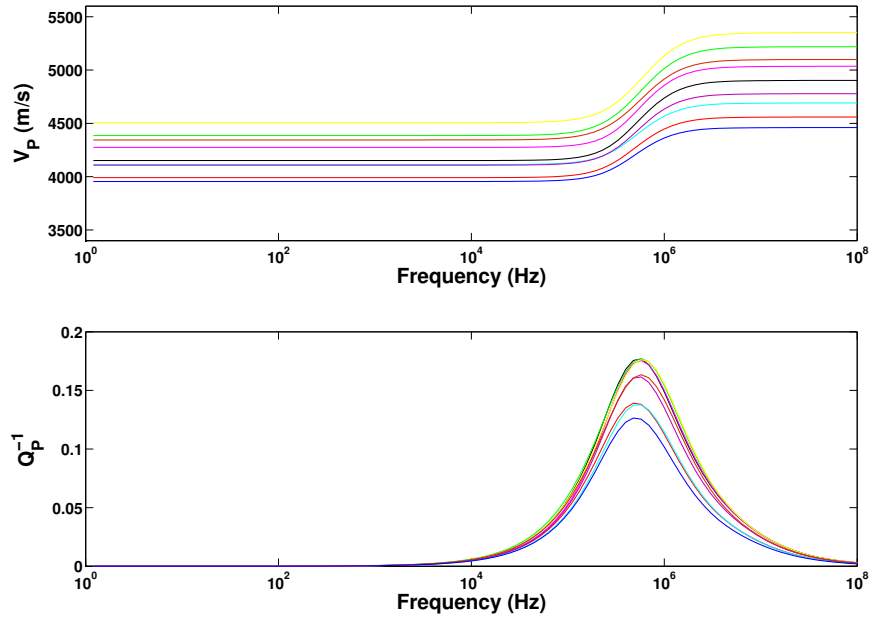

Figure 5a: V_P and Q_P^{-1} as functions of frequency and different mineralogy. Calcite (C), Dolomite (D) and Aragonite (A). The first letter corresponds to inclusion and the second to the matrix mineral. CC (black); CD (green); CA (red); DC (magenta); DD (yellow); DA (cyan); AC (brown); AD (pink) and AA (blue).

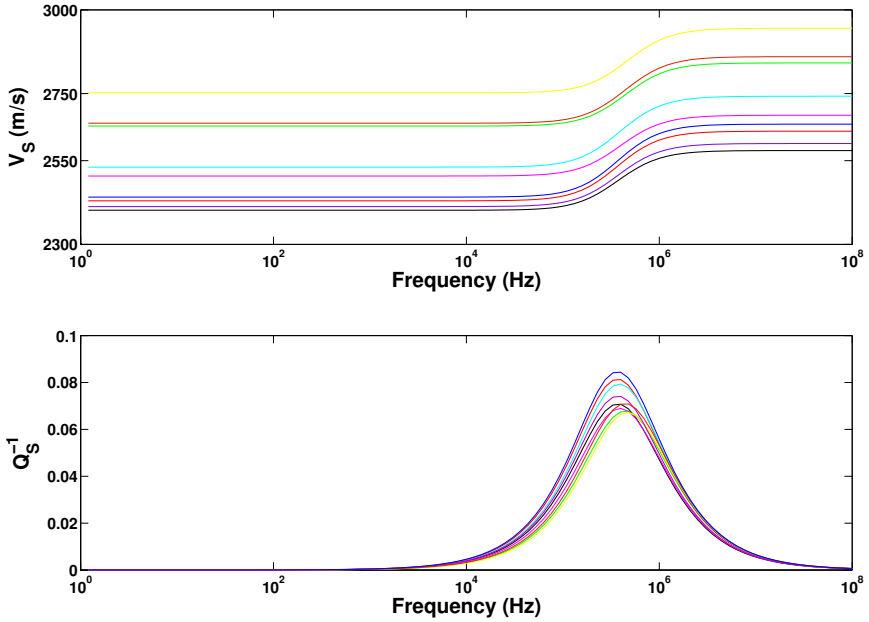

Figure 5b: V_S and Q_S^{-1} as functions of frequency with different mineralogy. Calcite (C), Dolomite (D) and Aragonite (A). The first letter corresponds to inclusion and the second to the matrix mineral. CC (black); CD (green); CA (red); DC (magenta); DD (yellow); DA (cyan); AC (brown); AD (pink) and AA (blue).

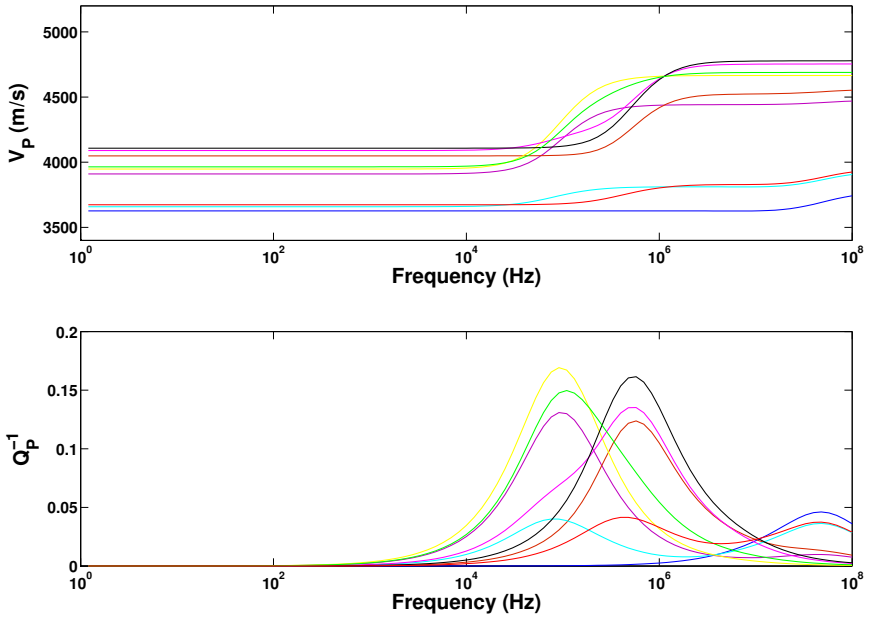

Figure 6a: V_P and Q_P^{-1} as functions of frequency and different fluids. Water (W), Oil (O) and Methane (M). The first letter corresponds to fluid in the micro porosity and the second letter to the meso porosity. WW (black); WO (green); WM (red); OW (magenta); OO (yellow); OM (cyan); MW (brown); MO (purple) and MM (blue).

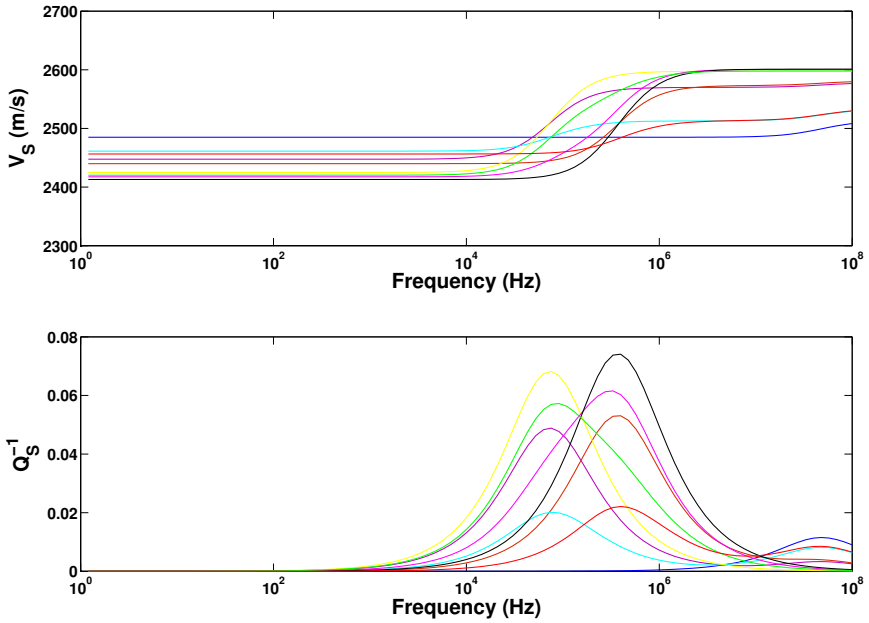

Figure 6b: V_S and Q_S^{-1} as function of frequency and different fluids. Water (W), Oil (O) and Methane (M). The first letter corresponds to fluid in the micro porosity and the second letter to the meso porosity. WW (black); WO (green); WM (red); OW (magenta); OO (yellow); OM (cyan); MW (brown); MO (purple) and MM (blue).

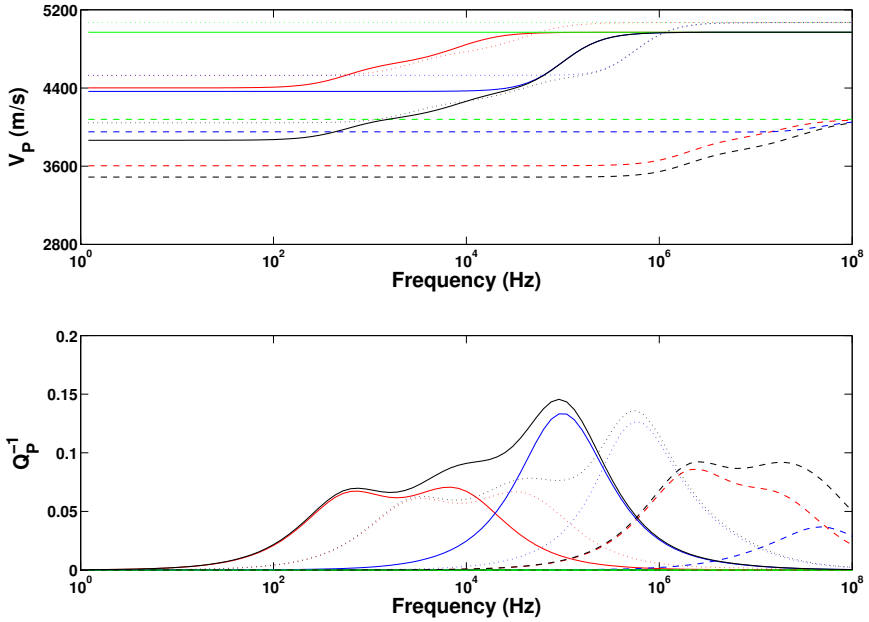

Figure 7a: V_P and Q_P^{-1} as functions of frequency with micro cracks saturated with different fluids: gas (dashed line), oil (solid line) and water (dotted line), and different connections: both micro and meso porosity connected (black), connected micro porosity and isolated meso porosity (red), connected meso porosity and isolated micro porosity (blue), both micro and meso porosity isolated (green).

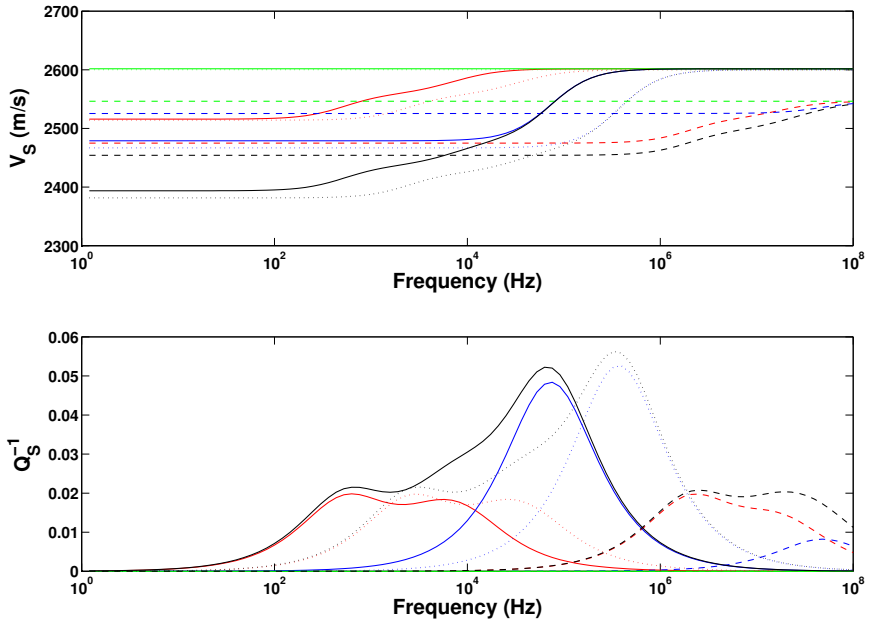

Figure 7b: V_S and Q_S^{-1} as functions of frequency with micro cracks saturated with different fluids: gas (dashed line), oil (solid line) and water (dotted line), and different connections: both micro and meso porosity connected (black), connected micro porosity and isolated meso porosity (red), connected meso porosity and isolated micro porosity (blue), both micro and meso porosity isolated (green).

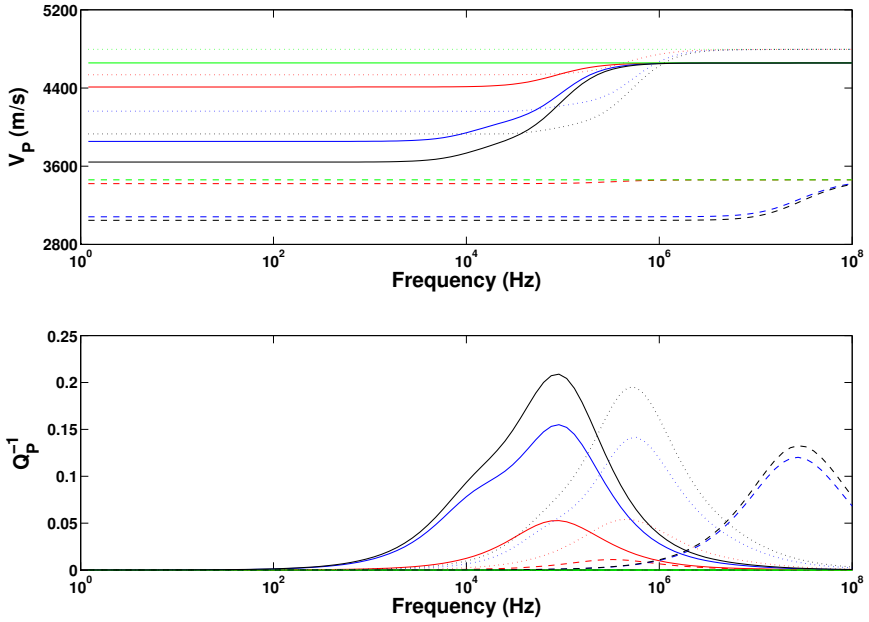

Figure 8a: V_P and Q_P^{-1} as functions of frequency with macro cracks saturated with different fluids: gas (dashed line), oil (solid line) and water (dotted line), and different connections: both micro- and macro porosity connected (black), connected micro porosity and isolated macro porosity (red), connected macro porosity and isolated micro porosity (blue), both micro- and macro-porosity isolated (green).

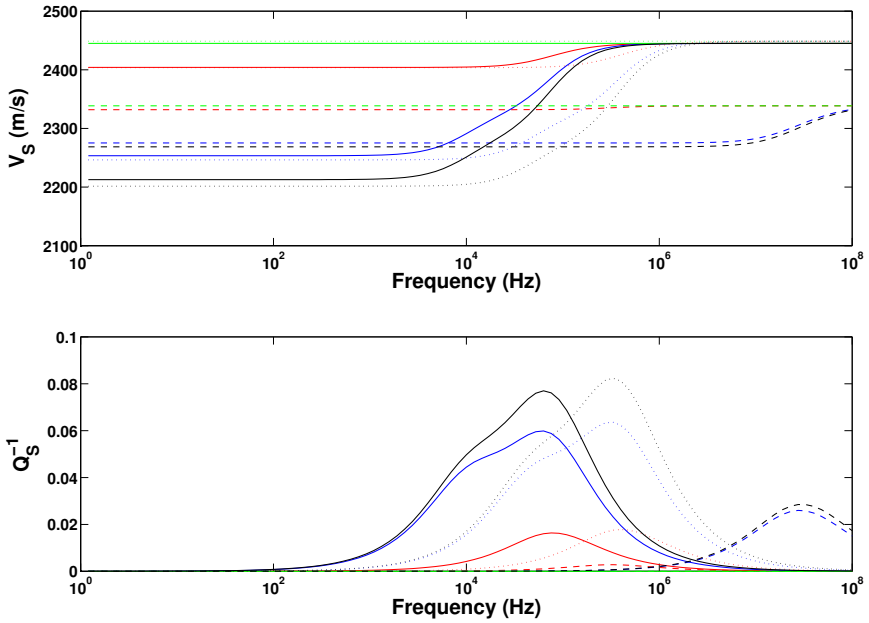

Figure 8b: V_S and Q_S^{-1} as functions of frequency with mesoscopic cracks saturated with different fluids: gas (dashed line), oil (solid line) and water (dotted line), and different connections: both micro and meso porosity connected (black), connected micro porosity and isolated meso porosity (red), connected meso porosity and isolated micro porosity (blue), both micro and meso porosity isolated (green).

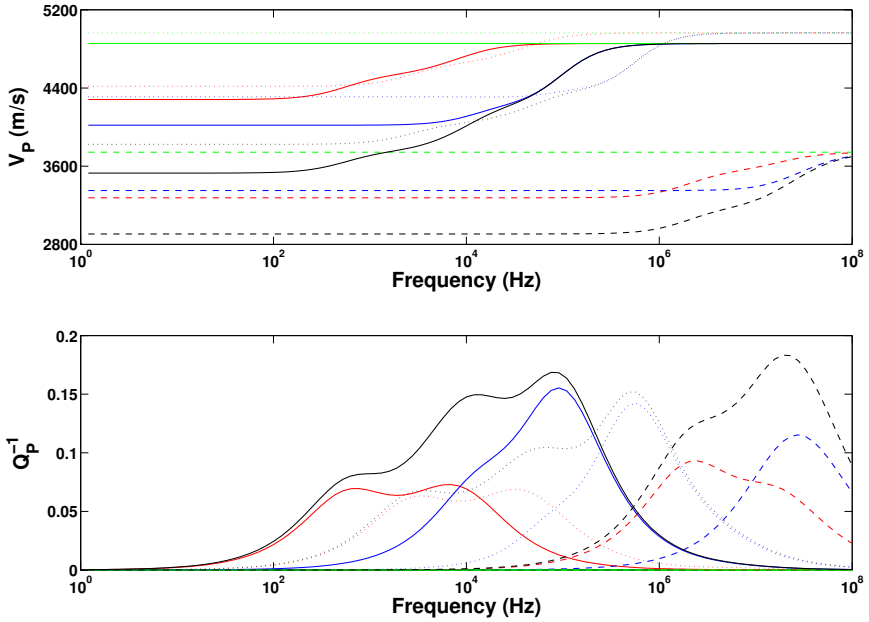

Figure 9a: V_P and Q_P^{-1} as functions of frequency with both micro and meso cracks saturated with different fluids: gas (dashed line), oil (solid line) and water (dotted line), and different connections: both micro and meso porosity connected (black), connected micro porosity and isolated meso porosity (red), connected meso porosity and isolated micro porosity (blue), both micro and meso porosity isolated (green).

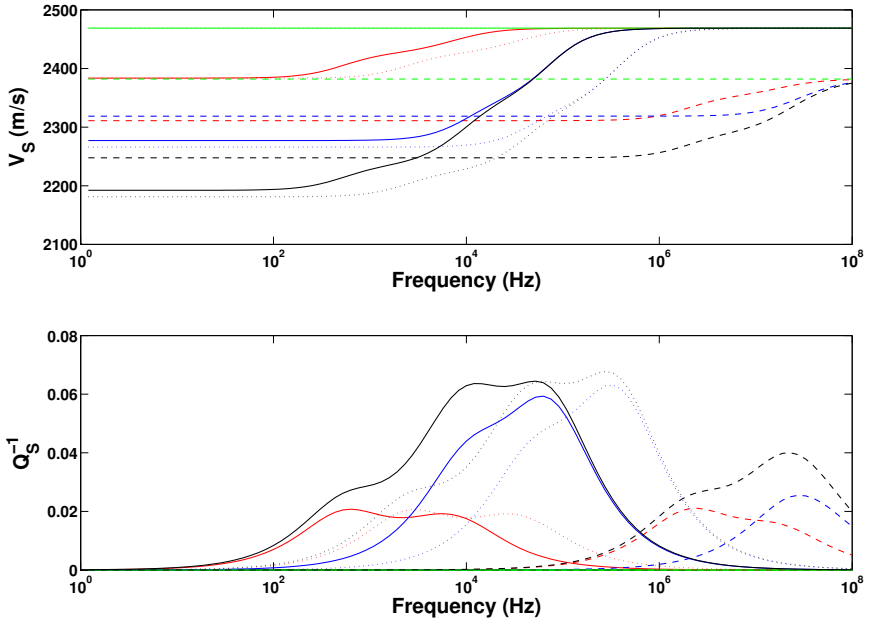

Figure 9b: V_S and Q_S^{-1} as functions of frequency with both micro and meso cracks saturated with different fluids: gas (dashed line), oil (solid line) and water (dotted line), and different connections: both micro and meso porosity connected (black), connected micro porosity and isolated meso porosity (red), connected meso porosity and isolated micro porosity (blue), both micro and meso porosity isolated (green).

Tables

	Calcite	Dolomite	Aragonite
Bulk modulus (GPa)	76.8	94.9	44.8
Shear Modulus (GPa)	32.0	45.0	38.8
Density (kg/m^3)	2710	2870	2920

Table 2: Properties of the minerals used in the calculations (compiled from Mavko, Mukerji and Dvorkin 1998).

	Water	Oil	Methane
V_P (m/s)	1554	1424.3	688.7
Density (kg/m^3)	989.1	854.2	206.5
Viscosity (cP)	1	6.4	0.029

Table 2: Properties of the fluids (compiled from Batzle and Wang 1992) used in the calculations. The temperature is 80^{0}C and the pore pressure is 40 MPa.

Microscopic porosity: $\varphi_{micro} = 0.23$		Mesoscopic porosity: $\varphi_{meso} = 0.11$	
Without cracks :		Without cracks:	
α	c	α	c
1	0.1	1	0.3[I)]
0.5	0.1	1	0.1
0.1	0.01	0.01	0.01
0.05	0.01		
0.01	0.01		
Including cracks:		Including cracks:	
α	c	α	c
1	0.21[II]	1	0.3[I]
0.1	0.01	1	0.099[II]
0.001	0.1[III]	0.01	0.01
0.0005	0.1[III]	0.001	0.1[III]
0.0001	0.1[III]		

Table 3: Aspect ratio (α) and concentration (c) of the micro and meso porosity for the examples. [I)] The micro porosity is incorporated in meso scale as spherical inclusions with relative concentrations. [II)] The concentration was determined so the total porosity with cracks was equal to the total porosity without cracks. [III)] Crack density. φ_{total} = 0.17.

Paper 2

EFFECTS OF FLUIDS AND DUAL PORE SYSTEMS ON VELOCITIES AND ATTENUATIONS OF CARBONATES

Remy Agersborg[1], Tor Arne Johansen[1], Morten Jakobsen[1], Jeremy Sothcott[2] and Angus Best[2]

ABSTRACT

In 4D seismic studies, the ability to differentiate between fluid and pressure effects is essential. The effects of fluid substitution on P- and S-wave velocities in carbonates of complex texture are still not fully understood. The often used Gassmann's equation has shown to give ambiguous results when compared with ultrasonic velocity data. We discuss theoretical modelling of velocity and attenuation measurements obtained for 6 carbonate samples, mainly made up of calcite, saturated with air, brine and one additionally with kerosene. Although both the porosities (2 – 14%) and permeabilities (0 - 74 mD) are relatively low, the velocity variations are large. S-wave velocities were measured for two orthogonal polarizations and some anisotropy was revealed. For some samples, the Gassmann model under-predicts the fluid substitution effects. Moreover, when dried they also show decreasing attenuation, with increasing confining pressure. To model this behaviour, we examine a pore model made up of two pore systems: one constituting the main and drainable porosity, and one made up of un-drained crack-like pores. Also, these dried rock samples were modelled to contain a fluid-filled pore system of crack-like pores potentially giving rise to local fluid flow and attenuation. For the theoretical modelling we use an inclusion model based on the T-matrix approach, which also considers the effects of texture, pore geometry, pore fluid and local fluid flow. By using a dual pore system, we succeeded in establishing a realistic physical model consistently describing the measured data.

[1] Department of Earth Science and Centre for Integrated Petroleum Research, University of Bergen, Allegt. 41 N-5006 Bergen, Norway. E-mail: remy.agersborg@geo.uib.no, torarne.johansen@geo.uib.no and morten.jakobsen@geo.uib.no.

[2] National Oceanography Centre, Southampton. E-mail: jsoth@noc.soton.ac.uk and aib@noc.soton.ac.uk.

INTRODUCTION

The complex nature of carbonate rocks can lead to ambiguous conclusions when interpreting seismic data for reservoir characterisation. For example, the seismic properties of carbonate rocks are affected by many parameters such as pore type and shape, porosity and pore fluid (Wang, 1997) making it difficult to attribute changes in seismic expression to any one parameter. Also, the debate is ongoing on the validity of using Gassmann's equation (Gassmann, 1951) for studying the seismic effects of various pore fluids. Adam et al. (2006) show that fluid effect predictions using Gassmann (1951) are consistent within the uncertainties of the measured data for some of their carbonate samples. Baechle et al. (2005), Rossebø et al. (2005) and Assefa et al. (2003) observed an alteration in the shear modulus with fluid substitution, violating one assumption of the Gassmann model. In the study of Wang (2000), measurements and Gassmann predictions of the P-wave velocity deviate significantly at low effective pressures, although they converge with increasing effective pressure. This convergence is caused by the closing of compliant, crack-like pores with increasing effective pressure, making the remaining pore system better connected and in closer agreement with the Gassmann assumptions.

The velocity dispersion of fluid-filled rocks is mainly due to viscous pore fluid flow. The fluid flow relaxation time is the time needed for the pore pressure to equilibrate throughout the pore volume, when a fluid-filled porous material is strained. For dynamic strains, a low-frequency response is produced when the fluid flow relaxation time is a magnitude less than the period of the strain impulse. A high frequency response is produced when the relaxation time is a magnitude larger, while an intermediate response results when the two quantities are comparable in magnitude. Whether we can expect a low-, intermediate- or high-frequency response when performing an ultrasonic wave propagation experiment will depend on the fluid mobility, which is the ratio of permeability of the rock to the viscosity of the pore fluid. Moreover, the fluid mobility determines the pore-pressure distribution as a passing seismic wave yields a small deformation in the rock (Batzle et al., 2006).

The main wave attenuation mechanisms at ultrasonic frequencies are scattering from pores and grains, and pore fluid flow. While scattering attenuation increases with frequency, attenuation due to pore fluid flow reaches a maximum for frequencies lying in between the low- and high-frequency responses (Biot, 1956a,b). At intermediate frequencies, the pore fluid is in non-equilibrium state, and several assumptions of the Gassmann model are violated. In such cases visco-elastic models need to be considered. This is especially true for carbonate rocks where the porosity and texture are the primary controlling factors for velocity

(Eberli et al., 1997). Frequency dependent inclusion models are good candidates for describing carbonate rocks.

In this paper we focus on rock physics modelling of measured P- and S-wave velocities and attenuations of 6 calcite rock samples. For the theoretical modelling we use the results of Jakobsen et al. (2003a,b) and Jakobsen and Johansen (2005), while the velocity and attenuation data were obtained using the ultrasonic P- and S-wave pulse-echo technique described by McCann and Sothcott (1992) and Best et al. (1994). We start by briefly describing the rock samples, the measurements and some observations, before the formalism and procedure for the theoretical modelling are outlined. We then discuss the idea of using a dual pore system to describe some of the observations where the Gassmann model appears to fail.

EXPERIMENTS AND OBSERVATIONS

The set of rock samples were collected from a well bore taken in a limestone formation at approximately 2 km depth. From a set of 26 samples, 6 core plugs of diameter 5 cm and length 2-3 cm were carefully selected to give a representative spread of lithological variations, porosity (2 to 14%) and permeability (0 to 74 mD). Before the porosities and permeabilities were measured, the samples were vacuum dried but not cleaned. Some details of the six samples are given in Table 1.

Velocities and attenuations were measured for various confining pressures at constant pore pressure by using an ultrasonic pulse-echo technique described by McCann and Sothcott (1992) on dried samples, which were saturated subsequently with brine (all samples) and kerosene (sample 6 only). For both the P and S waves a frequency of 750 kHz was applied. The pulse-echo system was installed inside an ITR Triaxial Hoek high pressure cell (Assefa, 1994) and the confining pressure was starting at 5 or 10 MPa, rising in steps of 10 MPa up to 60 MPa. For each pressure level, two-way travel times of the P and S waves were measured after 30 minutes had elapsed to allow pressure equilibration. The S-wave transducer was rotated for each step and minimum and maximum travel times were assigned 0^0 and 90^0 relative to the lamination directions at cylinder ends, as illustrated in Figure 1. The core plugs were cleaned between each fluid substitution, and for the saturated samples the pore fluid pressure was maintained at 5 MPa. The velocity was calculated by

$$V = \frac{2L}{t_{av}}, \tag{1}$$

where t_{av} is the average two-way travel time and L is the length of the rock sample. The quality factor was derived from

$$Q = 8.686\frac{\pi f}{V\alpha}, \tag{2}$$

where f is the frequency of the wave. The attenuation coefficient α is found from

$$\alpha = \frac{8.686}{2L}\ln\left(\frac{A_1}{A_2}(1-R_{12}^2)\right) = \frac{1}{2L}20\log_{10}\left(\frac{A_1}{A_2}(1-R_{12}^2)\right). \tag{3}$$

Here A_1 and A_2 are the amplitudes of the first and second reflection, respectively, and R_{12} is the reflection coefficient at the buffer rod/sample interface.

For all velocity measurements (shown in Figure 2), a general trend found is that the velocities are increasing with increasing confining pressure, which mainly is due to closing of cracks. Sample 1 has the largest differences between highest and lowest velocities for both dried and brine saturated samples. For P waves they are 615 m/s (brine) and 896 m/s (dried), and for S waves they are 318 m/s (brine) and 323 m/s (dried). Sample 3 showed the smallest differences, where for P waves they are 30 m/s (brine) and 125 m/s (dried), and for S waves they are 30 m/s (brine) and 45 m/s (dried). Sample 4 shows an almost linear increase in velocity with increasing pressure. This may be because the sample consists of cracks with a large distribution of aspect ratios (crack-like pores) or that the sample has a relative small amount of high aspect ratio (near spherical) pores. For sample 5, the velocities show a rapid increase with pressure for then to level out with further increasing pressure. This suggests that there may be cracks with a narrow distribution of small aspect ratios, which all close at a certain pressure.

Since mainly the cracks (which accounts only for a small fraction of the total porosity) are closing as the pressure increases, the component of elasticity due to scattering should not change significantly as the pressure changes. The attenuation measurements (shown in Figure 3), however, show a significant change as the effective pressure increases. We interpret this observation through the effects of wave induced fluid flow. Only sample 2 does not show any change in attenuation with pressure. Even though there is pressure dependent attenuation, we cannot be certain whether there is an extra overall attenuation component due to the inelastic properties of the matrix material. Furthermore, the attenuations become close to constant when the effective pressure exceeds 30 MPa. This also indicates an overall inelastic term embedded in the effective properties of the samples.

We made no assumptions about elastic symmetry planes within the core plugs prior to the measurements. Thus, the S-wave velocities were measured by rotating the receivers for 0^0 and 90^0 relative to bedding at cylinder ends. Supported later by the modelling where S-wave splitting was detected, we have assumed a horizontal transverse isotropy, with a symmetry axis orthogonal to the direction of the fastest S-wave, as indicated in Figure 1. From the velocity plots in Figures 4 - 11, some anisotropy can be observed. Sample 1 revealed some pressure dependent anisotropy: the anisotropy decreases with increasing effective pressure, and vanishes above 20 MPa pressure. Sample 3 did not show any anisotropic behaviour.

The perhaps most interesting observation is that several of the dried samples (1, 3, 4, 5 and 6) show a similar qualitative behaviour with respect to attenuation as when they are brine saturated. Since the attenuation decreases with increasing pressure, we consider this also as an effect caused by the closing of cracks. The closing of cracks will reduce both the amount of wave scatterers, but we may also associate this reduction in attenuation with the closing of a network of un-drained low-aspect ratio pores. This latter assumption is later to be supported by the theoretical modelling results. The measured attenuation also indicates that the measurements correspond to an intermediate or high frequency fluid response because of the pressure dependency. Furthermore, a preliminary test, using Gassmann (1951) to compute dry rock P-velocity from the brine saturated rock P-velocity, measured porosity and elastic properties of the calcite, gives a fluid effect that is too small at lower pressures. Thus, the measured P velocities of the brine saturated samples seem to be increased by local fluid flow phenomena in the crack-like pores.

THEORY AND PROCEDURE BEHIND MODELLING

Here, we apply the visco-elastic effective medium theory of Jakobsen et al. (2003a,b) to the data. A homogeneous matrix material is embedded with inclusions of the same scale, which are divided into families having the same concentrations and shape/orientations, labelled by r = 1,2,…,N. Where cavities are labelled by r = 1,2,…,Nc and solid inclusions by r = Nc+1,…,N. The effective stiffness $\mathbf{C}^*$ is given by (Jakobsen et al., 2003a,b)

$$\mathbf{C}^* = \mathbf{C}^{(0)} + \mathbf{C}_1(\mathbf{I}_4 + \mathbf{C}_1^{-1}\mathbf{C}_2)^{-1}, \tag{4}$$

$$\mathbf{C}_1 = \sum_{r=1}^{N} \mathrm{v}^{(r)}\mathbf{t}^{(r)}, \tag{5}$$

$$\mathbf{C}_2 = \sum_{r=1}^{N}\sum_{s=1}^{N} \mathrm{v}^{(r)}\mathbf{t}^{(r)}\mathbf{G}_d^{(rs)}\mathbf{t}^{(s)}\mathrm{v}^{(s)}, \tag{6}$$

where $\mathbf{C}^{(0)}$ is the fourth-rank stiffness tensor of the homogeneous matrix material, $\mathbf{I}_4$ is the identity for fourth-rank tensors, $v^{(r)}$ is the volume concentration for inclusion of type r, $\mathbf{t}^{(r)}$ is the t-matrix, $\mathbf{G}_d^{(rs)}$ is given by the strain Green's functions integrated over a characteristic ellipsoid having the same symmetries as $p^{(s|r)}(\mathbf{x}\text{-}\mathbf{x}')$ which, in turn, gives the probability density for finding an inclusion of type s at point $\mathbf{x}'$ given there is an inclusion of type r at point $\mathbf{x}$. The t-matrix of a single inclusion of type r is given by (Jakobsen et al., 2003a,b)

$$\mathbf{t}^{(r)} = (\mathbf{C}^{(r)} - \mathbf{C}^{(0)})[\mathbf{I}_4 - \mathbf{G}^{(r)}(\mathbf{C}^{(r)} - \mathbf{C}^{(0)})]^{-1} \quad , \tag{7}$$

where $\mathbf{C}^{(r)}$ is the stiffness tensor for the inclusion and $\mathbf{G}^{(r)}$ is a fourth rank tensor depending only on the aspect ratio of the inclusion and $\mathbf{C}^{(0)}$.

T-matrix/communicating cavities

We will only list the important t-matrix equations where these effects are incorporated and used in this paper. A detailed derivation can be found in Jakobsen et al. (2003b).

For a single communicating cavity (fully fluid saturated), which is allowed to exchange fluid mass with other cavities, the t-matrix can be expressed as a dry t-matrix and a term which take into account the fluid effects (Jakobsen et al., 2003a,b)

$$\mathbf{t}^{(r)} = \mathbf{t}_d^{(r)} + \frac{\Theta \mathbf{Z}^{(r)} + i\omega\tau\kappa_f \mathbf{X}^{(r)}}{1 + i\omega\gamma^{(r)}\tau}, \tag{8}$$

$$\mathbf{X}^{(r)} = \mathbf{t}_d^{(r)}\mathbf{S}^{(0)}(\mathbf{I}_2 \otimes \mathbf{I}_2)\mathbf{S}^{(0)}\mathbf{t}_d^{(r)}, \tag{9}$$

$$\mathbf{Z}^{(r)} = \mathbf{t}_d^{(r)}\mathbf{S}^{(0)}(\mathbf{I}_2 \otimes \mathbf{I}_2)\mathbf{S}^{(0)}\left(\sum_{r=1}^{N_c} \frac{v^{(r)}\mathbf{t}_d^{(r)}}{1 + i\omega\gamma^{(r)}\tau}\right), \tag{10}$$

$$\Theta = \kappa_f \left\{ \left(1 - \kappa_f S^{(0)}_{uuvv}\right)\left(\sum_{r=1}^{N_c} \frac{v^{(r)}}{1 + i\omega\gamma^{(r)}\tau}\right) + \kappa_f \left(\sum_{r=1}^{N_c} \frac{v^{(r)}(K_d^{(r)})_{uuvv}}{1 + i\omega\gamma^{(r)}\tau}\right) - \frac{ik_u k_v \Gamma_{uv}\kappa_f}{\eta_f \omega} \right\}^{-1}, \tag{11}$$

$$\gamma^{(r)} = 1 + \kappa_f \left(K_d^{(r)} - S^{(0)}\right)_{uuvv}, \tag{12}$$

$$\mathbf{K}_d^{(r)} = \left(\mathbf{I}_4 + \mathbf{G}^{(r)}\mathbf{C}^{(0)}\right)^{-1}\mathbf{S}^{(0)}. \tag{13}$$

Here $\mathbf{t}_d^{(r)}$ is the t-matrix for the dry cavity of family r, $\mathbf{S}^{(0)} = \left(\mathbf{C}^{(0)}\right)^{-1}$, ω is the frequency, τ is the relaxation time constant, κ_f and η_f are the bulk modulus and viscosity of the fluid, k_u and k_v are components of the wave number vector, Γ_{uv} is the permeability tensor of the rock and the subscription u and v represent summation over u and v, respectively (u,v = 1,2,3). $\mathbf{I}_2$ is a second rank tensor and $\otimes$ denotes a dyadic tensor product.

Effect of pressure

Two assumptions were made to capture the features of the microstructure under evolution when subjected to a finite deformation. First, the applied effective stress is triaxial with axes coinciding with the symmetry axes of the medium, then the inclusions which are ellipsoidal in shape and will deform into ellipsoids when they are subjected to uniform drained loading conditions.

The change in volume $\partial v^{(r)}$ and aspect ratio $\partial \alpha^{(r)}$ of cavity of type r due to a small increment in the effective strain $\boldsymbol{\varepsilon}$ is given by Jakobsen et al. (2005)

$$\frac{\partial v^{(r)}}{v^{(r)}} = \partial \varepsilon_{kk}^{(r)} - \sum_{s=0}^{N_c} v^{(s)} \partial \varepsilon_{kk}^{(s)}, \tag{14}$$

$$\frac{\partial v^{(r)}}{v^{(r)}} = \left[\left(K_{d*}^{(r)} \right)_{kkpq} - \sum_{s=0}^{N_c} v^{(s)} \left(K_{d*}^{(s)} \right)_{kkpq} \right] \left(\partial < \sigma >_a^{(r)} \right)_{pq}, \tag{15}$$

$$\frac{\partial \alpha^{(r)}}{\alpha^{(r)}} = \partial \varepsilon_{33}^{(r)} - \partial \varepsilon_{11}^{(r)}, \tag{16}$$

$$\frac{\partial \alpha^{(r)}}{\alpha^{(r)}} = \left[\left(K_{d*}^{(r)} \right)_{33pq} - \left(K_{d*}^{(r)} \right)_{11pq} \right] \left(\partial < \sigma >_a^{(r)} \right)_{pq}. \tag{17}$$

Here k,p,q represent summation (k,p,q = 1,2,3), $\mathbf{K}_{d*}^{(r)}$ is the effective dry K-tensor and is given by (Jakobsen and Johansen, 2005)

$$\mathbf{K}_{d*}^{(r)} = \left(\mathbf{I}_4 - \mathbf{G}^{(r)} \mathbf{C}^{(0)} \right)^{-1} \left(\mathbf{I}_4 + \mathbf{C}_{d1}^{-1} \mathbf{C}_{d2} \right)^{-1} \mathbf{S}_d^*, \tag{18}$$

where the fourth-rank tensors $\mathbf{S}_d^* = \left(\mathbf{C}_d^* \right)^{-1}$, $\mathbf{C}_{d1}$ and $\mathbf{C}_{d2}$ can be found from equation (4) – (6) by using the t-matrix formulation (equation (4)) for dry inclusions. The apparent stress, $\partial < \sigma >_a^{(r)}$, is given as (Jakobsen and Johansen, 2005)

$$\partial < \sigma >_a^{(r)} = \partial < \sigma > + \delta p_f \varsigma^{(r)}, \tag{19}$$

where $\partial < \sigma >$ is the effective stress and the second-rank tensor of apparent stress coefficients is

$$\varsigma^{(r)} = \mathbf{I}_2 - (\mathbf{K}_{d*}^{(r)})^{-1} \mathbf{S}^{(0)} \mathbf{I}_2 . \tag{20}$$

SINGLE AND DUAL PORE SYSTEMS

If the dried samples still contain some fluid in a fully or partly un-drained network of cracks, the modelling of the effective properties must include the effects of this fluid. Essentially there are three possible ways the pore fluid can be distributed within the porosity.

It can, either be partially saturating the pores and cracks, or completely saturating parts of the porosity, or a combination of 1 and 2. In the further modelling we shall assume that the porosity is divided into two separate pore systems which are isolated with respect to each other. One pore space contains a variety of pore aspect ratios, and the pores constitute close to all the open porosity, i.e. the pore space is possible to drain and re-fill with another pore fluid. The other pore space is a network of crack-like pores (low aspect ratios) which is not drained through the fluid substitution processes. Similar geometrical models for two-fluid distributions were also discussed by Johansen et al. (2002).

We now associate the remaining fluid in the dried samples with the closed (un-drainable) porosity. This can be found from the densities of the brine saturated sample $\rho_{brine-sat}$, calcite mineral $\rho_{mineral}$, and the grain ρ_{grain} according to Mavko et al. (1998). Here the grain density means the density of the mineral including the closed or remaining porosity ϕ_R. The measured porosity is denoted ϕ_M, and the relevant relations read

$$\rho_{brine-sat} = (1-\varphi_M)\rho_{grain} + \varphi_M\rho_{brine}, \tag{21}$$

$$\rho_{grain} = (1-\varphi_R)\rho_{mineral} + \varphi_R\rho_{brine}. \tag{22}$$

From equation (22), we find the remaining porosity of the core plug to be

$$\varphi_R = \frac{\rho_{grain} - \rho_{mineral}}{\rho_{brine} - \rho_{mineral}}. \tag{23}$$

Combining equations (21) and (22) gives the total porosity

$$\varphi_{tot} = \varphi_M + \varphi_R - \varphi_M\varphi_R. \tag{24}$$

Here, the last term may be considered as a correction term for the difference between the grain density and the mineral density.

MODELLING APPROACH

An ideal approach for predicting the acoustic responses of the core plugs, using the T-matrix formalism, is first to invert for the distribution of pores and cracks of the dry sample, and then to estimate the relaxation time constant τ (see eqs. (8) and (10)) for the saturated sample. Since we still assume that there may be some fluid left in most of the dried samples and also that the distribution of the fluid in the cavities is unknown, we have used a three step procedure in the further modelling. In the following, we use the analysis of sample 1 data as a tutorial for this approach.

Step 1. By using the total porosity derived from equation (24) and a distribution of the cracks according to equation A-1 (and Figure 4a) together with some additional pores (of

aspect ratio 0.23) we first obtain a model for the saturated sample. In this model the porosity is fully connected and randomly oriented as illustrated in Figure 4b. Figure 4c shows a good fit for the brine saturated P-wave velocity, while when substituting brine with air the fit is strongly pressure dependent: for low pressures, the measured dry rock velocities are larger than the predicted, while with increasing pressure (above 25 MPa) and reducing amount of cracks, the fit becomes much better. The reduction of crack-like pores reduces the local fluid flow effects and makes the overall pore fluid response to be of low-frequency type, corresponding with the Gassmann model. If we believe that the established pore system used for describing the saturated sample is correct, this is another indication that the dried rock contains a portion of fluid-filled cracks which stiffen the (dry) rock and contribute to the observed attenuation. The increasing correspondence between observation and modelling of the dried and saturated rock at high pressures is in accordance with previous observations (Wang, 2000).

For the S-wave, which is less influenced by fluid, the velocity trend of the modelling is about 100 m/s off the measured (Figure 4d). The S-wave attenuation for the brine saturated model of sample 1 is shown in Figure 4e.

Step 2. Failing to describe the P-wave velocity for the dried case at low pressures, and the fact that the porosity may contain about 1.6% brine according to equation (24), we now divide the porosity into two individually connected pore systems which are considered isolated with respect to each other for fluid flow associated with seismic waves (Figure 5b). The crack distribution is the same as the original one, but because the P-wave velocity of the dried sample matches the data above 25 MPa quite well (Figure 4c), we define the un-drained pore system (with a porosity of 1.6%) to be made up of the lowest aspect ratio pores as illustrated in Figure 5c. As the confining pressure slowly increases (near static limit) and the fluid-filled cracks close, the pore fluid is now drained into the dry pore system in order to maintain mass balance. However, we do not consider this to affect the behaviour of the dry pore system, since the effective bulk modulus of the fluid of vacuum with a small fraction of brine is very close to zero. The theoretical modelling now succeeds also to match both the dried and saturated sample, except for a bend at about 20 MPa pressure at which the un-drained pore system completely closes. Figure 5d shows that the dual pore system imposes almost no effect on the S-wave velocity, while in Figure 5e we see some attenuation even for the dried sample.

Step 3. In order to remove the artificial bend caused by the abrupt closing of fluid-filled cracks (see Fig. 5c), we redistribute the saturated part of the crack distribution so that

there is a gradual fractional decrease of un-drained cracks with increasing aspect ratio, as shown in Figure 6a and 6b. Also, since the S-wave velocities are about 100 m/s off the measured velocities, and since they are relative insensitive to the fluid, we reduce the S-wave velocity of the mineral by this value. As Figure 6c shows, that using this new un-drained pore system, the dried and brine saturated P-wave velocity of sample 1 can be reproduced quite accurately. In Figure 6d S-wave velocities are plotted, while Figure 6e shows the corresponding attenuations of both P and S waves.

In the further modelling of the core plugs, the following model parameters were allowed to be slightly adjusted to obtain a best fit between the modelling and data: P- and S-wave velocities of the mineral (calcite) by $\pm$ 100 m/s due to possible heterogeneity effects, the porosity according to equation (24), and the τ-parameter controlling the characteristic frequency due to squirt flow.

For comparison, we have calculated the P velocities of the dried core plugs using the Gassmann equation (appendix B) from velocities obtained at saturated state. Since no off-axis velocities were measured, we did not use the anisotropic version of Gassmann's equation for the samples where anisotropy was measured. The deviation from the calculated and measured values is given as

$$\text{Deviation} = \frac{V_{P\,(\text{Gassmann})} - V_{P(\text{measured})}}{V_{P(\text{measured})}} 100\%.$$

RESULTS

In the following, we describe the measurements and analyses of the six samples. The modelling procedures were outlined in the previous section, with the analyses of sample 1 as a tutorial. Tables 1 to 4 summarize the parameters found to give an adequate fit between the measured and modelled data. Table 2 reveals for each sample the effective calcite properties, total and dry porosity, permeability, and the deviation of our modelling using a dual pore system compared to results obtained from the Gassmann model considering either dry or saturated samples. Table 3 provides the values of the τ-parameter, related to the fluid-to-solid coupling, and the pore system: Here ε_0 denotes the total crack density, $\overline{\alpha}$ is the mean aspect ratio of the crack distribution, δ is a parameter which dictates the spread of the crack distribution and u is the upper aspect ratio of the crack distribution. α^* denotes the aspect ratio of the pores which are either dry or fluid-filled, while the distribution function with parameters p_i, $i=0,\ldots,n$ defined as $p_i = p_{i-1}e^{-a}$ for $p_{i-1} > c$ and $p_i = p_{i-1}e^{-b}$ for $p_{i-1} \le c$.

The results of sample 1 of porosity 13.35% is given in Figure 6. Figure 7 reveals the results of sample 2 of porosity 9.07%. The P-wave attenuation (Fig. 7d) is seen to be close to constant with pressure. Furthermore, the P-wave velocity (Fig. 7b) difference between low and high effective pressures is much greater for dry pores compared to the brine saturated case. This should indicate that the sample is completely dry, or, at least, that the volume fraction of the remaining fluid is very small. The S-velocity (Fig. 7c) for brine saturation is greater than for dried sample for effective pressures up to about 20 MPa, while at higher pressures the situation is opposite. This again points to a possible existence of a tiny portion of very thin cracks which due to wave induced fluid increases the shear modulus for lower pressures. The effect vanish as these pores close with increasing pressure, and the S-velocity differences between dry and brine saturation will be due to changes in the effective density. Also the crack distribution (Fig. 7a) for the fitted model of sample 2 becomes practically zero for aspect ratios larger than 0.003. In this case the porosity is fully connected and completely dry, while 30% of the crack distribution up to aspect ratio 0.0056 is defined vertically aligned.

Figure 8 shows the results obtained for sample 3 of porosity 2.76%. Here there are little changes in the measured P- and S-wave velocities (Figs 8b and c) as the effective pressure increases. The measured attenuations (Fig. 8d) show almost no changes for the saturated sample, but when dried the attenuation decreases rapidly with lowered effective pressure before levelling out. Again, for the modelling this imposed some remaining fluid in the cracks with very low aspect ratios closing at pressures above 20 MPa. Pores with aspect ratio 0.25 of concentration of 0.02 were added, while divided into a dry (with concentration of 0.0058) and a saturated fraction. In addition pores with aspect ratio 0.95 were included such that the total porosity reached 2.76%. No S-wave splitting was seen for this sample, and thus, a random distribution of the crack-like pores was used.

Figure 9 shows the results of sample 4 of porosity 4.91%. There is a small P-velocity difference (Fig. 9b) between the dried and brine saturated samples as the effective pressure increases. This indicates a high concentration of the stiffer pores (and cracks). Also a greater S-wave splitting is observed for the dried compared with the saturated sample (Fig. 9c). This may be due to either that the shear modulus is altered with pore content, or that the pore system has been modified through the pressure cycle, or a combination of both. In this case, 10% of the crack distribution for aspect ratios up to 0.0028 was defined vertical aligned. The pores with aspect ratio 0.4 and concentration 0.02 were added, while divided into a dry (with concentration of 0.0015) and a saturated fraction. Furthermore, pores with aspect ratio 0.9 were further added to obtain a total porosity of 4.91%.

The data for sample 5 are given in Figure 10. In this case the measured porosity of 13.97% was by eq. (21-24) adjusted to 16.02%. The measured dried and brine saturated P velocities (Fig. 10b) level out when the effective pressure reaches above 20 MPa. The steep increase in P-velocity of the dried sample indicates a narrow distribution of aspect ratios describing the cracks, which all close when the effective pressure reaches about 20 MPa. The similar picture is seen for the S-wave data (Fig. 10c), where the dried and saturated samples have close to equal S velocities for low effective pressures, while a constant difference after the cracks are closed. The crack distribution was re-distributed into 80% dry and 20% saturated cracks (Fig. 10a). Also 5.5% of the crack distribution for aspect ratios up to 0.0028 is vertically oriented. Here a portion of pores with aspect ratio 0.2 and concentration of 0.035 was included, and divided into dry (with concentration 0.0205) and saturated pores. To obtain a total porosity of 16.02%, pores with aspect ratio 0.32 were added.

Velocity and attenuation data for sample 6 were obtained both when dried, brine and kerosene saturated as shown in Figure 11. Both the P and S velocities (Figures 11b and c) increase gently as the effective pressure increases. However, this is not true for the S-velocity for the brine saturated sample for the 90^0 component. The estimated dry rock bulk modulus applying the Gassmann equation based on the P-velocity obtained from the brine-saturated sample, even turns out to be negative. This unexpected observation may indicate an alteration in shear modulus**.** To obtain the data fit, it was needed to define 20% of the crack distribution of aspect ratios up to 0.0048 vertically oriented. Here we chose first to fit the velocity data measured for kerosene, due to the deviating S-velocity data in case of brine saturation. Then the model was adjusted to fit the data of the dried sample, before the data of the brine saturated sample were predicted. The model is seen to fairly well describe the data obtained for dried and kerosene saturated samples, while the predictions for the brine saturated case are less successful. However, this is an effect of assuming the relaxation time constant to be independent of the fluid properties, which it is not. Hence, a better match is obtainable by estimating a new τ-parameter for the brine saturated model.

CONCLUSIONS

The aim of this study has been to investigate a physical model for predicting fluid effects on seismic properties of carbonate rocks with some fraction of hardly drainable cracks. The presence of cracks often implies high-frequency fluid flow response to seismic waves, and also that the Gassmann equation occurs less appropriate for understanding fluid effects. Measurement and theoretical modelling of velocities and attenuations of 6 carbonate core

plugs have been presented. Even though the porosity and permeability of the samples, mainly consisting of calcite, are relatively low, there is a large variation in the signatures of both velocity and attenuation. Pressure dependent attenuation of the dried samples is believed to be caused also by wave induced fluid flow from a small fraction of un-drained pores. Observed differences in velocities of S-waves with orthogonal polarization directions also reveal anisotropy and aligned pore structure properties.

We have used the so called T-matrix formalism to model both the velocity and attenuation data. To account for attenuation of dried samples, a dual pore model was applied. This includes one open pore system of connected and drainable pores, and one de-coupled and closed system which is not. While the open pore system includes the main fraction of the porosity which is made up of spherical and crack-like (low aspect ratio) pores, the closed system holds a minor fraction of the porosity constituted by crack-like pores only. To account for anisotropy a portion of the crack-like pores were defined to be aligned. The modelling succeeded in obtaining correlations of a microscopic description of the rock, also including various fluid properties, and a range of measured physical responses. The modelled fluid effects on velocity data were also compared to similar predictions using the Gassmann equation. Deviations between the two models varied from close to zero and up to 5 percent.

The modelling approach presented should be relevant for understanding the influence of the combined fluid-pore system on seismic properties of carbonates, which is crucial for using seismic data in reservoir monitoring of such rocks.

ACKNOWLEDGEMENTS

We would like to thank Hydro for providing the core material, and financing of both the PhD scholarship to Remy Agersborg and the experimental work.

APPENDIX A – The crack distribution

The crack distribution used in this paper is a generalized beta probability function multiplied with a total crack density. The crack density function can be written as (Tod, 2001)

$$\varepsilon(\alpha) = \varepsilon_0 F_\beta(\alpha, \overline{\alpha}, \delta, u), \tag{A-1}$$

Where ε is the crack density, ε_0 is the total crack density, α is the aspect ratio, $\overline{\alpha}$ is the mean aspect ratio, δ is a parameter which controlling the shape together with $\overline{\alpha}$, u is where the distribution end and the generalized beta probability function F_β can be written as (Tod, 2001)

$$F_\beta(\alpha,\bar{\alpha},\delta,u)=\frac{1}{u}\frac{\Gamma(p+q)}{\Gamma(p)\Gamma(q)}\left(1-\frac{\alpha}{u}\right)^{q-1}\left(\frac{\alpha}{u}\right)^{p-1}, \tag{A-2}$$

where

$$p=\frac{u-\bar{\alpha}-\bar{\alpha}\delta^2}{u\delta^2} \tag{A-3}$$

and

$$q=\frac{u-\bar{\alpha}}{\bar{\alpha}}p. \tag{A-4}$$

APPENDIX B – Gassmann's equation

The dry bulk modulus can be related to the saturated bulk modulus of the rock according to (Gassmann, 1951)

$$K_{sat}=K_{dry}+\frac{\left(1-\frac{K_{dry}}{K_0}\right)^2}{\frac{\phi}{K_{fl}}+\frac{1-\phi}{K_0}-\frac{K_{dry}}{K_0^2}}. \tag{B-1}$$

Or the dry bulk modulus related to the saturated bulk modulus as

$$K_{dry}=\frac{K_{sat}\left(\frac{\phi K_0}{K_{fl}}+1-\phi\right)-K_0}{\frac{\phi K_0}{K_{fl}}+\frac{K_{sat}}{K_0}-1-\phi}. \tag{B-2}$$

Here the dry and saturated shear modulus, μ, is assumed to be the same. K_{sat} is the effective bulk modus of saturated rock, K_{dry} is the effective bulk modulus of the dry rock, ϕ is the porosity, K_{fl} is the effective bulk modulus of the fluid and K_0 is the bulk modulus of the mineral.

The P-wave velocity can be calculated from

$$V_P=\sqrt{\frac{K+(4/3)\mu}{\rho}} \tag{B-3}$$

Where ρ is the effective density, K is the effective bulk modulus and μ is the effective shear modulus ($\mu_{dry}=\mu_{sat}$).

REFERENCES

Adam, L., Batzle, M. and Brevik, I., 2006, Gassmann's fluid substitution and shear modulus variability in carbonates at laboratory seismic and ultrasonic frequencies: Geophysics, **71**, F173-F183.

Assefa, S., 1994, Seismic and petrophysical properties of carbonate reservoir rocks: Ph.D. thesis, University of Reading.

Assefa, S., McCann, C. and Sothcott, J., 2003. Velocities of compressional and shear waves in limestones: Geophysical Prospecting, **51**, 1-13.

Baechle, G.T., Weger, R.J., Eberli G.P., Massaferro, J.-L., and Sun. Y.-F., 2005, Changes of shear moduli in carbonate rocks: Implications for Gassmann applicability: The Leading Edge, **24**, 507-510.

Batzle, M.L., Han, D.-H., and Hofmann, R., 2006, Fluid mobility and frequency-dependent seismic velocity – Direct measurement: Geophysics, **71**, N1-N9.

Best, A.I., McCann, C. and Sothcott, J., 1994, The relationships between the velocities, attenuations and petrophysical properties of reservoir sedimentary rocks: Geophysical Prospecting, **42**, 151-178.

Biot, M.A., 1956a, Theory of propagation of elastic waves in a fluid saturated porous solid I. Low frequency range: The Journal of the Acoustical Society of America,**28**, 168-178.

Biot, M.A., 1956b, Theory of propagation of elastic waves in a fluid saturated porous solid II. High frequency range: The Journal of the Acoustical Society of America, **28**, 179-191.

Eberli, G.P., Baechle, G.T., Anselmetti, F., and Incze, M., 2003, Factors controlling elastic properties in carbonate sediments and rocks: The Leading Edge, **22**, 654-660.

Gassmann, F., 1951, Über die Elastizität poröser Medien: Viereljahrscrift der Naturforschende Gesellschaft in Zürich, **96**, 1-23.

Jakobsen, M., Hudson, J.A. and Johansen, T.A., 2003a, T-matrix approach to shale acoustic: Geophysical Journal International, **154**, 533-558.

Jakobsen, M., Johansen, T.A., and McCann, C., 2003b, The acoustic signature of fluid flow in a complex porous media: Journal of Applied Geophysics, **54**, 219-246.

Jakobsen, M. and Johansen, T.A., 2005, The effect of drained and undrained loading on visco-elastic waves in rock-like composites: International Journal of Solids and Structures, **42**, 1597-1611.

Johansen, T.A., Drottning, Å., Lecomte, I., and Gjøystdal, H., 2002, An Approach to combined rock physics and seismic modelling of fluid substitutions effects: Geophysical Prospecting, **50**, 119-137.

Mavko, G., Mukerji, T., and Dvorkin, J., 1998, The rock physics handbook: tools for seismic analysis in porous media: Cambridge University Press.

McCann C. and Sothcott J., 1992, Loboratory measurements of the seismic properties of sedimentary rocks, in A. Hurst, P.F. Worthington and C. Griffiths, eds., Geological Applications of wire line logs 2: Special publications of the geological society of London, 285-297.

Rossebø, Ø.H., Brevik, I. Gholam, R.A. and Adam, L., 2005, Modeling of acoustic properties in carbonate rocks: 75th Annual International Meeting, SEG, Expanded Abstracts, 1505-1508.

Tod, S. R., 2001, The effect on seismic waves of interconnected nearly aligned cracks: Geophysical Journal International, **146**, 249-263.

Wang, Z., 2000, The Gassmann equation revisited: Comparing laboratory data with Gassmann's prediction, in Z. Wang, and A. Nur, eds., Seismic and acoustic velocities in reservoir rocks: Recent developments, **3**, SEG, 8-23.

Wang, Z., 1997, Seismic properties of carbonate rocks, in Palaz, I, Marfurt, K.J., eds., Carbonate Seismology: Geophysical Developments, **6**, 29-52.

List of Figures

representing the dried core plug at 0 MPa effective pressure. For the saturated core plug, both these distributions represent fluid-filled cracks. Figure 5b: Sketch of the model used in the 2. approach. The fluid filled cracks (represented as black ellipsoids) are fully connected with respect to each other, but isolated to the dry porosity. Figure 5c: Sample 1 (2. approach). Measured and calculated P-wave velocities for dried plug (square, dashed line) and saturated plug (circle, solid line). Figure 5d: Sample 1 (2. approach). Measured and calculated S-wave velocities for dried plug (circle (90^0), square (0^0) and dashed line) and brine saturated plug (dots (90^0), stars (0^0) and solid line). Figure 5e: Sample 1 (2. approach). Calculated and measured attenuations: a) Brine saturated core plug; P-wave (solid line and squares), S-wave (dotted line and stars). B) Dried core plug; P-wave (dashed line and circles), S-wave (dash-dot line and diamonds)……..30

6. Figure 6a: Sample 1 (3. approach). Crack distribution used in the calculation. Solid line represents the fluid-filled cracks and the dashed line represents the dry cracks in the dried core plug at 0 MPa effective pressure. For the saturated core plug, both these distributions represent fluid-filled cracks. Figure 6b: A sketch of the final model of sample 1. The black ellipsoids represent the fluid-filled porosity for the dried core plug. The fluid-filled porosity and the dry porosity are considered as two systems which are individually connected but isolated relative to each other. Figure 6c: Sample 1. Measured and calculated P-wave velocities for dried plug (square, dashed line) and saturated plug (circle, solid line). The stars are Gassmann calculated P-velocity using the properties measured from the saturated core plug. Figure 6d: Sample 1. Measured and calculated S-wave velocities for dried plug (circle (90^0), square (0^0) and dashed line) and brine saturated plug (dots (90^0), stars (0^0) and solid line). Figure 6e: Sample 1. Measured and calculated attenuations: a) Brine saturated core plug; P-wave

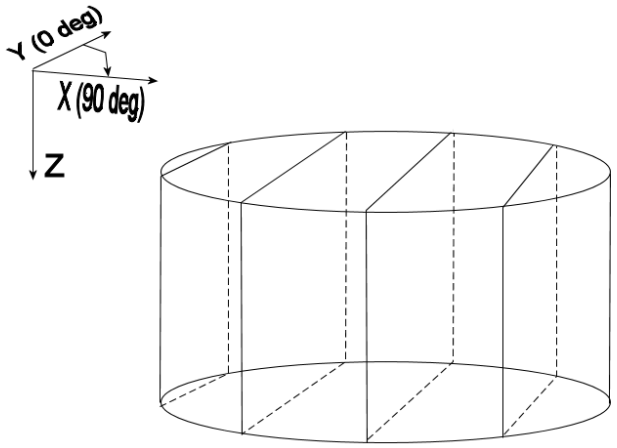

Figure 1: Model of the core plug where y-axis is parallel to the crack-plane and x-axis is perpendicular to the crack-plane.

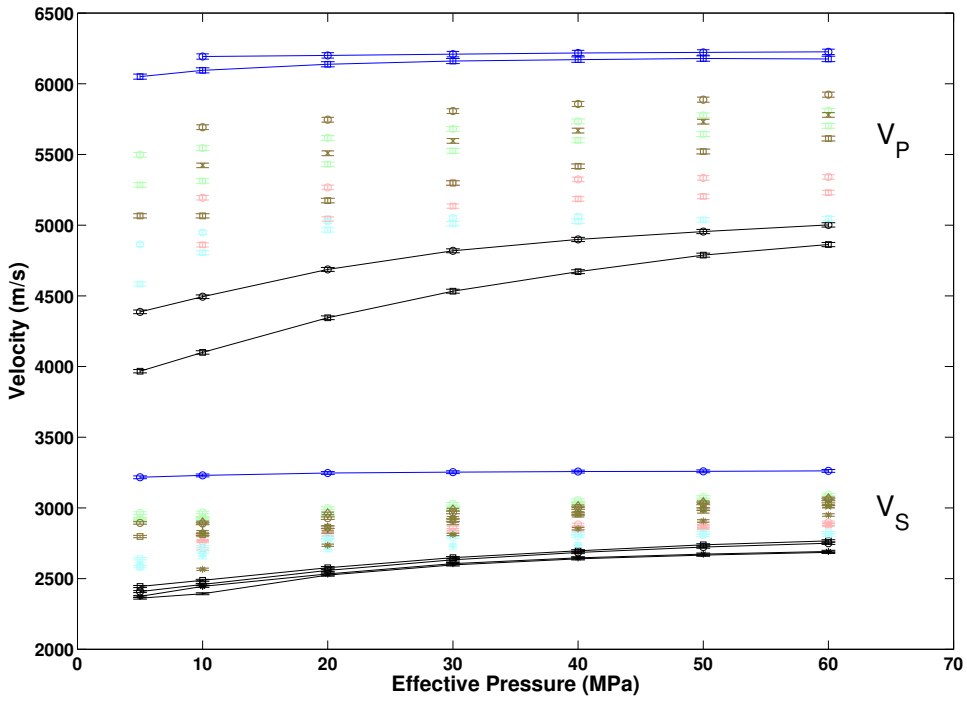

Figure 2: Measured P- and S-wave velocities. Sample 1 (black), sample 2 (red), sample 3 (blue), sample 4 (green), sample 5, (cyan) and sample 6 (gray). The equal coloured lines indicate measurements of same plug, but where the porosity is either dry or saturated with brine. A detailed description of each sample can be found in Figures 4 to 11.

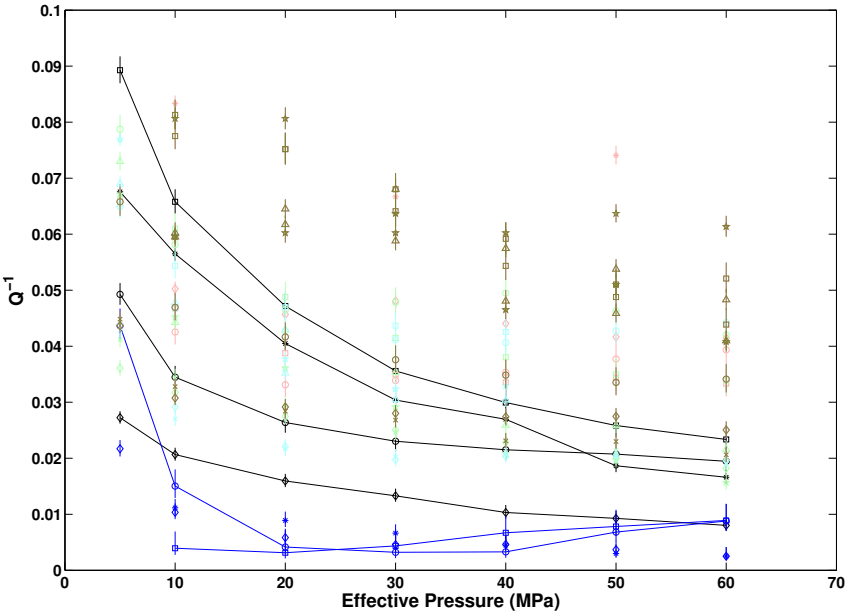

Figure 3. Measured P- and S-wave attenuations. Sample 1 (black), sample 2 (red), sample 3 (blue), sample 4 (green), sample 5, (cyan) and sample 6 (gray). The equal coloured lines indicate measurements of same plug, but where the porosity is either dry or saturated with brine. A detailed description of each sample can be found in Figures 4 to 11.

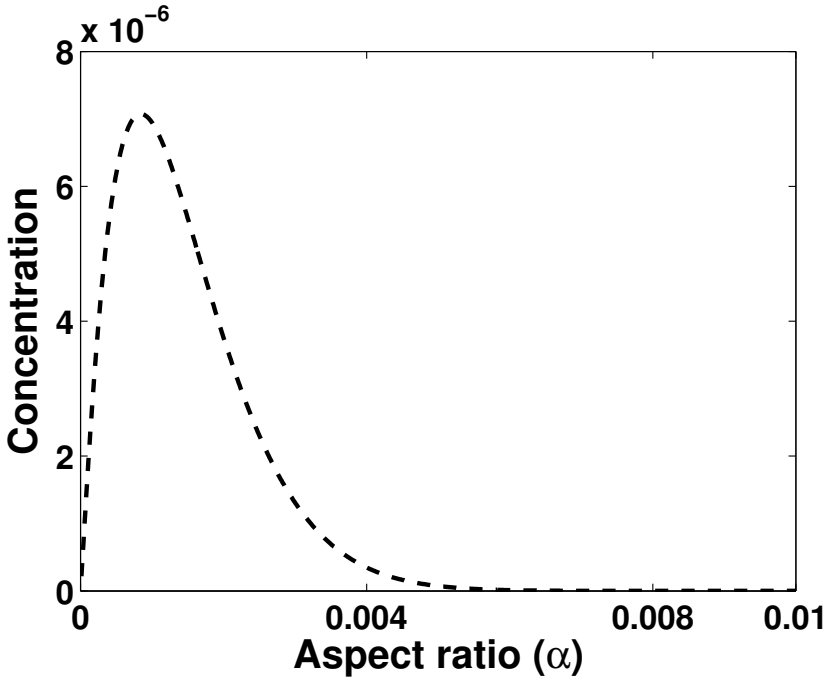

Figure 4a: Sample 1 (1. Approach). Crack distribution at 0 MPa effective pressure used in the calculation where the porosity is fully connected.

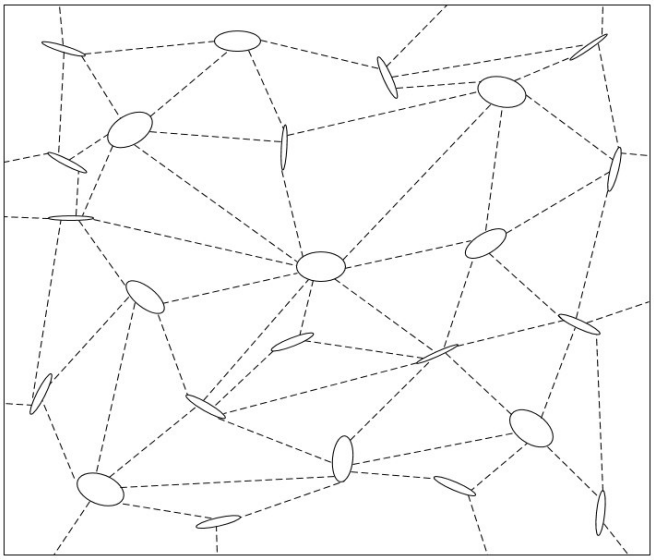

Figure 4b: (1. Approach). Sketch of the fully connected porosity.

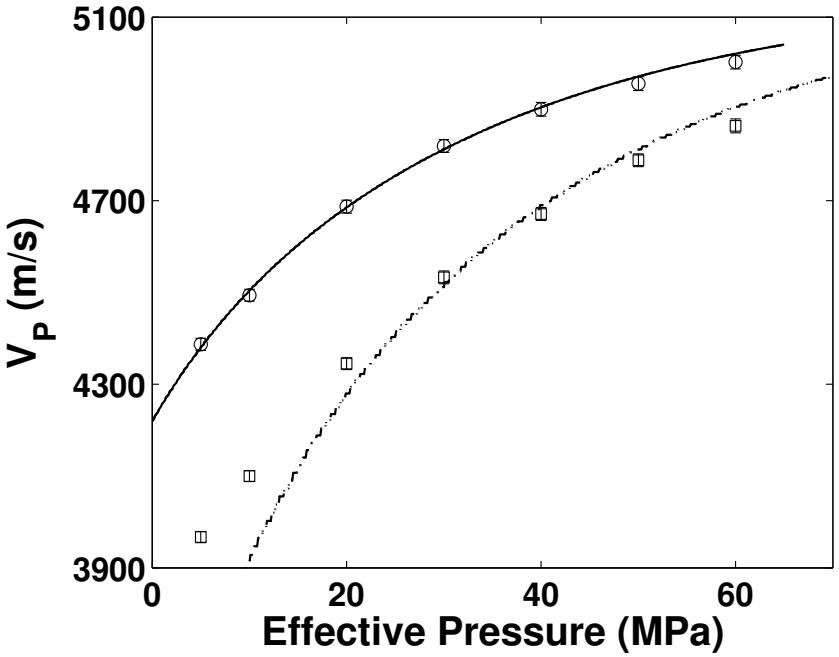

Figure 4c: Sample 1 (1. Approach). Measured and calculated P-wave velocities for dried (square, dashed line) and saturated sample (circle, solid line), respectively.

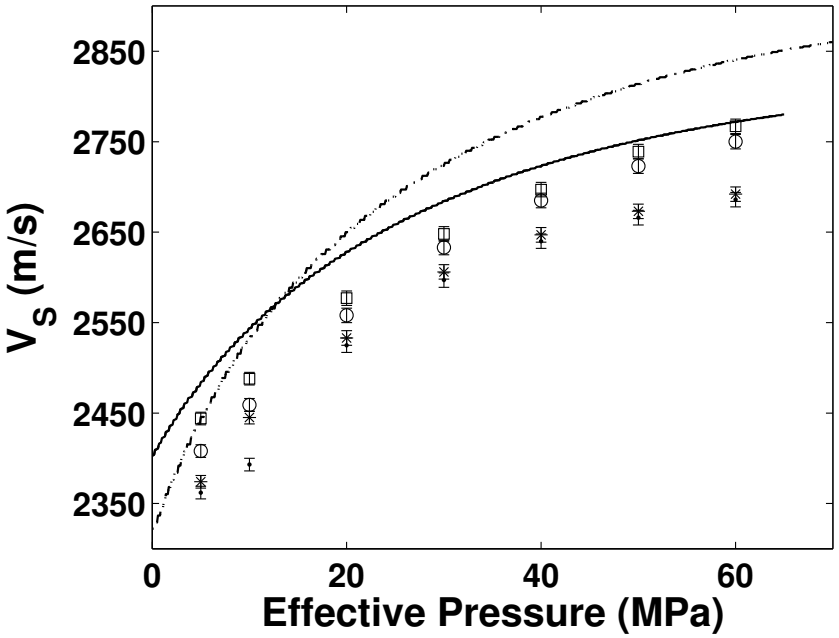

Figure 4d: Sample 1 (1. Approach). Measured and calculated S-wave velocities for dried (circle (90^0), square (0^0) and dashed line) and brine saturated sample (dots (90^0), stars (0^0) and solid line), respectively.

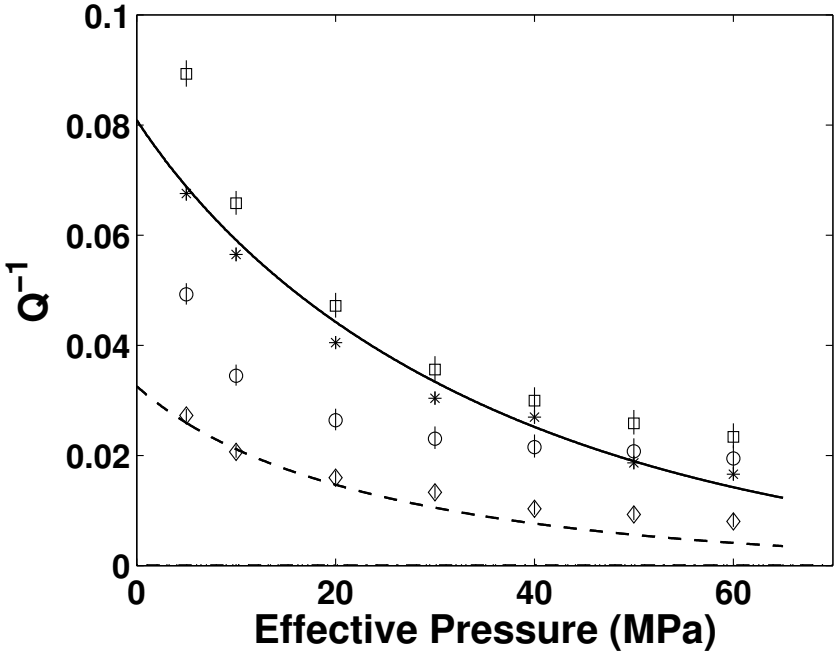

Figure 4e: Sample 1 (1. Approach). Calculated and measured attenuations for: a) Saturated plug; P-wave (solid line and squares), S-wave (dotted line and stars) b) Dried plug; P-wave (dashed line and circles), and the S-wave (dash-dot line and diamonds).

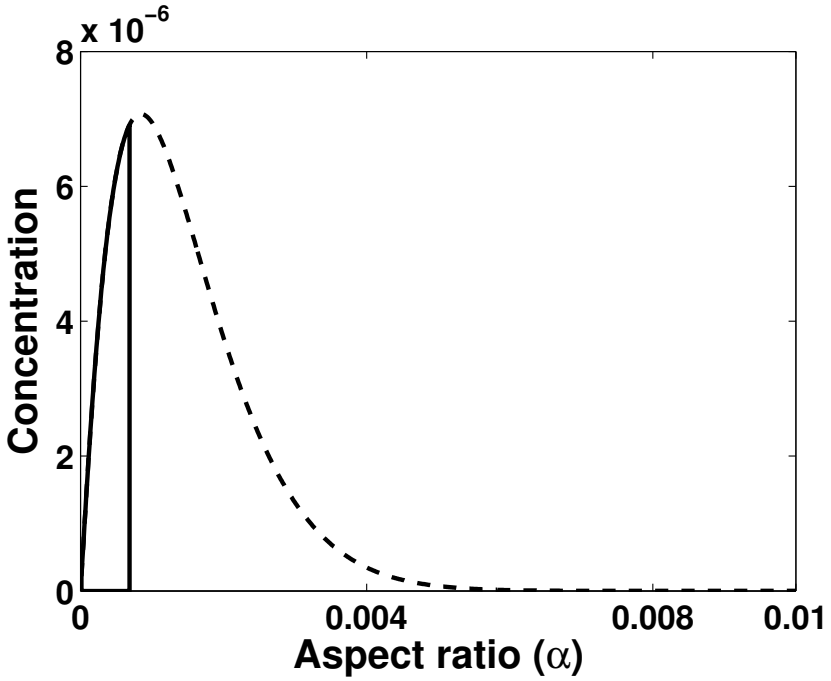

Figure 5a: Sample 1 (2. Approach). Crack distribution used in the calculation of sample 1. Solid line is the fluid-filled cracks and the dashed line is dry cracks in representing the dried core plug at 0 MPa effective pressure. For the saturated core plug, both these distributions represent fluid-filled cracks.

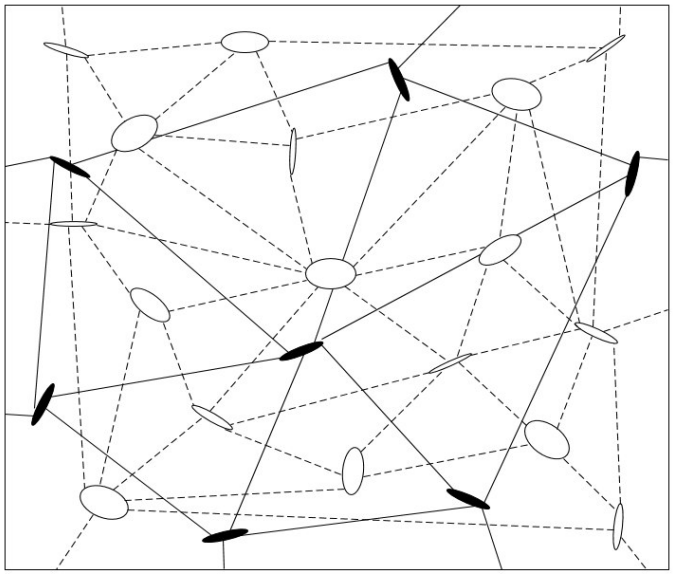

Figure 5b: Sketch of the model used in the 2. approach. The fluid filled cracks (represented as black ellipsoids) are fully connected with respect to each other, but isolated to the dry porosity.

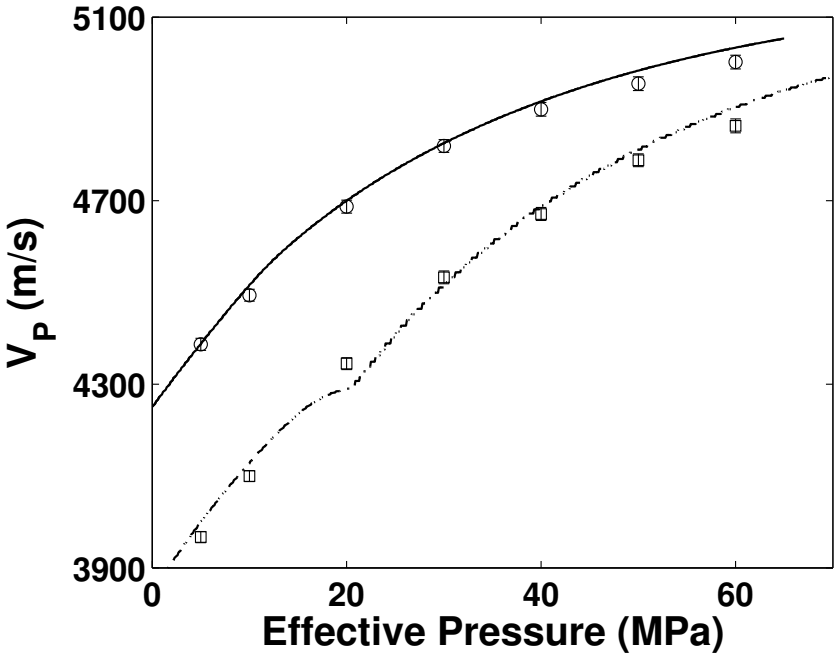

Figure 5c: Sample 1 (2. approach). Measured and calculated P-wave velocities for dried plug (square, dashed line) and saturated plug (circle, solid line).

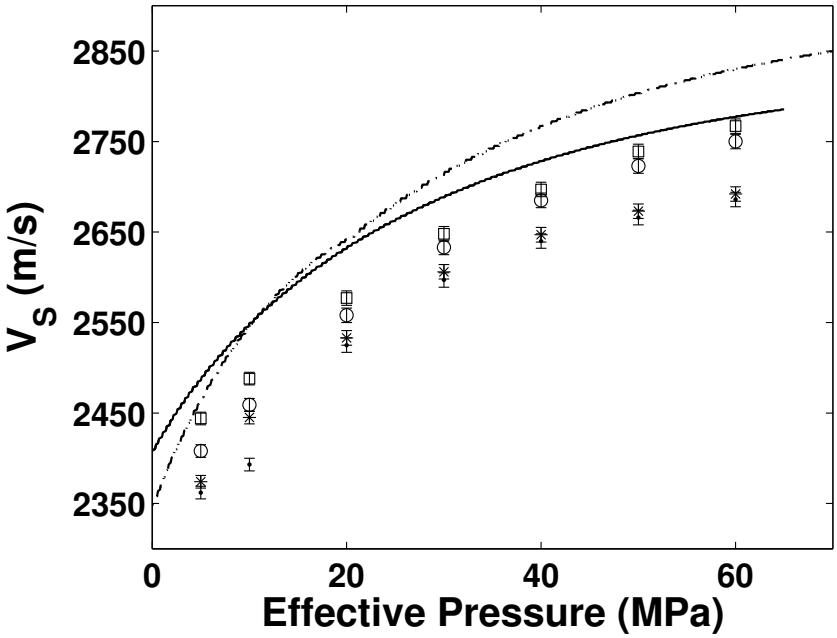

Figure 5d: Sample 1 (2. approach). Measured and calculated S-wave velocities for dried plug (circle (90^0), square (0^0) and dashed line) and brine saturated plug (dots (90^0), stars (0^0) and solid line).

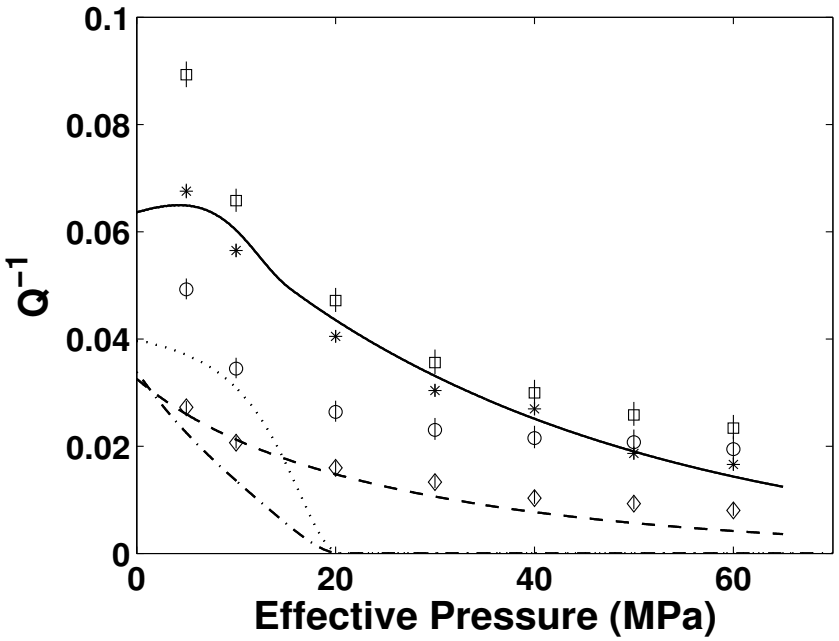

Figure 5e: Sample 1 (2. approach). Calculated and measured attenuations: a) Brine saturated core plug; P-wave (solid line and squares), S-wave (dotted line and stars). B) Dried core plug; P-wave (dashed line and circles), S-wave (dash-dot line and diamonds).

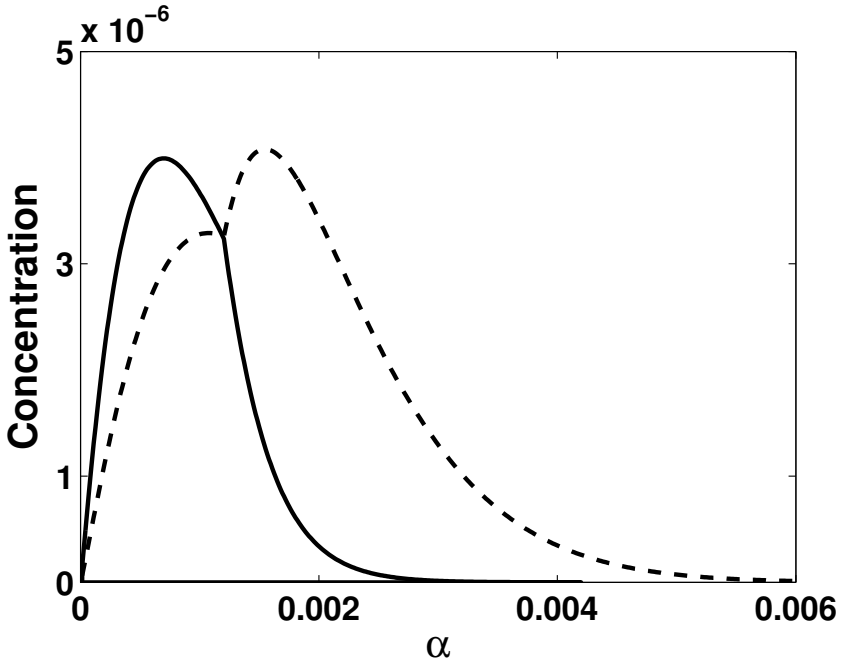

Figure 6a: Sample 1 (3. approach). Crack distribution used in the calculation. Solid line represents the fluid-filled cracks and the dashed line represents the dry cracks in the dried core plug at 0 MPa effective pressure. For the saturated core plug, both these distributions represent fluid-filled cracks.

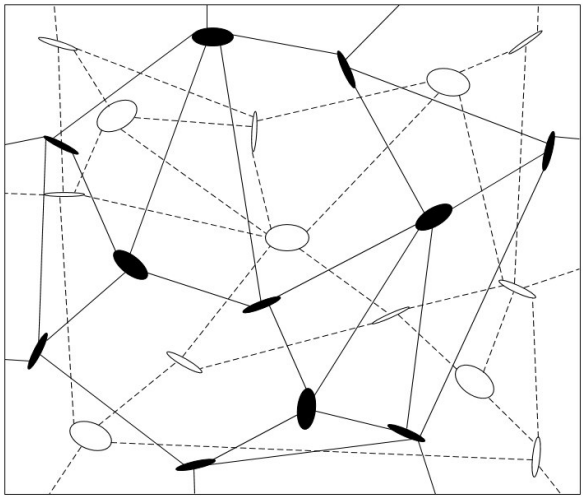

Figure 6b: A sketch of the final model of sample 1. The black ellipsoids represent the fluid-filled porosity for the dried core plug. The fluid-filled porosity and the dry porosity are considered as two systems which are individually connected but isolated relative to each other.

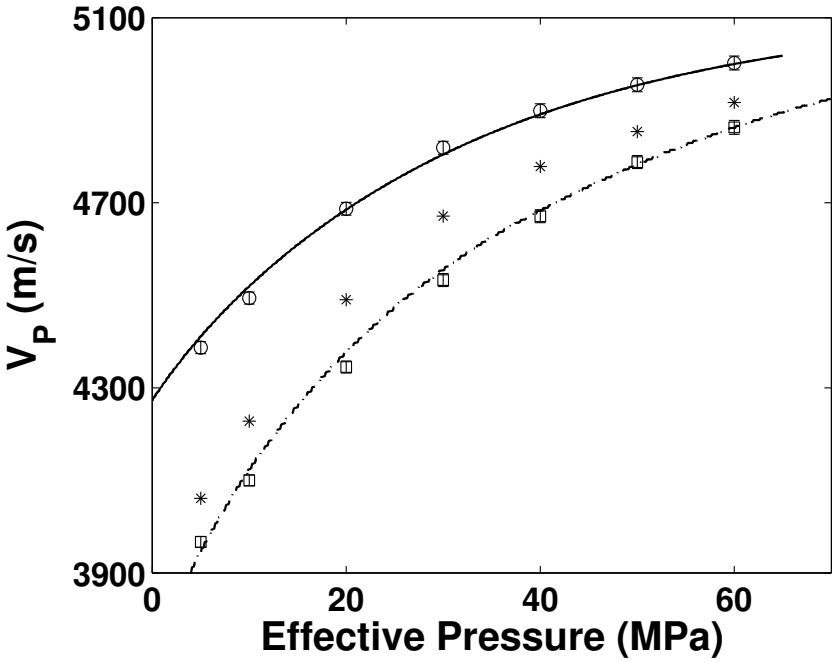

Figure 6c: Sample 1. Measured and calculated P-wave velocities for dried plug (square, dashed line) and saturated plug (circle, solid line). The stars are Gassmann calculated P-velocity using the properties measured from the saturated core plug.

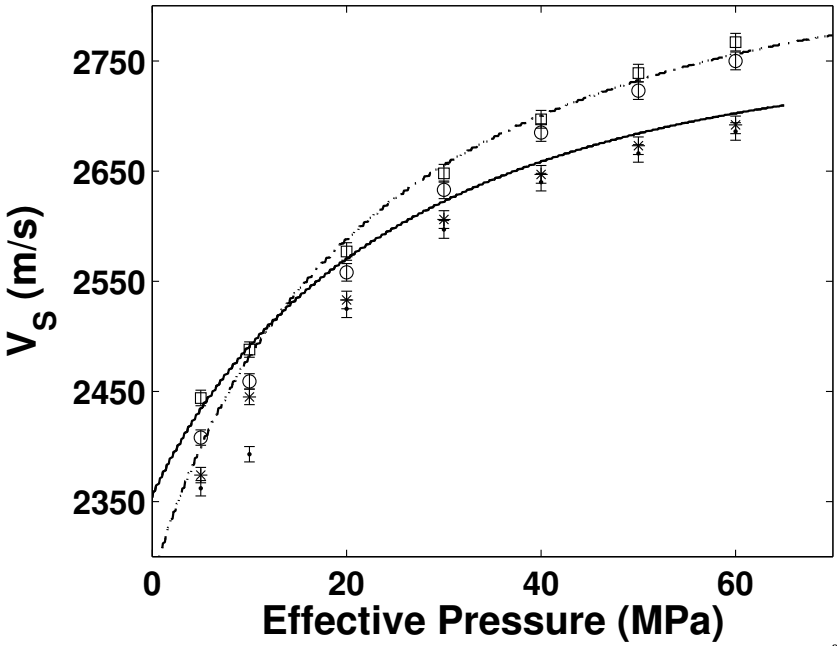

Figure 6d: Sample 1. Measured and calculated S-wave velocities for dried plug (circle (90^0), square (0^0) and dashed line) and brine saturated plug (dots (90^0), stars (0^0) and solid line).

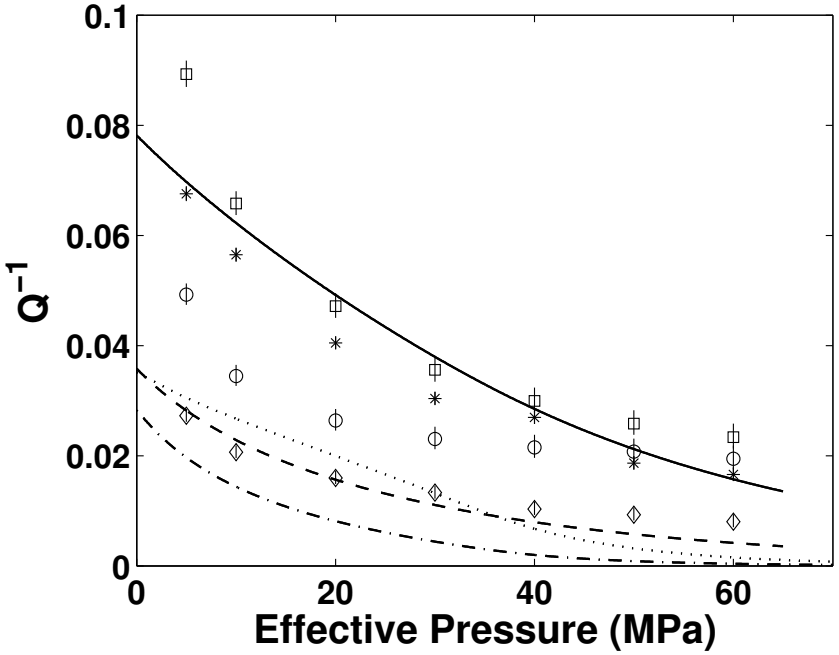

Figure 6e: Sample 1. Measured and calculated attenuations: a) Brine saturated core plug; P-wave (squares and solid line and), S-wave (stars and dotted line). b) Dried core plug; P-wave (circles and dashed line), S-wave (diamonds and dash-dot line).

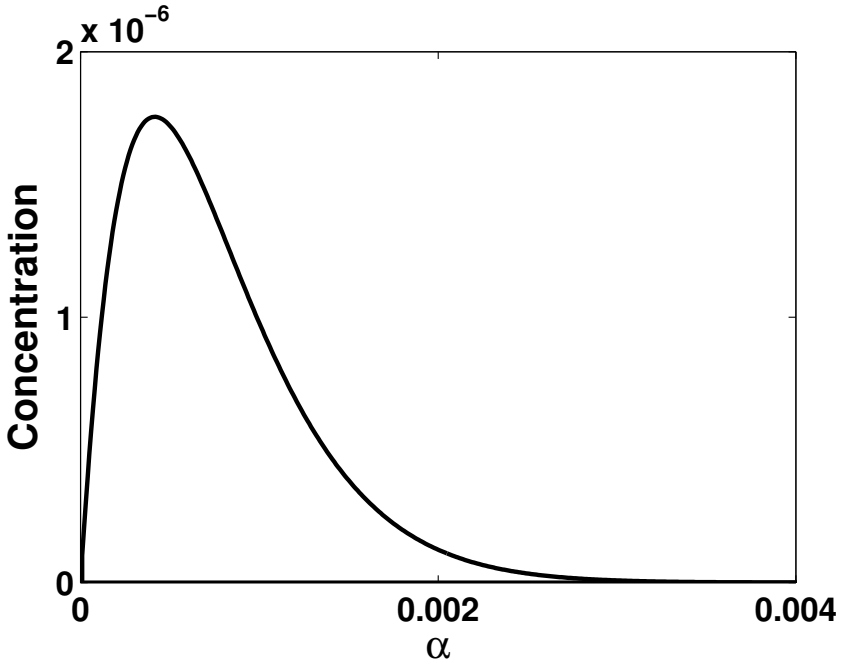

Figure 7a: The crack distribution used in the calculation of sample 2.

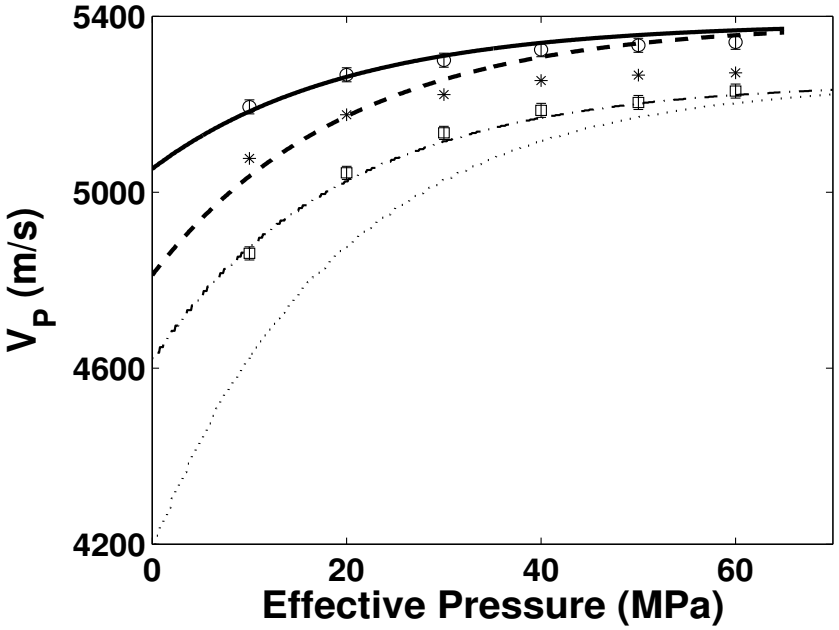

Figure 7b: Sample 2. Measured and calculated P-wave velocities for dried plug (square, dashed and dotted line (parallel to vertical cracks) and dotted line (perpendicular to vertical cracks)) and saturated plug (circle, solid line (parallel to vertical oriented) and dashed line (perpenticular to the vertical cracks)). The stars are the Gassmann calculated P-velocity using the properties measured for the saturated plug.

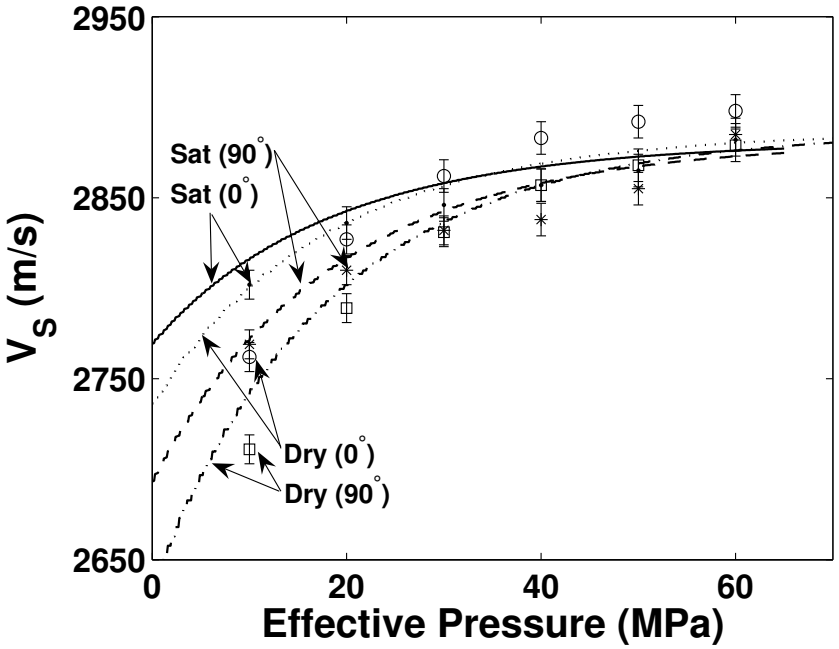

Figure 7c: Sample 2. Measured and calculated S velocities for dried plug (circle – dotted line for 0^0, square – dashed-dotted line for 90^0), and saturated plug (dot – solid line for 0^0, star – dashed line for 90^0).

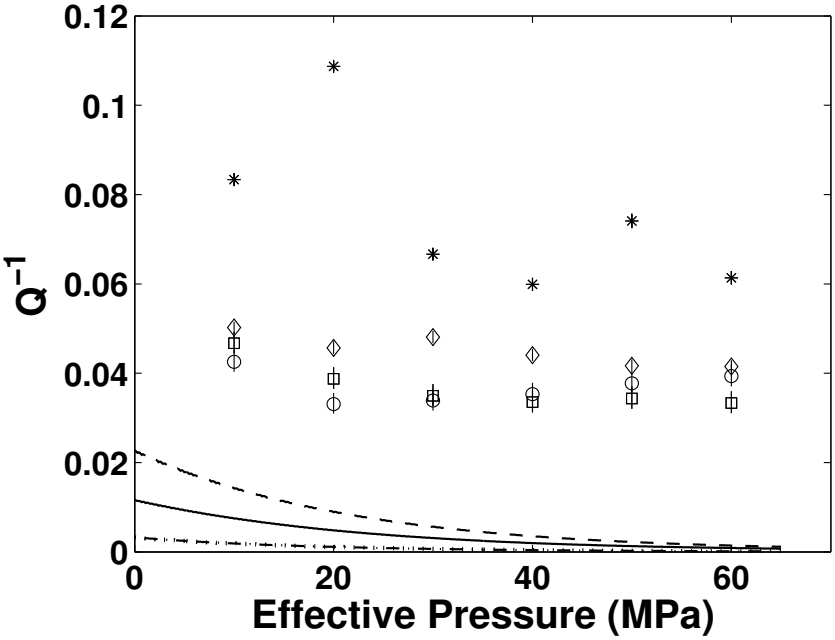

Figure 7d: Sample 2. Measured and modelled attenuations of P waves; dried plug (squares - dashed line parallel to vertical cracks, solid line perpendicular to vertical cracks), saturated plug (stars), and S-waves; dried plug (diamonds - dashed-dotted line for both 0^0 and 90^0), saturated plug (circles).

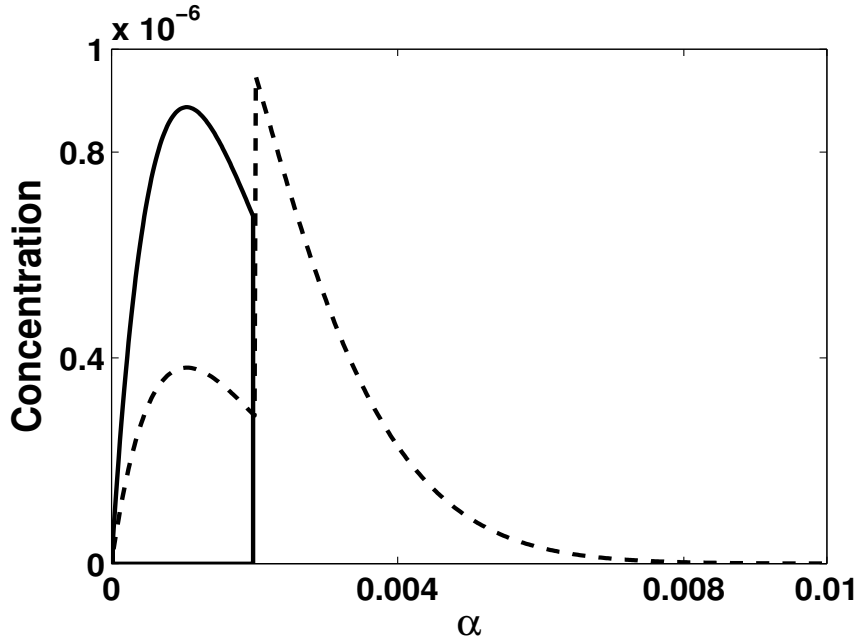

Figure 8a: Sample 3. The crack distribution used in the calculation. Solid line is the saturated crack distribution and dashed line is the dry crack distribution.

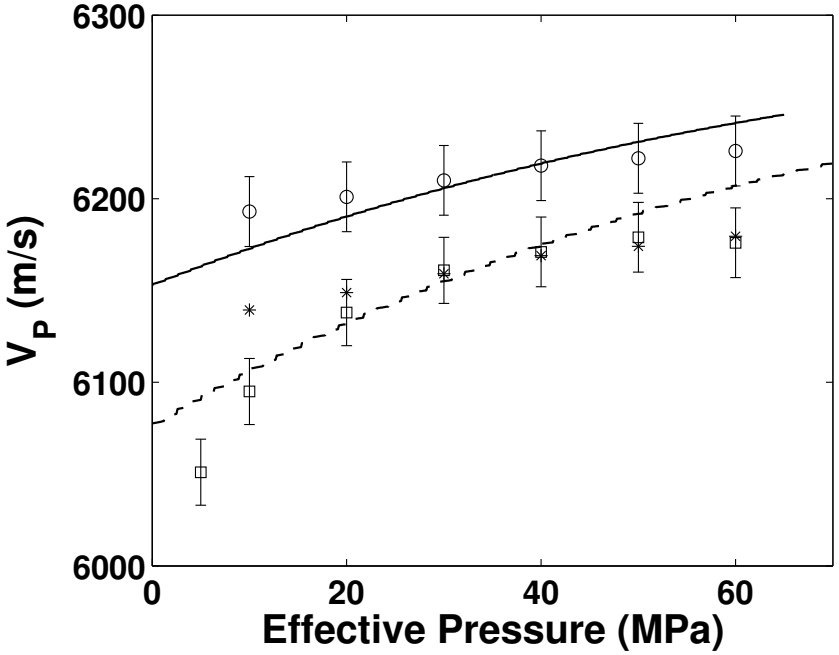

Figure 8b: Sample 3. Measured and calculated P-wave velocities for the dried plug (squares and dashed line) and the saturated plug (circles and solid line). The stars are the Gassmann calculated P-velocity using the properties measured for the saturated core plug.

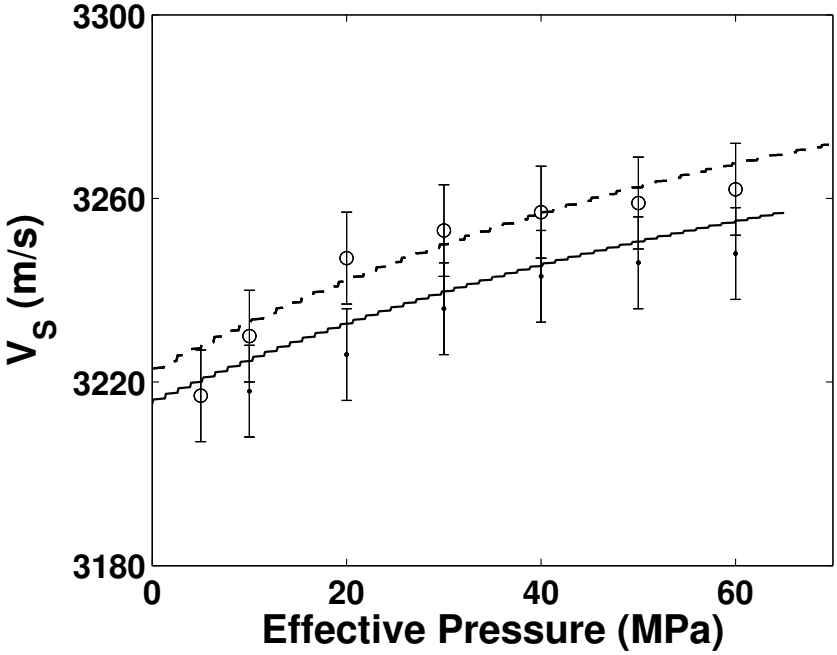

Figure 8c: Sample 3. Measured and calculated S-wave velocities for the dried plug (circles and dashed line) and the saturated plug (dots and solid line).

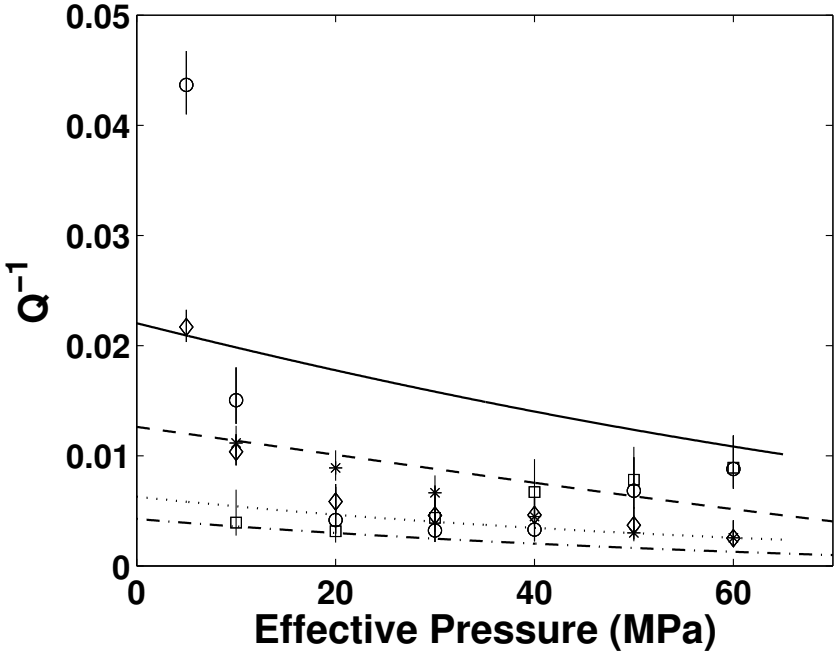

Figure 8d: Sample 3. Measured and modelled attenuations of P waves; dried plug (squares - dashed line parallel to vertical cracks, solid line perpendicular to vertical cracks), saturated plug (stars), and S-waves; dried plug (diamonds - dashed-dotted line for both 0^0 and 90^0), saturated plug (circles).

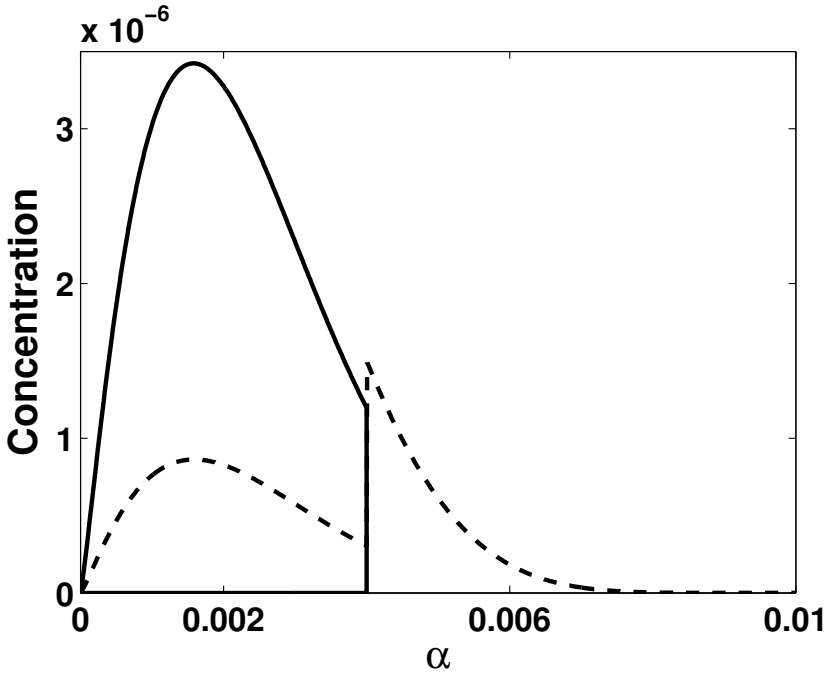

Figure 9a: Sample 4. The crack distribution used in the calculation. Solid line is the saturated crack distribution and dashed line is the dry crack distribution.

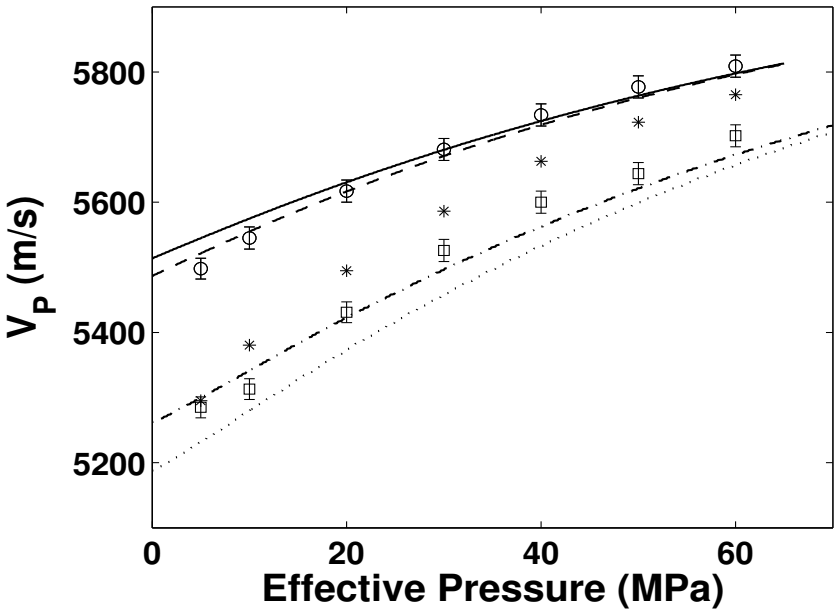

Figure 9b: Sample 4. Measured and calculated P-wave velocities for dried plug (square, dashed and dotted line (parallel to vertical cracks) and dotted line (perpendicular to vertical cracks)) and saturated plug (circle, solid line (parallel to vertical oriented) and dashed line (perpenticular to the vertical cracks)). The stars are the Gassmann calculated P-velocity using the properties measured for the saturated plug.

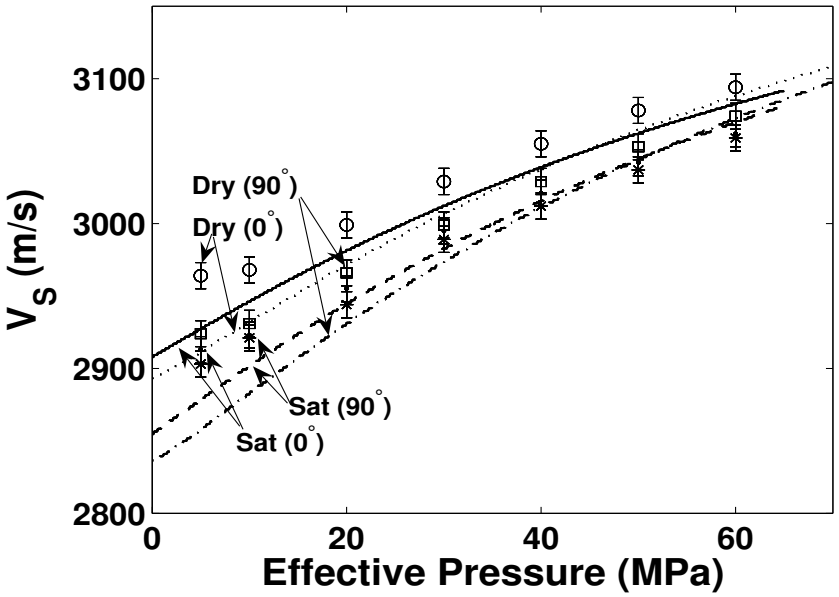

Figure 9c: Sample 4. Measured and calculated S velocities for dried plug (circle – dotted line for 0^0, square – dashed-dotted line for 90^0), and saturated plug (dot – solid line for 0^0, star – dashed line for 90^0).

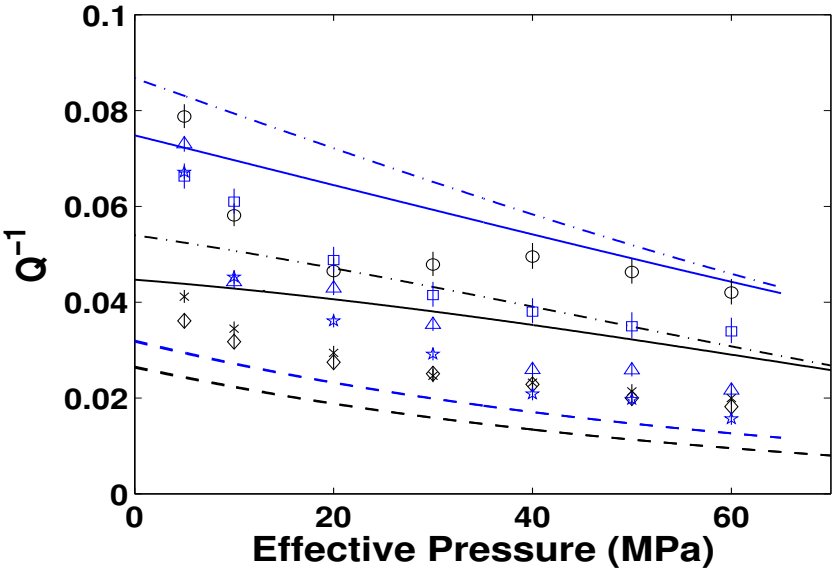

Figure 9d: Sample 4. Measured and modelled attenuations of P waves; dried plug (circles – dashed-dotted line parallel to vertical cracks, solid line perpendicular to vertical cracks), saturated plug (stars – blue dashed-dotted line parallel to vertical cracks, blue solid line perpendicular to vertical cracks), and S waves; dried plug (diamonds - dashed line for 0^0, crosses and for 90^0), saturated plug (blue stars – blue dashed line for 0^0, blue triangles – blue dashed line for 90^0).

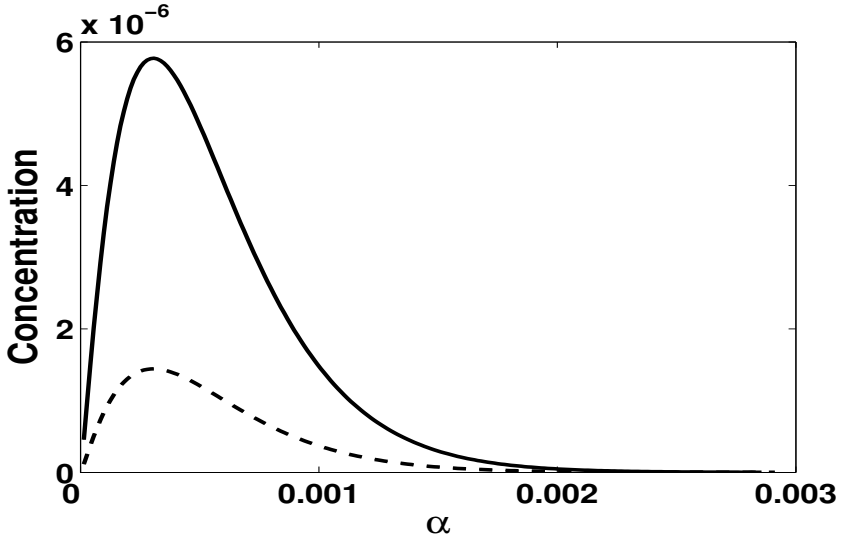

Figure 10a: Sample 5. The crack distribution used in the calculation. Solid line is the saturated crack distribution and dashed line is the dry crack distribution.

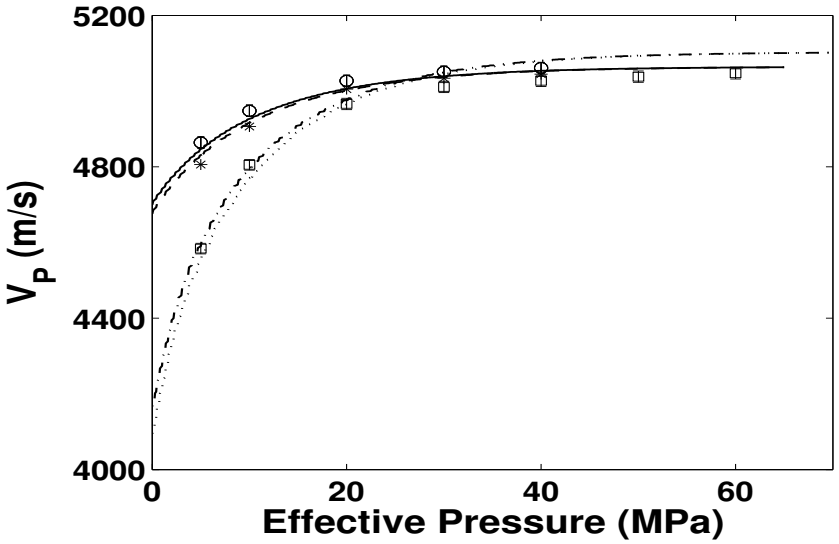

Figure 10b: Sample 5. Measured and calculated P-wave velocities for dried plug (square, dashed and dotted line (parallel to vertical cracks) and dotted line (perpendicular to vertical cracks)) and saturated plug (circle, solid line (parallel to vertical oriented) and dashed line (perpenticular to the vertical cracks)). The stars are the Gassmann calculated P-velocity using the properties measured for the saturated plug.

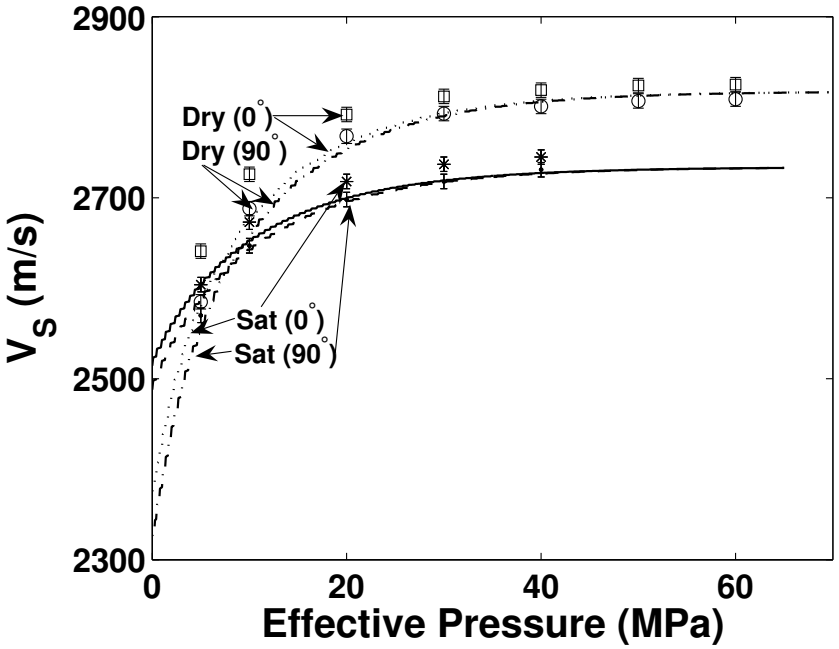

Figure 10c: Sample 5. Measured and calculated S velocities for dried plug (circle – dotted line for 0^0, square – dashed-dotted line for 90^0), and saturated plug (dot – solid line for 0^0, star – dashed line for 90^0).

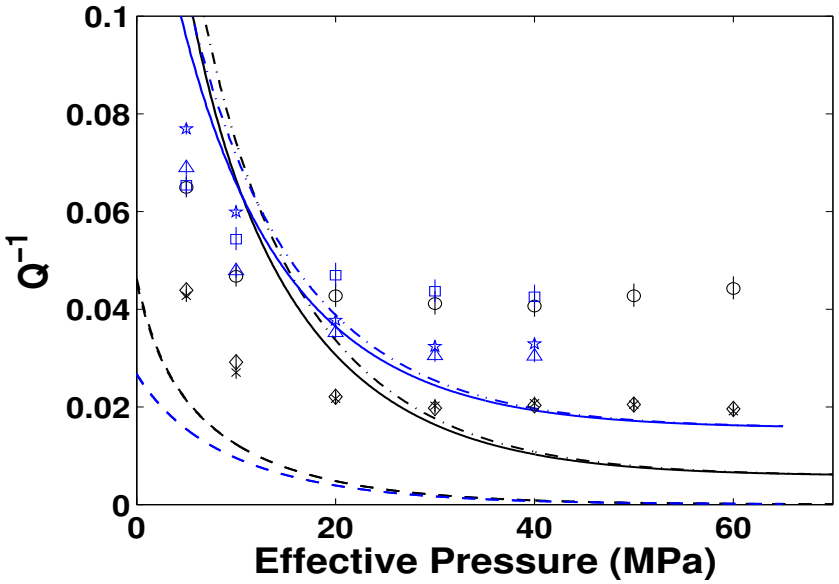

Figure 10d: Sample 5. Measured and modelled attenuations of P waves; dried plug (circles – dashed-dotted line parallel to vertical cracks, solid line perpendicular to vertical cracks), saturated plug (stars – blue dashed-dotted line parallel to vertical cracks, blue solid line perpendicular to vertical cracks), and S waves; dried plug (diamonds - dashed line for 0^0, crosses and for 90^0), saturated plug (blue stars – blue dashed line for 0^0, blue triangles – blue dashed line for 90^0).

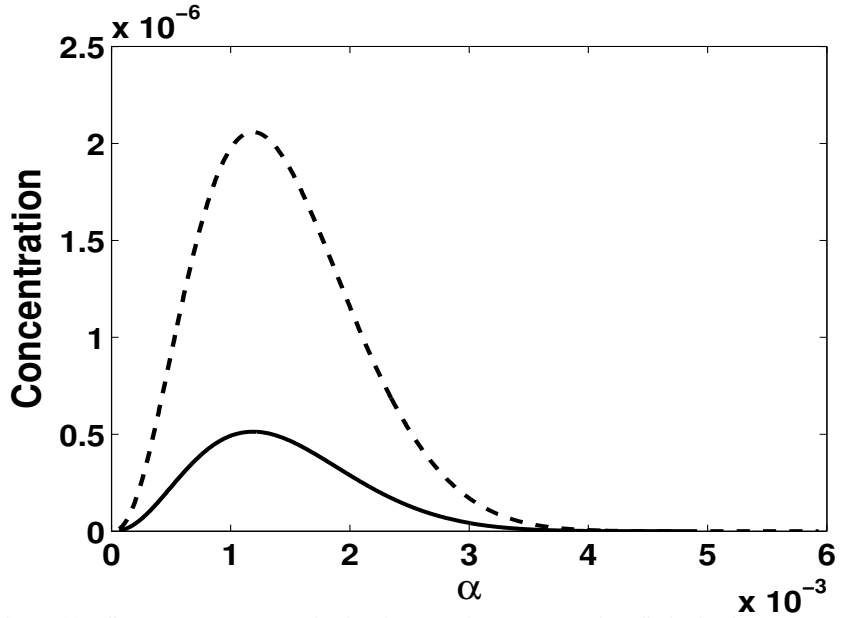

Figure 11a: Sample 6. The crack distribution used in the calculation. Solid line is the saturated crack distribution and dashed line is the dry crack distribution.

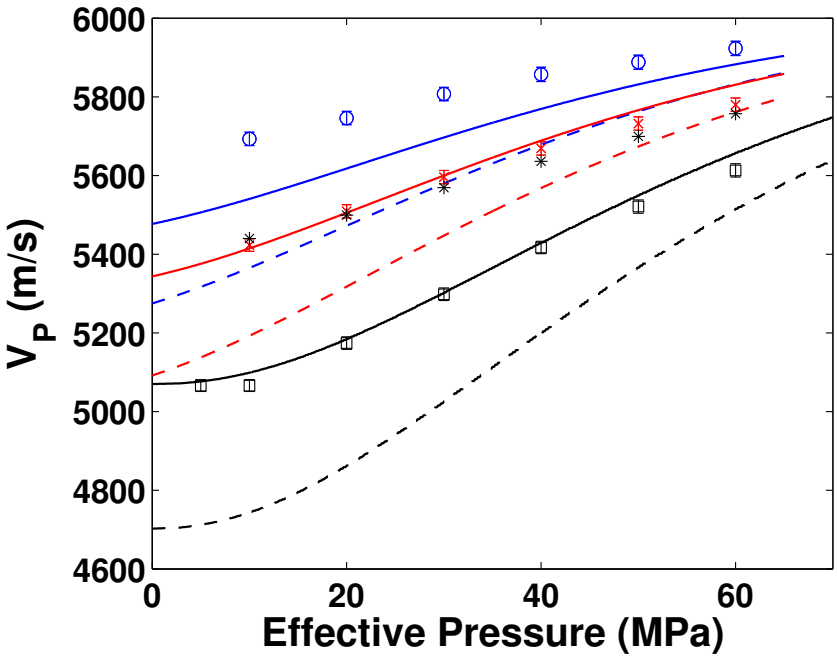

Figure 11b: Sample 6. Measured and calculated P-wave velocities for dried plug (black squares, black solid and dashed line); brine saturated plug (blue circles, blue solid and dashed line); kerosene saturated plug (red crosses, red solid and dashed line). The solid line represents P-velocity parallel to the vertical cracks and the dashed line is the P-velocity normal to the vertical cracks. The stars are Gassmann calculated P-velocity from measured properties of dried plug with brine as fluid.

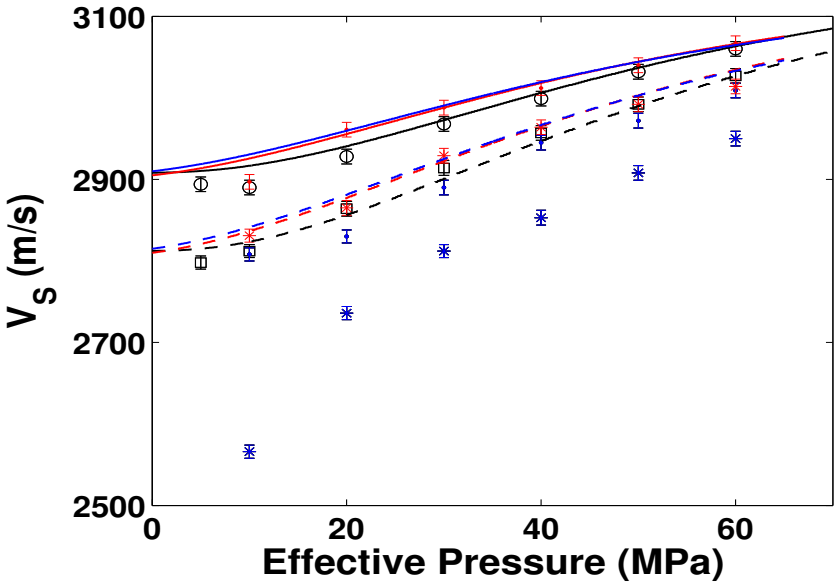

Figure 11c: Sample 6. Measured and calculated S-wave velocities for dried sample (squares – solid line for 0^0 , circles – dashed line for 90^0), brine saturated sample (blue stars – blue solid line for 0^0, blue dots – blue dashed line for 90^0) and kerosene saturated sample (red stars - red solid line for 0^0, red dots – red dashed line for 90^0).

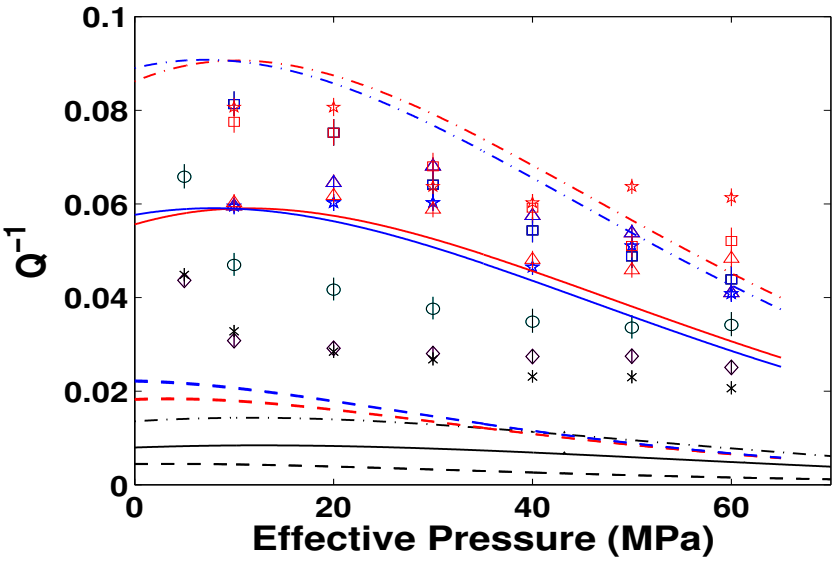

Figure 11d: Sample 6. Measured and modelled attenuations of P waves; dried plug (square – dashed-dotted line parallel to vertical cracks, solid line perpendicular to vertical cracks), brine saturated plug (blue square – blue dashed-dotted line parallel to vertical cracks, blue solid line perpendicular to vertical cracks), kerosene saturated plug (red square – red dashed-dotted line parallel to vertical cracks, red solid line perpendicular to vertical cracks), and S waves; dried plug (star - dashed line for 0^0, crosses and for dashed line for 90^0), saturated plug (blue stars – blue dashed line for 0^0, blue triangles – blue dashed line for 90^0) and kerosene saturated plug (red stars – red dashed line for 0^0, red triangles – red dashed line for 90^0).

Sample	Porosity (%)	Permeability (mD)
1	11.77	2.463
2	9.07	11.761
3	2.18	0
4	3.76	0.075
5	13.97	74.442
6	3.4	0.013

Table 1: Measured properties of the calcite samples.

Sample	V_P (m/s)	V_S (m/s)	ρ (kg/m^3)	φ_{tot} (%)	φ_{dry} (%)	φ_{sat} (%)	$Dev_{Gassmann}$ (%)
1	6260	3140	2710	13.35	11.75	1.6	2.4
2	6260	3180	2710	9.07	9.07	0	4.4
3	6530	3360	2710	2.76	2.75	0.01	0.7
4	6260	3330	2710	4.91	3.76	1.15	0.2
5	6260	3150	2710	16.02	13.97	2.05	4.9
6	6360	3240	2710	3.98	3.38	0.6	4.5

Table 2: Effective mineral properties, total, dry and saturated porosities used for calculating the P- and S-wave velocities and the corresponding attenuations. Last column shows the deviation of our modelling to the Gassmann predicted P-wave velocity for each sample.

Sample	τ	ε_0	$\overline{\alpha}$	δ	u	p_0	a	b	c
1	$0.11 \cdot 10^{-8}$	0.3	0.0015	0.91	0.02	0.7	0.004	0.03	0.5
2	$0.1 \cdot 10^{-9}$	0.11	0.0004	0.95	0.01	-	-	-	-
3	$0.5 \cdot 10^{-8}$	0.04	0.001	0.95	0.02	0.7	0.00001	0.03	0.5
4	$1.6 \cdot 10^{-8}$	0.23	0.0014	0.8	0.01	0.8	0.00001	-	-
5	$0.2 \cdot 10^{-8}$	0.3	0.0003	0.9	0.014	-	-	-	-
6	$0.3 \cdot 10^{-8}$	0.15	0.0011	0.55	0.006	0.2	0.00001	-	-

Table 3: Pore structure models used.

Fluid	V_P (m/s)	Density (kg/m^3)	Viscosity (cP)
Brine	1557	1031	1
Kerosene	1324	804	2.12
Air	330	1.23	≈0

Table 4: Fluid properties used.

Paper 3

EFFECTS OF PORE FLUID PRESSURE ON THE SEISMIC RESPONSE OF A FRACTURED CARBONATE RESERVOIR

Journal Studia Geophysica et Geodaetica 51(1), Agersborg, R.; Jakobsen, M.; Ruud, B.; Johansen, T., Effects of pore fluid pressure on the seismic response of a fractured carbonate reservoir, pp. 89-118(30).
 http://dx.doi.org/10.1007/s11200-007-0005-8

ABSTRACT
An effective medium model for the stress-dependent seismic properties of fractured reservoirs is developed here on the basis of a combination of a general theory of viscoelastic waves in rock-like composites with recently published formulae for deformation of communicating and interacting cavities (interconnected pores/cracks and fractures at finite concentration) under drained loading. The inclusion-based model operates with spheroidal cavities at two different length scales; namely, the microscopic scale of the pores and (grain-boundary) cracks, and the mesoscopic scale of the fractures (controlling the flow of fluid). The different cavity types can in principle have any orientation and aspect ratio, but the microscopic pores/cracks and mesoscopic fractures were here assumed to be randomly and vertically oriented, respectively. By using three different aspect ratios for the relatively round pores (representing the stiff part of the pore space) and a distribution of aspect ratios for the relatively flat cracks (representing the compliant part of the pore space), we obtained a good fit between theoretical predictions and ultrasonic laboratory measurements on an unfractured rock sample under dry conditions. By using a single aspect ratio for the mesoscopic fractures, we arrived at a higher-order microstructural model of fractured porous media which represents a generalization of the first-order model developed by Chapman et al. (2002,2003). The effect of cavity size was here modelled under the assumption that the characteristic time for wave-induced (squirt) flow at the scale of a particular cavity (pore/crack vs. fracture) is proportional with the relevant scale-size. In the modelling, we investigate the effect of a decreasing pore pressure with constant confining pressure (fixed depth), and hence, increasing effective pressure. The analysis shows that the attenuation-peak due to the mesoscopic fractures in the reservoir will move downward in frequency as the effective pressure increases. In the range of seismic frequencies, our modelling indicates that the P-wave velocities may change by more than 20% perpendicular to the fractures and close to 10% parallel to the fractures. In comparison, the vertical S-wave velocities change by only about 5% for both polarization directions (perpendicular and parallel to the fractures) when the effective pressure increases from 0 to 15 MPa. This change is mainly due to the overall change in porosity with pressure. The weak pressure dependence is a consequence of the fact that the S waves will only sense if the fractures are open or not, and since all the fractures have the same aspect ratio, they will close at the same effective pressure (which is outside the analysed interval). Approximate reflection coefficients were computed for a model consisting of the fractured reservoir embedded as a layer in an isotropic shale and analysed with respect to variations in Amplitude Versus Offset and aZimuth (AVOZ) properties at seismic frequencies for increasing effective pressure. For the P-P reflections at the top of the reservoir, it is found that there is a significant dependence on effective pressure, but that the variations with azimuth and offset are small. The lack of azimuthal dependence may be explained from the approximate reflection coefficient formula as a result of cancellation of terms related to the S-wave velocity and the Thomson's anisotropy parameter d. For the P-S reflection, the azimuthal dependence is larger, but the pressure dependence is weaker (due to a single aspect ratio for the fractures). Finally, using the effective stiffness tensor for the fractured reservoir model with a visco-elastic finite-difference code, synthetic seismograms and hodograms were computed. From the seismograms, attenuation changes in the P wave reflected at the bottom of the reservoir can be observed as the effective pressure increases. S waves are not much affected by the fractures with respect to attenuation, but azimuthal dependence is stronger than for P waves, and S-wave splitting in the bottom reservoir P-S reflection is clearly seen both in the seismograms and hodograms. From the hodograms, some variation in the P-S reflection with effective pressure can also be observed.

Keywords: fractures, cracks, anisotropy, fluid pressure, AVOZ, time-lapse

Paper 4

Modelling reflection signatures of pore fluids and dual porosity in carbonate reservoirs

Remy Agersborg[1,2], Tor Arne Johansen[1] and Bent Ole Ruud[2]

[1] *Department of Earth Science and* [2] *Centre for Integrated Petroleum Research, University of Bergen Allégt. 41, 5007 Bergen, Norway.*

Abstract

The motivation for this synthetic Amplitude Versus Angle (AVA) study of an isotropic carbonate reservoir consisting of a dual porosity on two scales is to identify possible seismic signatures of carbonate rocks containing various fluids and pore connection models. The reservoir is modelled for four scenarios on the basis of a general theory for visco-elastic waves, where the inclusion-based model operates with spheroidal cavities on two scales. While the total porosity of the reservoir is considered constant, the pores and cracks at the different scales are designed to be either connected or isolated. The pore systems are saturated with either gas, oil or water. Reflection coefficients are computed for a 2-layer model consisting of a cap rock of shale above the reservoir in order to analyze the effects of various pore to pore connection and pore fluid models in the double porosity systems.

The modelling shows how the AVA parameters change both due to varying pore to pore connection and various pore fluid saturation scenarios. If we assume estimated AVA parameters with some uncertainties, the study indicates that it should be possible to obtain measurable changes in the reflectivity due to changes of the pore connectivity also when the introduced fluid has almost equal acoustic properties as the displaced one. Such modelling studies should be of particular relevance for studying diagenetic effects on seismic signatures, as for instance, water and oil may have similar acoustic properties, but different impact on the pore system over time.

Keywords: Dual porosity, carbonate reservoir, AVA, fluid substitution, pore structure.

Introduction

The aim of seismic reservoir monitoring and time lapse studies is to follow how the fluids displace within the reservoir unit. It is essential to have the information about the pore geometry and how the pores are connected with respect to fluid flow as accurate as possible in order to differentiate between effects due to alterations in fluid saturation and pressure.

The variations in the seismic properties of carbonate rocks are mainly caused by their complex pore structure (Eberli et al., 2003) where pores and cracks can co-exist on many scales, from microscopic pores/cracks to huge macroscopic fractures (Anselmetti et al., 1998; Wang, 1997). In the context of fluid substitution, where the reservoir is water flooded, the pore geometry and wettability of the rock can cause the water first to flood e.g. the cracks and smaller pores or this may cause the oil to be trapped in the larger pores which again may leave a considerable amount of residual oil in the reservoirs (Chatzis et al., 1983). A study of the Ekofisk field (Sylte et al., 1999) showed that injection of water in the calcite-reservoir caused compaction and porosity loss. They concluded that the sensitivity of the chalk to injected water most probably resulted from an intimate chemical interaction between the injected water and the calcite.

For predicting the P-wave velocity and the seismic effects of fluid substitution, it is common to use Gassmann's equation (Gassmann, 1951). However, for carbonate rocks this relation is not always applicable (Adam et al., 2006; Anselmetti and Eberli, 1999; Assefa et al., 2003; Baechle et al., 2005; Rossebø et al., 2005; Wang, 1997; 2000) and this can to a large extent be caused by the complex pore structure and chemical interaction between the fluid and the carbonate minerals. Modelled velocity and attenuation effects caused by a porosity system on different scales have been discussed by Agersborg et al. (2007a). Here, the seismic properties were modelled using a visco-elastic rock physics theory, referred to as the T-matrix formulation (Jakobsen et al., 2003a,b). This method was

also applied in Agersborg et al. (2007b) for modelling ultrasonic velocity and attenuation data for calcite samples. Various characteristic pore types for carbonate rocks described by Wang (1997) and Choquette and Pray (1970) are referred to as grain-boundary cracks (intercrystaline and interparticle porosity), porous inclusions (intraparticle porosity) and rounded pores (vugs and fenestral porosity). The influence of complex pore structures on seismic velocities is often modelled by using inclusion based theories. Then cavities are modelled as spheroids, where cracks have aspect ratios (α: ratio between minor and major axis) less than 0.001, and compliant pores to spherical pores have aspect ratio from 0.001 to 1.

In this study, we discuss how various pore fluid distributions in a dual porosity system of different scales will influence the seismic signature, and in particular, on Amplitude Versus Angle (AVA) attributes. Similar studies have been done for various microscopic and macroscopic fluid distributions (Johansen et al., 2002), however, in their study the pores were regarded as isolated to fluid flow. For AVA characterization we apply both exact and approximate formulas for the reflection coefficients of PP and PS waves.

Elastic properties of the dual porosity reservoir

Consider a reservoir modelled with the porosity distributed on mesoscopic (meso) and microscopic (micro) scale. The pore systems may be individually connected or unconnected, but they are unconnected with respect to each other. Additionally, each pore system contains cracks. We consider four scenarios revealing various connectivity models: **Model 1**: Connected micro pores and connected meso pores; **Model 2**: Unconnected micro pores and unconnected meso pores; **Model 3**: Unconnected micro pores and connected meso pores; and finally, **Model 4**: Connected micro pores and unconnected meso pores. The four models are conceptually defined in Figure 1. The pores and the cracks on each scale

are saturated with either gas (methane), oil or water with the properties given in Table 1. The aspect ratios of the pore model are defined in Table 2. The permeability was set to 50 mD and the mineral matrix for each scale is calcite with properties as listed in Table 1.

The effective stiffness tensor for the reservoir is found from the T-matrix approach for $r = 1, ..., Nc$ cavities and $r = Nc + 1, ..., N$ visco-elastic inclusions according to Jakobsen et al. (2003a,b)

$$\mathbf{C}^* = \mathbf{C}^{(0)} + \mathbf{C}_1(\mathbf{I}_4 + \mathbf{C}_1^{-1}\mathbf{C}_2)^{-1}, \quad (1)$$

$$\mathbf{C}_1 = \sum_{r=1}^{N} v^{(r)}\mathbf{t}^{(r)}, \quad (2)$$

$$\mathbf{C}_2 = \sum_{r=1}^{N}\sum_{s=1}^{N} v^{(r)}\mathbf{t}^{(r)}\mathbf{G}_d^{(rs)}\mathbf{t}^{(s)}v^{(s)}, \quad (3)$$

where $\mathbf{C}^{(0)}$ is the fourth-rank stiffness tensor of the homogeneous matrix material, $\mathbf{I}_4$ is the identity for fourth-rank tensor, $v^{(r)}$ is the volume concentration for inclusion of type r, $\mathbf{t}^{(r)}$ is the T-matrix (defined below in terms of stiffness fluctuations), $\mathbf{G}_d^{(rs)}$ is given by the strain Green's function integrated over a characteristic ellipsoid having the same symmetries as $p^{(s|r)}(\mathbf{x} - \mathbf{x}')$ which, in turn, gives the probability density for finding an inclusion of type s at point $\mathbf{x}'$ given there is an inclusion of type r at point $\mathbf{x}$. The 1^{st} order correction $\mathbf{C}_1$ depends on the concentrations, shapes and orientations of the inclusions. The 2^{nd} order correction $\mathbf{C}_2$ also takes into account the mechanical interaction between pairs of different inclusions.

The T-matrix of a single isolated cavity of type r can be written as (Jakobsen et al,. 2003b)

$$\mathbf{t}^{(r)} = (\mathbf{C}^{(r)} - \mathbf{C}^{(0)})[\mathbf{I}_4 - \mathbf{G}^{(r)}(\mathbf{C}^{(r)} - \mathbf{C}^{(0)})]^{-1}, \quad (4)$$

where $\mathbf{G}^{(r)}$ is a fourth-rank tensor depending only on $\mathbf{C}^{(0)}$ and the shape/orientation of the inclusion of type r and $\mathbf{C}^{(r)}$ is the stiffness tensor of the inclusion. If r represents a

fully fluid saturated cavity that is isolated with respect to fluid flow, $\mathbf{C}^{(r)}$ is simply related to the bulk modulus of the fluid. If r represents a dry cavity, $\mathbf{C}^{(r)}$ is equal to zero. The formulae for a single fully fluid saturated communicating cavity can be found in Appendix A, and the P velocity (V_P), S velocity (V_S) and attenuation parameters defined from the stiffness tensor in Appendix B.

To account for the two porosity scales we first model the visco-elastic properties of the micro porous material with porosity ϕ_{micro}. The micro porous material are used as spherical isolated visco-elastic inclusions with concentration v^{inc}, which implies that the effective micro porosity is $\phi^*_{micro} = \phi_{micro} v^{inc}$. Then the properties of the medium including the meso porosity ϕ_{meso} are calculated. The total porosity is thus $\phi_{tot} = \phi^*_{micro} + \phi_{meso}$. The cavities in the T-matrix approach are assumed to be of equal size (Jakobsen et al., 2003b) which implies that domains of the material with the micro pores and cracks are considered to be on the same size as meso pores and cracks. By treating the micro porous material as isolated inclusions in calculating the mesoscopic effective stiffness tensor, the micro cavities are thereby implicitly of much less size than the meso cavities.

An empirical relaxation time constant τ (Appendix A) describing pore fluid flow, must ideally be determined for each pore fluid and pore scale under consideration from velocity and attenuation measurements. However, here we have chosen to use $\tau = 10^{-7}s$ to represent the case of a porous rock saturated with water. Furthermore, we have assumed that τ can be related to fluid viscosity (Agersborg et al., 2007c)

$$\tau^{fluid1} = C_m \eta^{fluid1}, \tag{5}$$

where C_m depends on the pore structure and is independent of the pore fluids. From this expression we approximate τ for other pore fluids by (Agersborg et al., 2007c)

$$\tau^{fluid2} = \tau^{fluid1} \frac{\eta^{fluid2}}{\eta^{fluid1}}. \tag{6}$$

The porosities on each scale (see Table 3) are constant in all the models. The various pore fluid distribution models considered are summarized in Table 4. Some small attenuation just below 100 Hz is due to wave-induced fluid flow caused by the cracks with the smallest aspect ratios. Otherwise the parameters are close to constant and treated as independent of frequency. In Figure 2 density (ρ) versus V_P is plotted for the various models. The V_P varies from 2900 m/s (for model 1 with gas) to about 5000 m/s (model 2 with water). Also seen, when ϕ^*_{micro} contains water and ϕ_{meso} contains gas, the P velocities for models 3 and 4 are very similar. The same is seen when ϕ^*_{micro} is gas saturated and ϕ_{meso} is water saturated. From the V_P versus V_S plot in Figure 3 the various models and saturations are revealed. One cluster appears where ϕ_{meso} is gas saturated and three clusters appears where ϕ_{meso} is oil or water saturated. It is hard to discriminate between models where the pore fluids are various combinations of water and oil saturating ϕ^*_{micro} and ϕ_{meso} porosities. Because the S-velocity is not very sensitive to fluids other than the changes of the fluid densities, the changes in the S-velocity are mostly due to changes in the pore connection properties. The P-velocity is sensitive both to the connection properties and the saturating fluids. In Figures 2 and 3 there are indicated some general trends for the effects of altering pore fluid and the pore to pore connectivity. Decreasing connectivity leads to an increase in both P and S velocities, while the density remains unchanged. The pore fluid mainly affects the P-velocity and the density, but has a less effect on the S-velocity. However, the larger pore to pore connection the larger is the pore fluid effects on velocities.

It is important to notice that the magnitude of velocity variations with altering pore fluid depend on the pore models.

AVA signatures

For the modelling of the reflectivity and AVA properties, we consider a 2 layer model as given in Table 5. The P-P and P-S reflection coefficients are calculated both using the Zoeppritz equations (Aki and Richards, 1980) and approximate formulae valid for small incidence angles and small impedance contrasts by (Johansen et al., 2004)

$$R_{PP}(\theta) \approx R_P + G_{PP}\sin^2(\theta), \tag{7}$$

$$R_{PS}(\theta) \approx G_{PS}\sin(\theta)\cos(\theta), \tag{8}$$

where the intercept R_P and the gradients G_{PP} and G_{PS} are given by

$$R_P = \frac{1}{2}\left(\frac{\Delta\alpha}{\alpha} + \frac{\Delta\rho}{\rho}\right), \tag{9}$$

$$G_{PP} = \frac{1}{2}\left[\frac{\Delta\alpha}{\alpha} - 4\left(\frac{\beta}{\alpha}\right)^2\left(\frac{\Delta\rho}{\rho} + 2\frac{\Delta\beta}{\beta}\right)\right], \tag{10}$$

$$G_{PS} = -\frac{1}{2}\left[\left(1 + 2\frac{\beta}{\alpha}\right)\frac{\Delta\rho}{\rho} + 4\frac{\beta}{\alpha}\frac{\Delta\beta}{\beta}\right]. \tag{11}$$

Here P-P and P-S reflections are labelled PP and PS, respectively, and θ is the incidence angle of the P-wave. $\Delta\alpha = \alpha_2 - \alpha_1$ and $\alpha = \frac{1}{2}(\alpha_1 + \alpha_2)$, where α_1 and α_2 denote the P-velocity above and below the interface. Similar relations apply to the S velocities by using β and the densities by ρ.

P-P and P-S reflection coefficients for the four models are shown in Figures 4 - 7. It can be seen that the approximate P-P and P-S reflection coefficients start to deviate from the exact ones from incidence angles about 20° and 10°, respectively. From the figures we can

observe that each P-P reflection can distinguish between the considered properties of the various reservoir models. i.e. the P-P reflections of models 1 and 4 are different for all the saturation distributions, while for models 2 and 3 there are almost no difference. We see that the pore fluid saturating ϕ_{meso} provides the largest effect. In this case $\phi_{meso} > \phi^*_{micro}$ which makes a large volume effect for the fluid in the meso pores. However, the fluid within the cracks may sometimes give dominant overall velocity effects. The P-S reflections show gentle variations for low incidence angles, while for large angles it is possible to differentiate between pore fluids in ϕ^*_{micro} and ϕ_{meso} for model 3.

The intercepts of the four models are shown in Table 5. For models 1 and 3 the variations are mainly caused by altered P velocities, while for models 2 and 4 the variation are mainly due to altered density inferred by the different fluid distributions. The P-P AVA gradients for all the models are also seen to vary along with their intercepts.

P-P and P-S reflection coefficients after substitution of oil with water for an initially oil filled reservoir are shown in Figure 8. In this case the pores and cracks on both scales are initially connected (model 1). If pores start to isolate due to geochemical reactions we need to also change from one model to another. Figure 8 reveals how the P-P and P-S reflections coefficients resemble various transitions in both pore fluid and connection properties. The P-P reflections enable us to discriminate between models 1, 2 and 3. Models 3 and 4 show similar intercepts and gradients, but differ at large incidence angles and also for the P-S gradients.

V_P/V_S versus impedances both for P and S waves are shown in Figure 9. The impedances correlate to V_P/V_S for models 2 and 4 and in the case for the other models where ϕ_{meso} is gas saturated. Models which have oil or water in ϕ_{meso} appear in clusters. In the case of gas in ϕ_{meso} the clusters are more diffuse and when water also saturate ϕ^*_{micro} it is almost impossible to distinguish between models 2 and 3. A similar picture is revealed in Figure 10 displaying the P-P and P-S AVA gradients versus intercept. Furthermore we see that

the P-S AVA plot resembles Figure 3.

Discussion

The objective of this paper is to discuss possible seismic signatures of various porosity and fluid models. By imposing the dual porosity we try to mimic effects of heterogeneous fluid substitution, e.g. when only a fraction of the pore systems undergo fluid substitution. Complex pore systems, both with respect to shapes and sizes, are often seen in carbonates.

In the previous section various seismic signatures versus saturation and pore structure were modelled. In practice, AVA and AVO analyses suffer from uncertainties related to several aspects such as the signal to noise ratio, the processing sequence and structural complexity. Estimated intercepts and gradients are always uncertain to some degree. If we assume an uncertainty of, say, 0.02 for the estimated reflection coefficients, it is hard to differentiate between the various fluid models within each of the connection models (Figures 4 to 7). Also the uncertainties will overlap in models 1 to 4 in those cases where either oil or water saturates the meso pores and one of them the micro pores. However, when the fluid in the meso pores is substituted the reflectivities differ.

For a situation where water is injected in order to maintain the pore pressure in an oil column with initially well connected pores (Figure 8), the reflection signatures are different for the various fluid distributions. The figure furthermore shows that the reflection coefficients are only insensitive to the substitution process when water saturates the micro pores and where micro and meso porosity are individually connected (model 1). However, if we know that water is injected into the reservoir, unaltered reflections could indicate that the water has displaced oil in the micro pores. Similar combinations of the reflection coefficients for each model and fluid saturation (Figure 4 to 7) can be made for revealing the sensitivity of the seismic parameters in monitoring fluid substitution processes in carbonates.

Conclusions

In this modelling study we have focused on possible seismic effects of fluid substitutions in reservoirs with dual porosities on different scales. Furthermore, our modelling aims to investigate effects of various fluids in the porosity system and various connectivity properties of the pores. Such models are relevant for understanding seismic effects of complicated fluid substitution processes, as for instance when water or gas are injected into the reservoir for maintaining the pore pressure. Geochemical reactions can result in compaction, and pores or cracks that originally were well connected can become isolated with respect to fluid flow. Also when a fluid is injected into the reservoir, pores of a certain scale can be flooded before others due to capillary forces.

Our modelling indicates that the various connectivities and fluids saturating pores on different scale can reveal measurable differences in seismic parameters. Although pore fluids of similar acoustic properties may generally not give any significant attainable seismic signal, geochemical effects can alter the pore systems so the pore fluids can over time reveal different seismic expressions. This furthermore points to the necessity of understanding pore fluid and mineral interactions, both in terms of visco-elasticity and geochemistry. They do for some materials relate over time.

Acknowledgments

R.A. gratefully acknowledges Hydro for financing his Ph.D. scholarship.

References

Adam, L., Batzle, M. and Brevik, I., 2006. Gassmann's fluid substitution and shear modulus variability in carbonates at laboratory seismic and ultrasonic frequencies. *Geophysics*, 71: F173–F183.

Agersborg, R., Jakobsen, M., Ruud, B.O. and Johansen, T.A., 2007a. Effect of pore fluid pressure on the seismic response of a fractured carbonate reservoir. *Stud. Geophys. Geod.*, 51: 89–118.

Agersborg, R., Johansen, T.A., Jakobsen, M., Sothcott, J. and Best, A.I., 2007b. Effects of fluid and dual pore systems on velocities and attenuations of carbonates. *Submitted to Geophysics.*

Agersborg, R., Johansen, T.A. and Jakobsen, M., 2007c. Velocity variations in carbonate rocks due to dual porosity and wave-induced fluid flow. *Submitted to Geophys. Prospect.*

Aki, K. and Richards, P.K, 1980. Quantitative seismology: Theory and methods, W.H. Freeman and Co., San Francisco.

Anselmetti, F.S. and Eberli, G.P., 1999. The velocity-deviation log: a tool to predict pore type and permeability trends in carbonate drill holes from sonic and porosity or density logs. *AAPG Bulletin*, 83: 450–466.

Anselmetti, F.S., Luthi, S., and Eberli, G.P., 1998. Quantitative characterization of carbonate pore systems by digital image analysis. *AAPG Bulletin*, 82: 1815–1836.

Assefa, S., McCann, C. and Sothcott, J., 2003. Velocities of compressional and shear waves in limestones. *Geophys. Prospect*, 51: 1–13.

Baechle, G.T., Weger, R.J., Eberli, G.P., Massaferro, J.-L. and Sun, Y.-F., 2005. Changes of shear moduli in carbonate rocks: Implications for Gassmann applicability. *The Leading Edge*, 24: 507–510.

Batzle, M. and Wang, Z., 1992. Seismic properties of pore fluids. *Geophysics*, 57: 1396–1408.

Chatzis, I., Morrow, N.R. and Lim, H.T., 1983. Magnitude and detailed structure of residual oil saturation. *Soc. Petrol. Eng. J.*, 23: 311–330.

Choquette, P.W. and Pray, L.C., 1970. Geologic nomenclature and classification of porosity in sedimentary carbonates. *AAPG Bulletin*, 54: 207–250.

Eberli, G.P., Baechle, G.T., Anselmetti, F.S. and Incze, M.L., 2003. Factors controlling elastic properties in carbonate sediments and rocks. *The Leading Edge*, 22: 654–660.

Gassmann, F., 1951. Über die elastizität poröser medien. *Vierteljahrscrift der Naturforschende Gesellschaft in Zürich*, 96: 1–23.

Jakobsen, M., Hudson, J.A. and Johansen, T.A., 2003a. T-matrix approach to shale acoustics. *Geophys. J. Int.*, 154: 533–558.

Jakobsen, M., Johansen, T.A. and McCann, C., 2003b. The acoustic signature of fluid flow in complex porous media. *J. Appl. Geophys.*, 54: 219–246.

Johansen, T.A., Drottning, Å., Lecomte, I. and Gjøystdal, H., 2002. An approach to combined rock physics and seismic modelling of fluid substitution effects. *Geophys. Prospect.*, 50: 119–137.

Johansen, T.A., Ruud, B.O. and Jakobsen, M., 2004. Effect of grain scale alignment on seismic anisotropy and reflectivity of shales. *Geophys. Prospect.*, 52: 133–149.

Mavko, G., Mukerji, T. and Dvorkin, J., 1998. The rock physics handbook, tools for seismic analysis in porous media. *Cambridge University Press*, ISBN 0521620686: 21–24.

Rossebø, Ø.H., Brevik, I., Gholam, R.A. and Adam, L., 2005. Modeling of acoustic properties in carbonate rocks: 75th Annual International Meeting, SEG, Expanded Abstracts: 1505-1508.

Sylte, J.E., Thomas, L.K., Rhett, D.W., Bruning, D.D. and Nagle, N.B., 1999. Water induced compaction in the Ekofisk field. *SPE*, 56426: 1–11.

Wang, Z., 1997. Seismic properties of carbonate rocks. *In: Carbonate Seismology: Geophysical Developments (Eds. Palaz, I. and Marfurt, K.J.)* , 6: 29–52.

Wang, Z., 2000. The Gassmann equation revisited: Comparing laboratory data with Gassmann's prediction. *In: Seismic and acoustic velocities in reservoir rocks: Recent developments (Eds. Wang, Z. and Nur, A.)*, 3, (SEG): 8–23.

A Single fully fluid saturated communicating cavity

For a single fully fluid saturated communicating cavity of type r, the T-matrix can be expressed through a dry T-matrix with a term considering the effect of fluid flow due to the passing wave (Jakobsen et al., 2003b)

$$\mathbf{t}^{(r)} = \mathbf{t}_d^{(r)} + \frac{\Theta \mathbf{Z}^{(r)} + i\omega\tau\kappa_f \mathbf{X}^{(r)}}{1 + i\omega\gamma^{(r)}\tau}, \tag{12}$$

$$\mathbf{X}^{(r)} = \mathbf{t}_d^{(r)} \mathbf{S}^{(0)} (\mathbf{I}_2 \otimes \mathbf{I}_2) \mathbf{S}^{(0)} \mathbf{t}_d^{(r)}, \tag{13}$$

$$\mathbf{Z}^{(r)} = \mathbf{t}_d^{(r)} \mathbf{S}^{(0)} (\mathbf{I}_2 \otimes \mathbf{I}_2) \mathbf{S}^{(0)} \Big(\sum_{n=1}^{Nc} \frac{v^{(n)} \mathbf{t}_d^{(n)}}{1 + i\omega\gamma^{(n)}\tau} \Big), \tag{14}$$

$$\Theta = \kappa_f \Big\{ (1 - \kappa_f S^{(0)}_{uuvv}) \Big(\sum_{r=1}^{Nc} \frac{v^{(r)}}{1 + i\omega\gamma^{(r)}\tau} \Big) + \kappa_f \Big(\sum_{r=1}^{Nc} \frac{v^{(r)} (K_d^{(r)})_{uuvv}}{1 + i\omega\gamma^{(r)}\tau} \Big) - \frac{i k_u k_v \Gamma_{uv} \kappa_f}{\eta_f \omega} \Big\}^{-1}. \tag{15}$$

Here ω is the angular frequency of the wave, κ_f is the bulk modulus for the fluid, τ is the relaxation time constant. $\mathbf{S}^{(0)}$ is the fourth-rank compliance tensor of the matrix, $\mathbf{I}_2$ is the identity for second-rank tensor, the symbol $\otimes$ denotes the dyadic tensor product, η_f is the viscosity of the fluid, k_u and k_v are components of the wave number vector. Subscripts u and v represent summation over u and v, respectively (u,v = 1,2,3), Γ_{uv} is the permeability tensor of the reservoir,

$$\gamma^{(r)} = 1 + \kappa_f (K_d^{(r)} - S^{(0)})_{uuvv}, \tag{16}$$

and the K-tensor for the dry cavity is (Jakobsen et al., 2003b)

$$\mathbf{K}_d^{(r)} = (\mathbf{I}_4 + \mathbf{G}^{(r)} \mathbf{C}^{(0)})^{-1} \mathbf{S}^{(0)}. \tag{17}$$

Equations (12) - (15) were derived under the assumption that the cavities are of the

same scale size and that the τ-constant is independent of shape and orientation (Jakobsen et al., 2003b).

B Velocities and attenuations of the reservoir

The velocity and attenuations can be found from the effective stiffness tensor and density of the isotropic reservoir as (Jakobsen et al., 2003b)

$$V_P = \left[Re\left(\frac{C^*_{11}}{\rho^*} \right)^{-\frac{1}{2}} \right]^{-1}, \tag{18}$$

$$V_S = \left[Re\left(\frac{C^*_{44}}{2\rho^*} \right)^{-\frac{1}{2}} \right]^{-1}, \tag{19}$$

$$Q_P = \frac{Re(C^*_{11})}{Im(C^*_{11})}, \tag{20}$$

$$Q_S = \frac{Re(C^*_{44})}{Im(C^*_{44})}. \tag{21}$$

$$\tag{22}$$

List of Figures

List of Tables

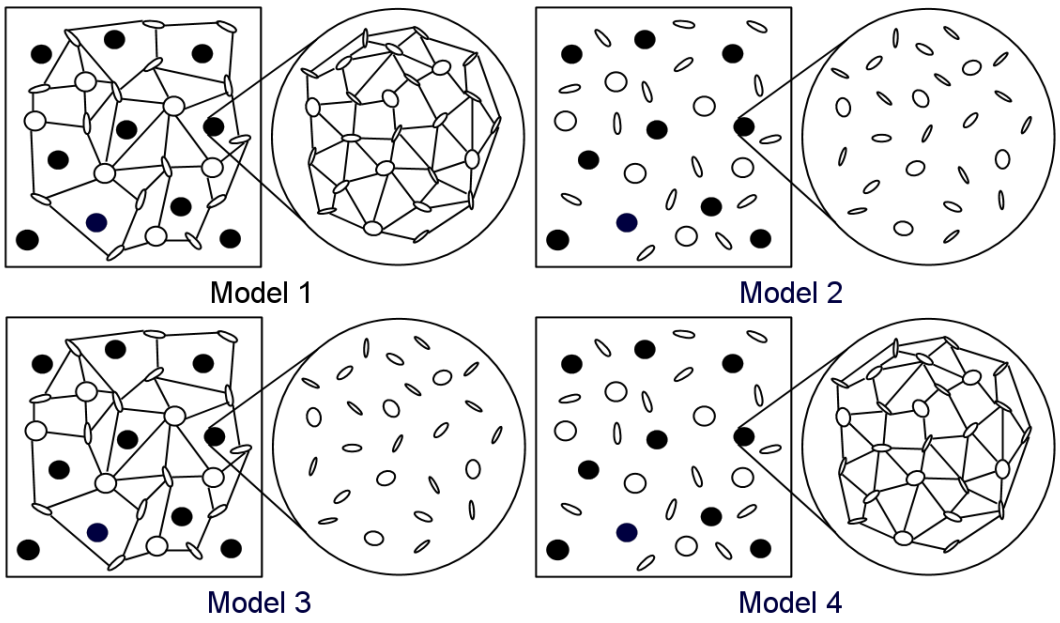

Figure 1: Conceptual sketches of the four reservoir-models where the pores exist both on micro (black inclusions) and meso scale with different connection.

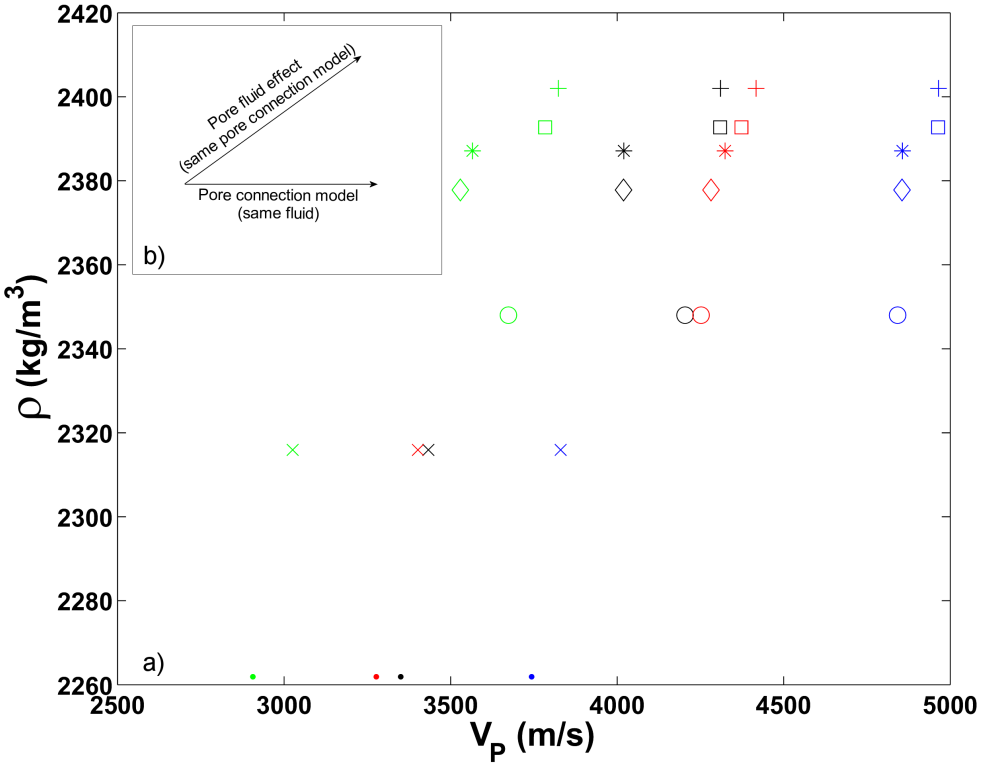

Figure 2: a) Density versus P-wave velocity for the different models. Model 1 (green); Model 2 (blue); Model 3 (black); and Model 4 (red). Gas - Gas (dot); Gas - Water (cirle); Water - Gas (x); Water - Water (cross); Water - Oil (star); Oil - Water (square); and Oil - Oil (diamond). First fluid denotes fluid saturating the micro porosity and second fluid the meso porosity. b) Schematics of pore fluid substitution trends: Magnitudes of velocity displacements depend on pore model and fluid properties.

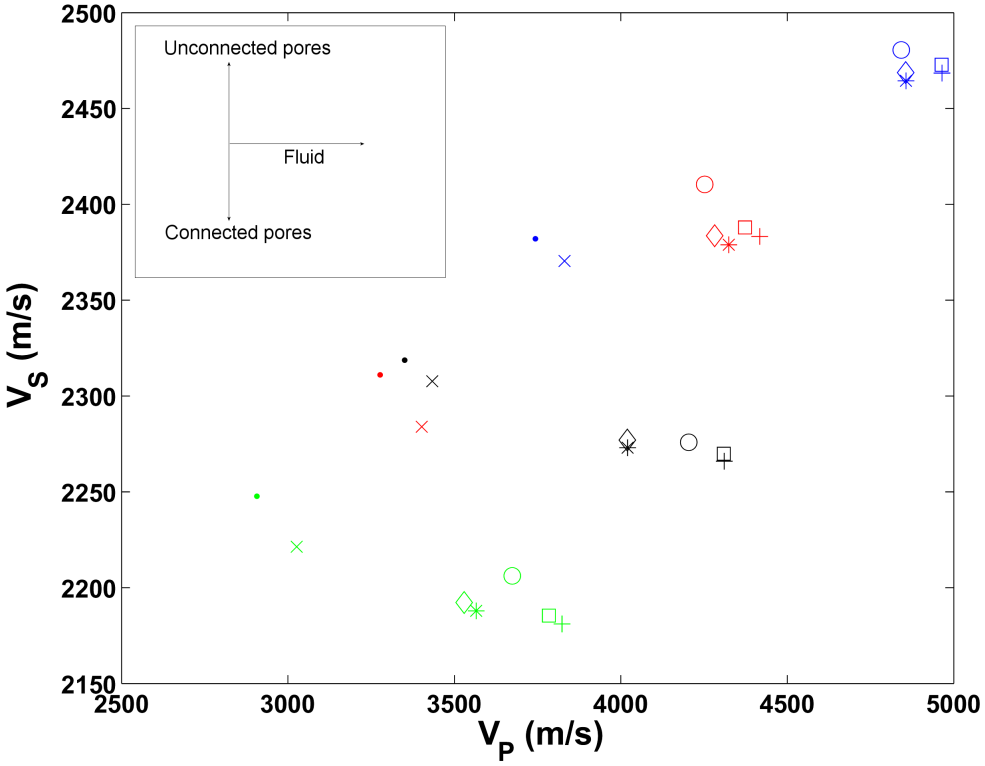

Figure 3: a) S-wave velocity versus P-wave velocity for the different models. Model 1 (green); Model 2 (blue); Model 3 (black); and Model 4 (red). Gas - Gas (dot); Gas - Water (cirle); Water - Gas (x); Water - Water (cross); Water - Oil (star); Oil - Water (square); and Oil - Oil (diamond). First fluid denotes fluid saturating the micro porosity and second fluid the meso porosity. b) Schematics of the fluid substitution trends: Magnetudes of velocity displacements depend on pore model and fluid properties.

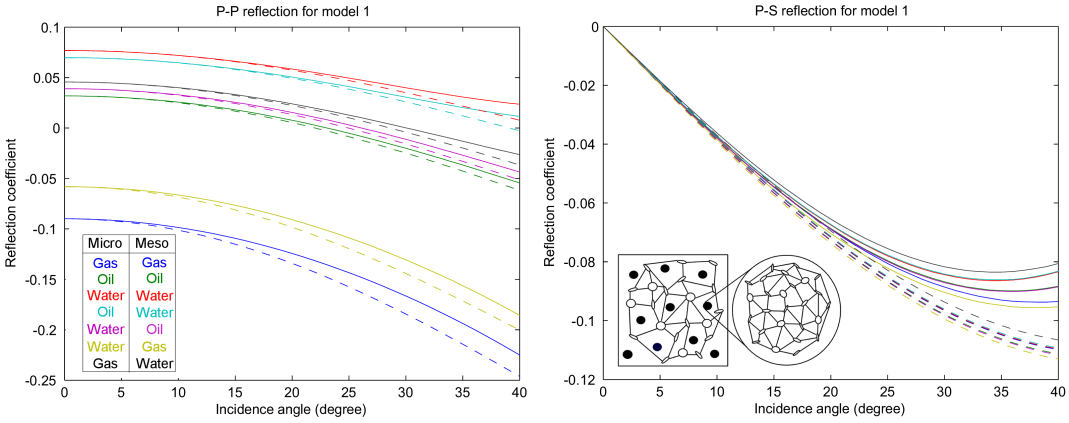

Figure 4: Reflection coefficients of model 1. Solid lines represent the exact reflection coefficients and dashed lines the approximate ones.

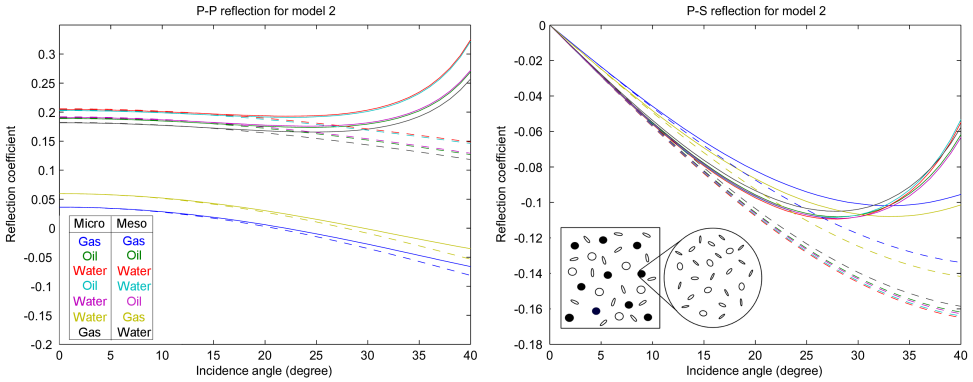

Figure 5: Reflection coefficients of model 2. Solid lines represent the exact reflection coefficients and dashed lines the approximate ones.

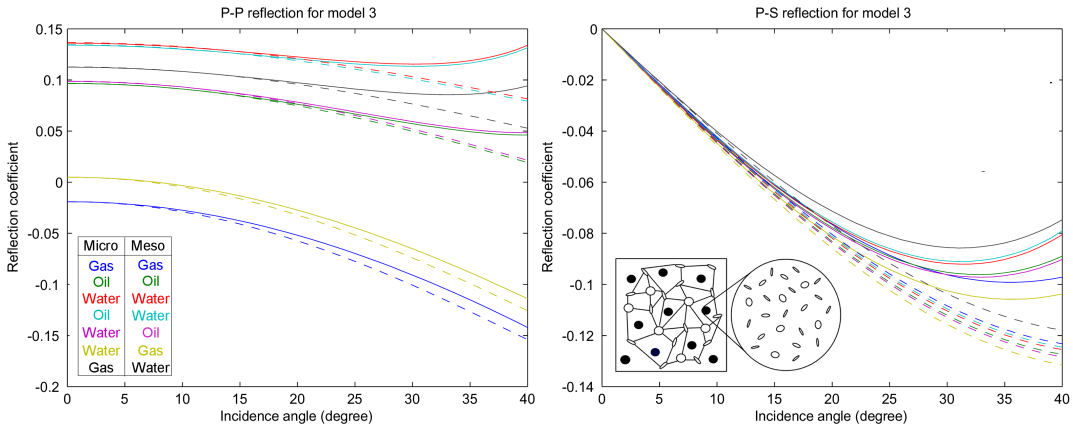

Figure 6: Reflection coefficients of model 3. Solid lines represent the exact reflection coefficients and dashed lines the approximate ones.

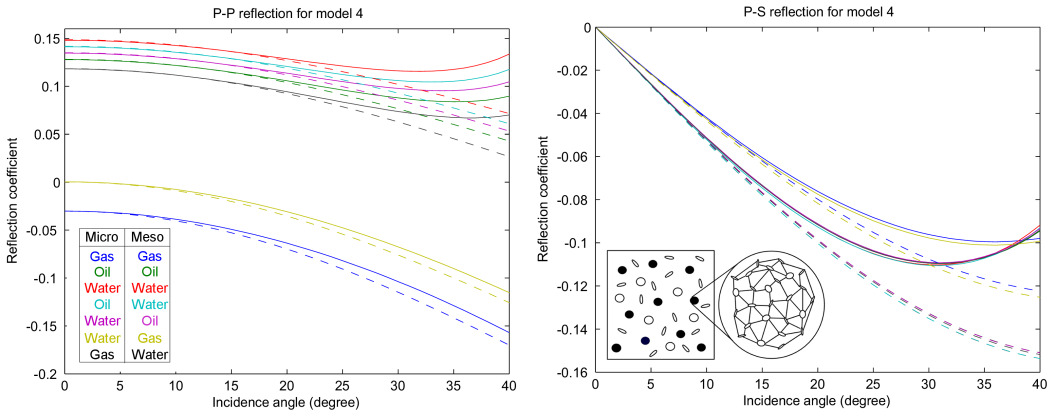

Figure 7: Reflection coefficients of model 4. Solid lines represent the exact reflection coefficients and dashed lines the approximate ones.

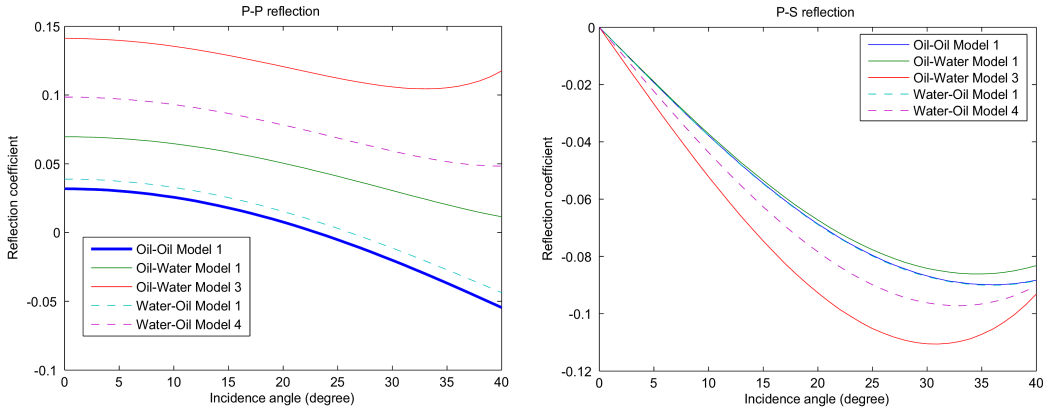

Figure 8: P-P and P-S reflections for the models with either oil or water in the different porosity systems as indicated in the figure. First and second fluid labels the fluid in the micro porosity and meso porosity, respectively. Model 1: Pores in both micro and meso scale are connected; Model 3: The micro pores are isolated and meso pores are connected; Model 4: Micro pores are connected and meso pores are isolated.

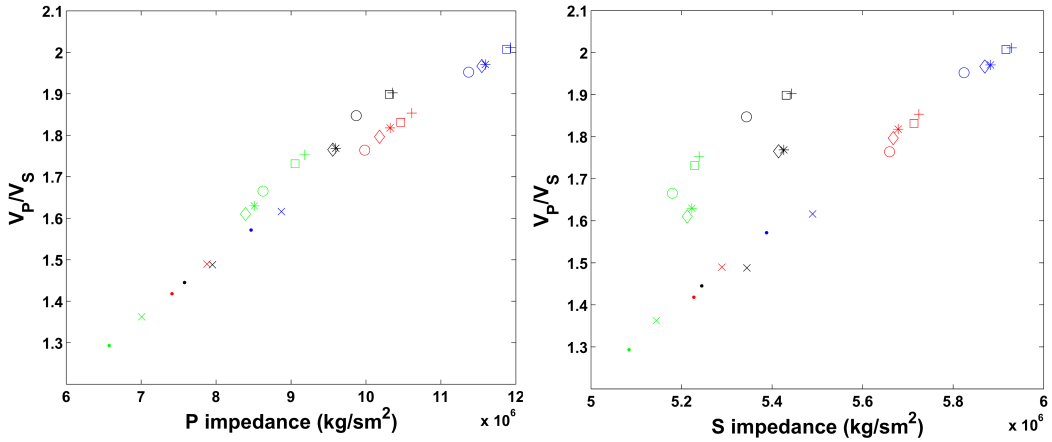

Figure 9: V_p/V_s versus impedance of the P- and S-wave. Model 1 (green); Model 2 (blue); Model 3 (black); and Model 4 (red). Gas - Gas (dot); Gas - Water (cirle); Water - Gas (x); Water - Water (cross); Water - Oil (star); Oil - Water (square); and Oil - Oil (diamond). First fluid denotes fluid saturating the micro porosity and second fluid the meso porosity.

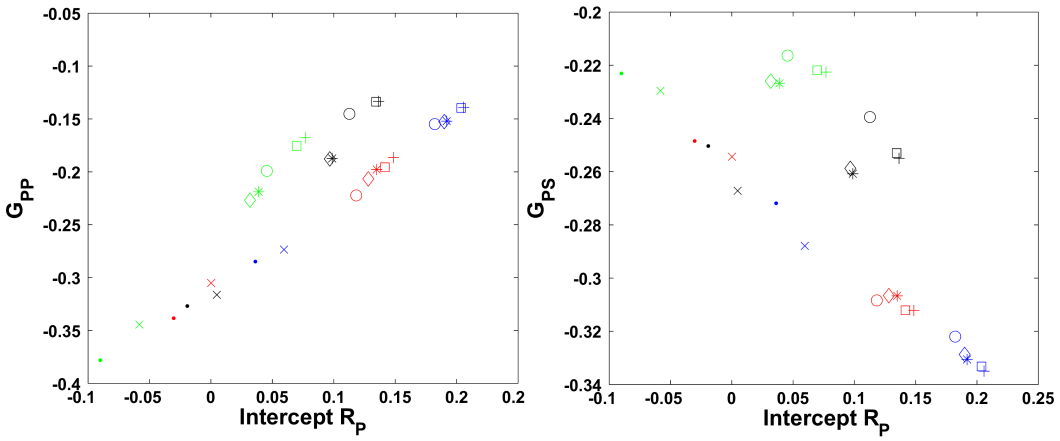

Figure 10: P-P and P-S AVA gradients versus intercept. Model 1 (green); Model 2 (blue); Model 3 (black); and Model 4 (red). Gas - Gas (dot); Gas - Water (cirle); Water - Gas (x); Water - Water (cross); Water - Oil (star); Oil - Water (square); and Oil - Oil (diamond). First fluid denotes fluid saturating the micro porosity and second fluid the meso porosity.

	Calcite	Water	Oil	Gas (Methane)
V_P (m/s)	6640	1554	1424.3	688.7
V_S (m/s)	3440			
Density (kg/m^3)	2710	989.1	854.2	206.5
Viscosity (cP)		1	6.4	0.029

Table 1: Properties of the mineral (Mavko et al., 1998) and fluid (Batzle and Wang, 1992) for temperature at 80°C and pressure at 40 MPa used in the calculations.

Micro Porosity			Meso Porosity		
α	v	ϵ	α	v	ϵ
1	$0.21^{(*)}$	0.501	1	$0.3^{(*)}$	0.0716
0.1	$0.01^{(*)}$	0.0239	1	$0.099^{(*)}$	0.0236
0.001	0.00042	$0.1^{(*)}$	0.01	$0.01^{(*)}$	0.2387
0.0005	0.00021	$0.1^{(*)}$	0.001	0.00042	$0.1^{(*)}$
0.0001	0.00004	$0.1^{(*)}$			

Table 2: Concentration (v), aspect ratio (α) and crack density ($\epsilon = \frac{3v}{4\pi\alpha}$) of the micro and meso porosity.$^{(*)}$ The value used in the calculation (v or ϵ). The micro porosity was incorporated in the mesoscopic calculation as spherical inclusions with concentration equal to 0.3.

ϕ_{micro} (%)	v^{inc} (%)	ϕ^*_{micro} (%)	ϕ_{meso} (%)	ϕ_{tot} (%)	$\phi_{micro(relative)}$ (%)
23	30	6.9	11	17.9	38.5

Table 3: The porosities of the different scales. $\phi^*_{micro} = \phi_{micro} v^{inc}$ and $\phi_{micro(relative)} = (\phi^*_{micro}/\phi_{tot}) \cdot 100$.

Micro	Meso
Gas	Gas
Oil	Oil
Water	Water
Oil	Water
Water	Oil
Water	Gas
Gas	Water

Table 4: Pore fluid distributions in the two pore scales.

Model	Saturation	V_P (m/s)	V_S (m/s)	ρ (kg/m^3)	R_P	G_{PP}	G_{PS}
1	Gas - Gas	2906.6	2247.7	2261.9	-0.0900	-0.3781	-0.2231
1	Gas - Water	3673.7	2206.1	2348.0	0.0455	-0.1991	-0.2164
1	Water - Gas	3026.1	2221.3	2315.9	-0.0582	-0.3444	-0.2296
1	Water - Water	3823.3	2181.1	2402.0	0.0768	-0.1676	-0.2226
1	Water - Oil	3565.6	2187.9	2387.1	0.0389	-0.2189	-0.2268
1	Oil - Water	3783.9	2185.4	2392.7	0.0697	-0.1755	-0.2219
1	Oil - Oil	3529.4	2192.2	2377.8	0.0318	-0.2268	-0.2260
2	Gas - Gas	3743.3	2382.0	2261.9	0.0362	-0.2848	-0.2719
2	Gas - Water	4842.3	2480.5	2348.0	0.1822	-0.1549	-0.3220
2	Water - Gas	3830.6	2370.4	2315.9	0.0595	-0.2735	-0.2879
2	Water - Water	4964.9	2468.5	2402.0	0.2057	-0.1390	-0.3350
2	Water - Oil	4856.7	2464.4	2387.1	0.1919	-0.1521	-0.3306
2	Oil - Water	4963.6	2472.8	2392.7	0.2037	-0.1396	-0.3332
2	Oil - Oil	4855.6	2468.7	2377.8	0.1899	-0.1526	-0.3287
3	Gas - Gas	3350.6	2318.7	2261.9	-0.0192	-0.3269	-0.2504
3	Gas - Water	4203.8	2275.8	2348.0	0.1127	-0.1452	-0.2395
3	Water - Gas	3433.5	2307.7	2315.9	0.0048	-0.3163	-0.2672
3	Water - Water	4310.5	2266.0	2402.0	0.1364	-0.1334	-0.2550
3	Water - Oil	4020.1	2273.0	2387.1	0.0987	-0.1874	-0.2608
3	Oil - Water	4309.4	2269.9	2392.7	0.1344	-0.1337	-0.2530
3	Oil - Oil	4019.4	2277.0	2377.8	0.0967	-0.1878	-0.2588
4	Gas - Gas	3277.0	2311.0	2261.9	-0.0303	-0.3384	-0.2485
4	Gas - Water	4251.9	2410.4	2348.0	0.1183	-0.2223	-0.3084
4	Water - Gas	3402.0	2283.9	2315.9	0.0002	-0.3051	-0.2544
4	Water - Water	4417.3	2383.2	2402.0	0.1485	-0.1865	-0.3122
4	Water - Oil	4324.4	2378.9	2387.1	0.1349	-0.1978	-0.3067
4	Oil - Water	4373.2	2387.9	2392.7	0.1416	-0.1956	-0.3121
4	Oil - Oil	4281.9	2383.6	2377.8	0.1281	-0.2067	-0.3066

Table 5: Properties of the reservoir and AVA parameters for the reservoir with different connections and saturations. Model 1: Cavities in both micro and meso scale are connected; Model 2: Pores in both micro and meso scale are isolated; Model 3: Micro pores are isolated and meso pores are connected; Model 4: Micro pores are connected and meso pores are isolated. First fluid in the table denotes the fluid in the micro porosity and second fluid denotes the fluid in the meso porosity. The properties of the overburden: $V_P = 3500$ m/s,$V_S = 1900$ m/s and $\rho = 2250$ kg/m^3.

9 Summary and perspective

The aim of this Ph.D. study is to characterize the acoustic properties of carbonate rocks with use of a recent developed visco-elastic effective medium theory, the T-matrix approach. The study involves predictions of the acoustic properties by considering different porosity models, pore sizes and types, crack and fracture orientations together with pore fluid saturation and pressure. By using dual porosity models with different pore types at two scales, it is shown in paper 1 that large scattering of the velocities observed for carbonates with equal porosity and mineralogy can be modelled. Also, when predicting velocity and attenuation for ultrasonic experiments of calcite core plugs in paper 2, the dual porosity model where the porosity was divided into a dry and a fluid filed part, is able to reproduce the measurements, both for the dried and saturated core plugs. In paper 3, the effect of large fractures is studied and it was shown how these fractures can cause attenuation due to wave induced fluid flow even at seismic frequencies. It is difficult to differentiate between the reflection coefficients for the various reservoir model from paper 1 with an overburden of shale. However, by considering different cross plots of the properties extracted from the reflection coefficients, in paper 4, the different reservoir models with various fluid distributions was revealed. In the modelling, the characteristic pore types of carbonates were depicted as cracks, compliant and stiffer pores.

Considering the porosity at different scales and how the pores are connected can account for many observed acoustic properties of carbonate rocks. Further work in this direction would be to account for diagenetic processes into the T-matrix approach. Also in this study we did not take into consideration any chemical interaction between the rock mineral, which can be chemical unstable, and the pore fluid. It would be interesting to study this with respect to be able to predict e.g. the observed shear modulus weakening due to softening of the rock frame.

A Derivation of the effective stiffness tensor

The derivation of the effective stiffness tensor of the T-matrix approach is taken from Jakobsen et al. (2003a). By assuming an elastic sample with a complex microstructure occupies a large spherical region Ω, the stress tensor $\boldsymbol{\sigma}(\mathbf{x})$ and strain tensor $\boldsymbol{\epsilon}(\mathbf{x})$ at point $\mathbf{x}$, under a deformation with infinitesimal strain, can be related by the linear transformation

$$\boldsymbol{\sigma}(\mathbf{x}) = \mathbf{C}(\mathbf{x})\boldsymbol{\epsilon}(\mathbf{x}). \tag{13}$$

Here $\mathbf{C}(\mathbf{x})$ is the local tensor of elastic constants. The complex microstructure of the sample is reflected in the fact that $\mathbf{C}(\mathbf{x})$ varies with $\mathbf{x}$ in a random manner, on a scale that is small compared with all other length-scales. For the heterogeneous material as a whole, similar relation in terms of the average stress tensor $\langle\boldsymbol{\sigma}(\mathbf{x})\rangle$ and strain tensor $\langle\boldsymbol{\epsilon}(\mathbf{x})\rangle$ gives (Jakobsen at al., 2003a)

$$\langle\boldsymbol{\sigma}(\mathbf{x})\rangle = \mathbf{C}^*\langle\boldsymbol{\epsilon}(\mathbf{x})\rangle. \tag{14}$$

By assuming that the material is statistical homogeneous, which means that any sufficiently large subregions of Ω is statistical identical with the whole specimen, all ensemble-averaged material quantities such as $\mathbf{C}^*$ are independent of position.

By introducing an integral equation for the strain field

$$\boldsymbol{\epsilon}(\mathbf{x}) = \frac{1}{2}\left\{\nabla\mathbf{u}(\mathbf{x}) + [\nabla\mathbf{u}(\mathbf{x})]^T\right\}, \tag{15}$$

under a known displacement $\mathbf{u}(\mathbf{x})$ of the surface $\partial\Omega$ of the sample Ω:

$$\mathbf{u}(\mathbf{x}) = \mathbf{U}(\mathbf{x}), \quad \mathbf{x} \in \partial\Omega. \tag{16}$$

We can evaluate the tensor of the effective elastic constants from Equation (14). With equilibrium equation

$$\nabla \cdot \boldsymbol{\sigma}(\mathbf{x}) = 0, \tag{17}$$

and since the material is homogeneous on the macroscopic scale, we can write

$$\mathbf{C}(\mathbf{x}) = \mathbf{C}^{(0)} + \delta\mathbf{C}(\mathbf{x}), \tag{18}$$

where $\delta\mathbf{C}(\mathbf{x})$ is the fluctuation of $\mathbf{C}(\mathbf{x})$ from a quantity $\mathbf{C}^{(0)}$ which is uniform in space. From Equations (13), (17), and (18) we now have

$$\nabla \cdot [\mathbf{C}^{(0)}\boldsymbol{\epsilon}(\mathbf{x})] = -\nabla \cdot [\delta\mathbf{C}(\mathbf{x})\boldsymbol{\epsilon}(\mathbf{x})]. \tag{19}$$

From this differential equation there can be derived an integral equation for the strain field

$$\boldsymbol{\epsilon}(\mathbf{x}) = \boldsymbol{\epsilon}^{(0)} + \int_{\Omega} d\mathbf{x}' \mathbf{G}^{(0)}(\mathbf{x} - \mathbf{x}')\delta\mathbf{C}(\mathbf{x}')\boldsymbol{\epsilon}(\mathbf{x}'), \tag{20}$$

where $\boldsymbol{\epsilon}^{(0)}$ is the strain tensor due to the boundary displacements in a material with properties given by $\mathbf{C}^{(0)}$. $\mathbf{G}^{(0)}(\mathbf{x})$ is the strain Green's tensor function for a translation-invariant system where the components are given by

$$G^{(0)}_{ijkl}(\mathbf{x}) = -\frac{1}{4}\left[\frac{g^{(0)}_{ik}(\mathbf{x})}{\partial x_j \partial x_l} + \frac{g^{(0)}_{jk}(\mathbf{x})}{\partial x_i \partial x_l} + \frac{g^{(0)}_{il}(\mathbf{x})}{\partial x_j \partial x_k} + \frac{g^{(0)}_{jl}(\mathbf{x})}{\partial x_i \partial x_k}\right]. \tag{21}$$

Here $g^{(0)}_{ik}(\mathbf{x})$ is a component of the displacement Green's tensor function $\mathbf{g}^{(0)}(\mathbf{x})$ which vanishes at the boundary of Ω

$$C^{(0)}_{ijkl}\frac{\partial^2 g^{(0)}_{km}(\mathbf{x})}{\partial x_j \partial x_l} + \delta_{im}\delta(\mathbf{x}) = 0, \quad \mathbf{g}^{(0)}(\mathbf{x}) = 0 \text{ if } \mathbf{x} \in \partial\Omega. \tag{22}$$

Following Zeller and Dederichs (1973), and introducing a fourth-rank tensor field $\mathbf{T}(\mathbf{x})$ which, when contracted with $\boldsymbol{\epsilon}^{(0)}$ on the right, yields the stress difference $\delta\mathbf{C}(\mathbf{x})\boldsymbol{\epsilon}(\mathbf{x})$

$$\delta\mathbf{C}(\mathbf{x})\boldsymbol{\epsilon}(\mathbf{x}) = \mathbf{T}(\mathbf{x})\boldsymbol{\epsilon}^{(0)}. \tag{23}$$

$\boldsymbol{\epsilon}(\mathbf{x})$ is linearly dependent on $\boldsymbol{\epsilon}^{(0)}$ through the boundary condition (Equation (16)), so $\mathbf{T}(\mathbf{x})$ depends only on the material properties and not on $\boldsymbol{\epsilon}(\mathbf{x})$ or $\boldsymbol{\epsilon}^{(0)}$. Similar to Equation (20), we find the integral equation for $\mathbf{T}(\mathbf{x})$ by using Equation (23) in Equation (20) and write

$$\boldsymbol{\epsilon}(\mathbf{x}) = \boldsymbol{\epsilon}^{(0)} + \int_{\Omega} d\mathbf{x}' \mathbf{G}^{(0)}(\mathbf{x}-\mathbf{x}')\mathbf{T}(\mathbf{x}')\boldsymbol{\epsilon}^{(0)}. \tag{24}$$

By multiplying Equation (24) with $\delta\mathbf{C}(\mathbf{x})$ from the left and using Equation (23) again, we get

$$\mathbf{T}(\mathbf{x})\boldsymbol{\epsilon}^{(0)} = \delta\mathbf{C}(\mathbf{x})\boldsymbol{\epsilon}^{(0)} + \delta\mathbf{C}(\mathbf{x}) \int_{\Omega} d\mathbf{x}' \mathbf{G}^{(0)}(\mathbf{x}-\mathbf{x}')\mathbf{T}(\mathbf{x}')\boldsymbol{\epsilon}^{(0)}. \tag{25}$$

The elements T_{ijkl} of $\mathbf{T}$ is chosen to be symmetric in (i,j) and (k,l) and, since $\boldsymbol{\epsilon}^{(0)}$ may be chosen to be an arbitrary symmetric matrix, it follows that

$$\mathbf{T}(\mathbf{x}) = \delta\mathbf{C}(\mathbf{x}) + \delta\mathbf{C}(\mathbf{x}) \int_{\Omega} d\mathbf{x}' \mathbf{G}^{(0)}(\mathbf{x}-\mathbf{x}')\mathbf{T}(\mathbf{x}'). \tag{26}$$

The tensor field $\mathbf{T}(\mathbf{x})$ specifies the 'transitions' out of the reference field $\boldsymbol{\epsilon}^{(0)}$ and gives the complete information about the strain tensor field distribution $\boldsymbol{\epsilon}(\mathbf{x})$ in the micro-inhomogeneous material, provided that we can solve the integral equation (Equation (26)).

For finding the effective elastic constants in terms of $\mathbf{T}$, we get from Equations (13) and (18)

$$\langle\boldsymbol{\sigma}\rangle = \mathbf{C}^{(0)}\langle\boldsymbol{\epsilon}\rangle + \langle\delta\mathbf{C}\boldsymbol{\epsilon}\rangle. \tag{27}$$

By combining Equations (23) and (27) we get

$$\langle \boldsymbol{\sigma} \rangle = \mathbf{C}^{(0)} \langle \boldsymbol{\epsilon} \rangle + \langle \mathbf{T} \rangle \boldsymbol{\epsilon}^{(0)}. \tag{28}$$

From Equation (24) it is clear that

$$\langle \boldsymbol{\epsilon} \rangle = \boldsymbol{\epsilon}^{(0)} + \bar{\mathbf{G}} \langle \mathbf{T} \rangle \boldsymbol{\epsilon}^{(0)}, \tag{29}$$

where

$$\bar{\mathbf{G}} = \int_{\Omega} d\mathbf{x}' \mathbf{G}^{(0)}(\mathbf{x} - \mathbf{x}'), \quad \mathbf{x} \in \Omega, \tag{30}$$

is a constant tensor (Eshelby, 1957). Equation (29) gives $\boldsymbol{\epsilon}^{(0)}$ in terms of $\langle \boldsymbol{\epsilon} \rangle$

$$\boldsymbol{\epsilon}^{(0)} = \left(\mathbf{I} + \bar{\mathbf{G}} \langle \mathbf{T} \rangle \right)^{-1} \langle \boldsymbol{\epsilon} \rangle, \tag{31}$$

where $\mathbf{I}$ is the identity tensor. Equations (14), (28), and (31), imply that

$$\mathbf{C}^{*} = \mathbf{C}^{(0)} + \langle \mathbf{T} \rangle \left(\mathbf{I} + \bar{\mathbf{G}} \langle \mathbf{T} \rangle \right)^{-1}. \tag{32}$$

Now having obtained a formal exact solution for the case of local elasticity in terms of the T-matrix for the material, we consider a material in which the elastic constant $\mathbf{C}(\mathbf{x})$ is piecewise constant, specifically we consider media with inclusions that are either embedded in a homogeneous matrix material or else make up a granular aggregate. The population of inclusions is divided into families of inclusions having the same shape/orientation and stiffness tensor $\mathbf{C}^{(r)}$, labelled by $r = 1, 2, ..., F$. Dry cavities may formally be treated as inclusions having vanishing stiffnesses (see Nemat-Nasser and Hori, 1993; Ponte Castaneda and Willis, 1995). We assume that there are $n^{(r)}$ inclusions of type r, occupying identical

regions $\Omega_\alpha^{(r)}$ of the space Ω, centred at random points $\mathbf{x}_\alpha^{(r)}$ $(\alpha = 1, ..., n^{(r)})$. Denote by $\theta^{(r)}(\mathbf{x})$ the characteristic function of the domain $\Omega_\alpha^{(r)}$ (that is, $\theta^{(r)}(\mathbf{x}-\mathbf{x}_\alpha^{(r)}) = 1$, if $\mathbf{x} \in \Omega_\alpha^{(r)}$ and 0 otherwise). It follows that the fluctuation $\delta\mathbf{C}(\mathbf{x})$ may be decomposed as

$$\delta\mathbf{C}(\mathbf{x}) = \sum_{r=1}^{F}\sum_{\alpha=1}^{n^{(r)}} \delta\mathbf{C}_\alpha^{(r)}(\mathbf{x}), \tag{33}$$

$$\delta\mathbf{C}_\alpha^{(r)}(\mathbf{x}) = \delta\mathbf{C}^{(r)}\theta^{(r)}(\mathbf{x}-\mathbf{x}_\alpha^{(r)}), \tag{34}$$

$$\delta\mathbf{C}^{(r)} = \mathbf{C}^{(r)} - \mathbf{C}^{(0)}. \tag{35}$$

A decomposition of the T-matrix for the material, which is analogous with that of $\delta\mathbf{C}(\mathbf{x})$ in Equation (33), is given by

$$\mathbf{T}(\mathbf{x}) = \sum_{r=1}^{F}\sum_{\alpha=1}^{n^{(r)}} \mathbf{T}_\alpha^{(r)}(\mathbf{x}), \tag{36}$$

$$\mathbf{T}_\alpha^{(r)}(\mathbf{x}) = \mathbf{T}(\mathbf{x})\theta^{(r)}(\mathbf{x}-\mathbf{x}_\alpha^{(r)}). \tag{37}$$

Equations (26), (33), and (36), imply that the $\mathbf{T}_\alpha^{(r)}(\mathbf{x})$ must satisfy

$$\mathbf{T}_\alpha^{(r)}(\mathbf{x}) = \delta\mathbf{C}_\alpha^{(r)}(\mathbf{x}) + \delta\mathbf{C}_\alpha^{(r)}(\mathbf{x})\int_\Omega d\mathbf{x}'\mathbf{G}^{(0)}(\mathbf{x}-\mathbf{x}')\sum_{s,\beta}\mathbf{T}_\beta^{(s)}(\mathbf{x}'). \tag{38}$$

If we let $\mathbf{t}_\alpha^{(r)}(\mathbf{x})$ denote the solution of the integral equation

$$\mathbf{t}_\alpha^{(r)}(\mathbf{x}) = \delta\mathbf{C}_\alpha^{(r)}(\mathbf{x}) + \delta\mathbf{C}_\alpha^{(r)}(\mathbf{x})\int_\Omega d\mathbf{x}'\mathbf{G}^{(0)}(\mathbf{x}-\mathbf{x}')\mathbf{t}_\alpha^{(r)}(\mathbf{x}'), \tag{39}$$

then we may rewrite expression (38) for $\mathbf{T}_\alpha^r(\mathbf{x})$ exactly as

$$\mathbf{T}_\alpha^{(r)}(\mathbf{x}) = \mathbf{t}_\alpha^{(r)}(\mathbf{x}) + \mathbf{t}_\alpha^{(r)}(\mathbf{x})\int_\Omega d\mathbf{x}'\mathbf{G}^{(0)}(\mathbf{x}-\mathbf{x}')\sum_{s,\beta}\mathbf{T}_\beta^{(s)}(\mathbf{x}')(1-\delta_{rs}\delta_{\alpha\beta}), \tag{40}$$

A single iteration of Equation (40) yields

$$\mathbf{T}_{\alpha}^{(r)}(\mathbf{x}) \approx \mathbf{t}_{\alpha}^{(r)}(\mathbf{x}) + \mathbf{t}_{\alpha}^{(r)}(\mathbf{x}) \int_{\Omega} d\mathbf{x}' \mathbf{G}^{(0)}(\mathbf{x}-\mathbf{x}') \sum_{s,\beta} \mathbf{t}_{\beta}^{(s)}(\mathbf{x}')(1-\delta_{rs}\delta_{\alpha\beta}). \tag{41}$$

Now assuming that the inclusions are ellipsoidal in shape, we can find the T-matrix for a single inclusion. The transition tensor $\mathbf{t}_{\alpha}^{(r)}(\mathbf{x})$ satisfies (see Equation (23))

$$\delta\mathbf{C}_{\alpha}^{(r)}(\mathbf{x})\boldsymbol{\epsilon}_{\alpha}^{(r)}(\mathbf{x}) = \mathbf{t}_{\alpha}^{(r)}(\mathbf{x})\boldsymbol{\epsilon}^{(0)}, \tag{42}$$

where $\boldsymbol{\epsilon}_{\alpha}^{(r)}(\mathbf{x})$ is the strain field for a single inclusion of type r embedded in the homogeneous matrix. If $\boldsymbol{\epsilon}_{\alpha}^{(r)}(\mathbf{x})$ is constant within the inclusion, then $\mathbf{t}_{\alpha}^{(r)}(\mathbf{x})$ must also be; and it is zero outside, so we may write

$$\mathbf{t}_{\alpha}^{(r)}(\mathbf{x}) = \mathbf{t}^{(r)}\theta^{(r)}(\mathbf{x}-\mathbf{x}_{\alpha}^{(r)}), \tag{43}$$

where $\mathbf{t}^{(r)}$ is a constant tensor. Inserting this into the integral equation (Equation (39)), we get

$$\begin{aligned} \mathbf{t}^{(r)}\theta^{(r)}(\mathbf{x}-\mathbf{x}_{\alpha}^{(r)}) &= \delta\mathbf{C}^{(r)}\theta^{(r)}(\mathbf{x}-\mathbf{x}_{\alpha}^{(r)}) \\ &+ \delta\mathbf{C}^{(r)}\theta^{(r)}(\mathbf{x}-\mathbf{x}_{\alpha}^{(r)}) \int_{\Omega} d\mathbf{x}' \mathbf{G}^{(0)}(\mathbf{x}-\mathbf{x}')\mathbf{t}^{(r)}\theta^{(r)}(\mathbf{x}'-\mathbf{x}_{\alpha}^{(r)}). \end{aligned} \tag{44}$$

Integrating over Ω we get

$$\mathbf{t}^{(r)} = \delta\mathbf{C}^{(r)} + \delta\mathbf{C}^{(r)}\mathbf{G}^{(r)}\mathbf{t}^{(r)}, \tag{45}$$

or

$$\mathbf{t}^{(r)} = (\mathbf{I} - \delta\mathbf{C}^{(r)}\mathbf{G}^{(r)})^{-1}\delta\mathbf{C}^{(r)}, \tag{46}$$

where

$$\mathbf{G}^{(r)} = \frac{1}{|\Omega^{(r)}|} \int_{\Omega^{(r)}} d\mathbf{x} \int_{\Omega^{(r)}} d\mathbf{x}' \mathbf{G}^{(0)}(\mathbf{x}-\mathbf{x}'), \tag{47}$$

and $\Omega^{(r)}$ is the region of an inclusion of type r centred at the origin. Clearly, $\mathbf{G}^{(r)}$ is a contant tensor, and its components can be evaluated by using the formulae discussed in Appendix B.

From Equations (36), (41), and (43), we find that

$$\mathbf{T}(\mathbf{x}) \approx \mathbf{T}_1(\mathbf{x}) + \mathbf{T}_2(\mathbf{x}), \tag{48}$$

where

$$\mathbf{T}_1(\mathbf{x}) = \sum_r \mathbf{t}^{(r)} \bar{\theta}^{(r)}(\mathbf{x}), \tag{49}$$

$$\begin{aligned} \mathbf{T}_2(\mathbf{x}) &= \sum_r \sum_s \mathbf{t}^{(r)} \int_\Omega d\mathbf{x}' \mathbf{G}^{(0)}(\mathbf{x}-\mathbf{x}') \bar{\theta}^{(r)}(\mathbf{x}) \bar{\theta}^{(s)}(\mathbf{x}') \mathbf{t}^{(s)} \\ &- \sum_{r,\alpha} \mathbf{t}^{(r)} \theta^{(r)}(\mathbf{x}-\mathbf{x}_\alpha^{(r)}) \int_\Omega d\mathbf{x}' \mathbf{G}^{(0)}(\mathbf{x}-\mathbf{x}') \theta^{(r)}(\mathbf{x}'-\mathbf{x}_\alpha^{(r)}) \mathbf{t}^{(r)}, \end{aligned} \tag{50}$$

and

$$\bar{\theta}^{(r)}(\mathbf{x}) = \sum_\alpha \theta^{(r)}(\mathbf{x}-\mathbf{x}_\alpha^{(r)}), \tag{51}$$

is the indicator function for phase r.

In order to evaluate the effective elastic constants from Equation (32), or from some equation implied by it, we need to construct an equivalent $\langle \mathbf{T} \rangle$. From Equation (48) we get

$$\langle \mathbf{T} \rangle \approx \langle \mathbf{T}_1 \rangle + \langle \mathbf{T}_2 \rangle. \tag{52}$$

Equation (49) yields

$$\langle \mathbf{T}_1 \rangle = \sum_r \mathbf{t}^{(r)} v^{(r)}, \tag{53}$$

where

$$v^{(r)} = \langle \bar{\theta}^{(r)}(\mathbf{x}) \rangle, \tag{54}$$

is the relative volume concentration of phase r. From Equation (50) we get

$$\langle \mathbf{T}_2 \rangle = \sum_r \sum_s \mathbf{t}^{(r)} \int_\Omega d\mathbf{x}' \mathbf{G}^{(0)}(\mathbf{x}-\mathbf{x}') \langle \bar{\theta}^{(r)}(\mathbf{x}) \bar{\theta}^{(s)}(\mathbf{x}') \rangle \mathbf{t}^{(s)} - \sum_r \mathbf{t}^{(r)} \tilde{\mathbf{G}}^{(r)} \mathbf{t}^{(r)}, \tag{55}$$

where

$$\tilde{\mathbf{G}}^{(r)} = \sum_\alpha \frac{1}{|\Omega|} \int_\Omega d\mathbf{x} \theta^{(r)}(\mathbf{x}-\mathbf{x}_\alpha^{(r)}) \int_\Omega d\mathbf{x}' \mathbf{G}^{(0)}(\mathbf{x}-\mathbf{x}') \theta^{(r)}(\mathbf{x}'-\mathbf{x}_\alpha^{(r)}), \tag{56}$$

and we have replaced the ensemble average of the second term on the right-hand side of Equation (50) by its volume average. Equations (47) and (56) imply that

$$\tilde{\mathbf{G}}^{(r)} = v^{(r)} \mathbf{G}^{(r)}, \tag{57}$$

since

$$v^{(r)} = \sum_\alpha \frac{|\Omega^{(r)}|}{|\Omega|} = n^{(r)} \frac{|\Omega^{(r)}|}{|\Omega|}. \tag{58}$$

The exact expression (32) for the effective elastic constant $\mathbf{C}^*$ can be rewritten exactly as

$$(\delta \mathbf{C}^*)^{-1} = \langle \mathbf{T} \rangle^{-1} + \bar{\mathbf{G}}, \tag{59}$$

where

$$\delta \mathbf{C}^* = \mathbf{C}^* - \mathbf{C}^{(0)}. \tag{60}$$

Multiplying Equation (59) with $\langle \mathbf{T}_1 \rangle$ from the left and using the standard rule for inversion of tensor inner products, we get

$$\langle \mathbf{T}_1 \rangle (\delta \mathbf{C}^*)^{-1} = \left[\langle \mathbf{T} \rangle \langle \mathbf{T}_1 \rangle^{-1} \right]^{-1} + \langle \mathbf{T}_1 \rangle \bar{\mathbf{G}}. \tag{61}$$

Combining Equations (52) and (61) we get

$$\langle \mathbf{T}_1 \rangle (\delta \mathbf{C}^*)^{-1} \approx \left[\mathbf{I} + \langle \mathbf{T}_2 \rangle \langle \mathbf{T}_1 \rangle^{-1} \right]^{-1} + \langle \mathbf{T}_1 \rangle \bar{\mathbf{G}}. \tag{62}$$

If we now assume that

$$||\langle \mathbf{T}_2 \rangle \langle \mathbf{T}_1 \rangle^{-1}|| < 1, \tag{63}$$

where $||\cdot||$ denotes a suitable tensor norm, then it follows from Equation (62) that $\delta \mathbf{C}^* \approx \delta \mathbf{C}_T^*$ where

$$\langle \mathbf{T}_1 \rangle (\delta \mathbf{C}_T^*)^{-1} = \mathbf{I} - \langle \mathbf{T}_2 \rangle \langle \mathbf{T}_1 \rangle^{-1} + \langle \mathbf{T}_1 \rangle \bar{\mathbf{G}}. \tag{64}$$

After some tensor algebra, we can rewrite this expression for the effective material parameters:

$$\delta \mathbf{C}_T^* = \langle \mathbf{T}_1 \rangle (\mathbf{I} - \langle \mathbf{T}_1 \rangle^{-1} \mathbf{X})^{-1}, \tag{65}$$

where

$$\mathbf{X} = \langle \mathbf{T}_2 \rangle - \langle \mathbf{T}_1 \rangle \bar{\mathbf{G}} \langle \mathbf{T}_1 \rangle. \tag{66}$$

From Equations (30), (53), (54), (55), (57), and (66), we get

$$\mathbf{X} = \sum_r \sum_s \mathbf{t}^{(r)} \langle \mathbf{A}^{(rs)} \rangle \mathbf{t}^{(s)} - \sum_r \mathbf{t}^{(r)} v^{(r)} \mathbf{G}^{(r)} \mathbf{t}^{(r)}, \tag{67}$$

where

$$\langle \mathbf{A}^{(rs)} \rangle = \int_\Omega d\mathbf{x}' \mathbf{G}^{(0)}(\mathbf{x} - \mathbf{x}') \left[\langle \bar{\theta}^{(r)}(\mathbf{x}) \bar{\theta}^{(s)}(\mathbf{x}') \rangle - \langle \bar{\theta}^{(r)}(\mathbf{x}) \rangle \langle \bar{\theta}^{(s)}(\mathbf{x}') \rangle \right], \tag{68}$$

depends only on $\mathbf{C}^{(0)}$ and the stochastic geometry of the microstructure. $\langle \mathbf{A}^{(rs)} \rangle$ can be written as (Ponte Castaneda and Willis, 1995; Jakobsen et al., 2003a)

$$\langle \mathbf{A}^{(rs)} \rangle = \delta_{rs} v^{(r)} \mathbf{G}^{(s)} - v^{(r)} v^{(s)} \mathbf{G}_d^{(rs)}, \tag{69}$$

where

$$\mathbf{G}_d^{(rs)} = \int_{\Omega_d^{(rs)}} d\mathbf{x}' \mathbf{G}^{(0)}(\mathbf{x} - \mathbf{x}'), \quad \mathbf{x} \in \Omega_d^{(rs)}, \tag{70}$$

is a spatially invariant tensor since $\Omega_d^{(rs)}$ represents an ellipsoid having the same symmetry as $p^{(s|r)}(\mathbf{z} - \mathbf{z}')$ which, in turn, represents the probability density for finding an inclusion of type s centred at point $\mathbf{z}'$ given that there is an inclusion of type r centred at point $\mathbf{z}$. Since $p^{(s|r)}(\mathbf{z} - \mathbf{z}') = p^{(r|s)}(\mathbf{z}' - \mathbf{z})$ it follows that $\mathbf{G}_d^{(rs)} = \mathbf{G}_d^{(sr)}$. We have assumed that the inclusions do not overlap because an ellipsoid of type r is surrounded by a 'security' ellipsoid $\Omega_d^{(rs)}$, in the sense that $p^{(s|r)}(\mathbf{z}'') = 0$ if $\mathbf{z}'' \in \Omega_d^{(rs)}$. From Equations (67) and (69) we find that

$$\mathbf{X} = -\sum_r \sum_s \mathbf{t}^{(r)} v^{(r)} \mathbf{G}_d^{(rs)} \mathbf{t}^{(s)} v^{(s)}. \tag{71}$$

From equations (53), (60), (65), and (71), have a new expression for the effective elastic constants

$$\mathbf{C}^* = \mathbf{C}^{(0)} + \sum_r \mathbf{t}^{(r)} v^{(r)} \left[\mathbf{I} + \left(\sum_s \mathbf{t}^{(s)} v^{(s)} \right)^{-1} \sum_u \sum_v \mathbf{t}^{(u)} v^{(u)} \mathbf{G}_d^{(uv)} \mathbf{t}^{(v)} v^{(v)} \right]^{-1}, \tag{72}$$

setting

$$\mathbf{C}_1 = \sum_r v^{(r)} \mathbf{t}^{(r)}, \tag{73}$$

$$\mathbf{C}_2 = \sum_r \sum_s v^{(r)} \mathbf{t}^{(r)} \mathbf{G}_d^{(rs)} \mathbf{t}^{(s)} v^{(s)}, \tag{74}$$

we can express the effective stiffness tensor as

$$\mathbf{C}^* = \mathbf{C}^{(0)} + \mathbf{C}_1 (\mathbf{I} + \mathbf{C}_1^{-1} \mathbf{C}_2)^{-1}. \tag{75}$$

B The tensors $\mathbf{G}^{(r)}$ and $\mathbf{G}_d^{(rs)}$

Jakobsen et al. (2003a,b) show that $\mathbf{G}^{(r)}$ for an ellipsoidal inclusion can be written as

$$G_{pqrs}^{(r)} = -\frac{1}{4}(E_{pqrs}^{(r)} + E_{pqsr}^{(r)} + E_{qprs}^{(r)} + E_{qpsr}^{(r)}), \tag{76}$$

where

$$E_{pqrs}^{(r)} = \int_0^{\pi} d\theta \sin\theta \int_0^{2\pi} d\phi D_{qs}^{-1}(\mathbf{k}) k_p k_r A^{(r)}(\theta, \phi), \tag{77}$$

and $D_{qs}^{-1}(\mathbf{k})$ is the invers matrix of the Fourier transform of the displacement Green's function, and

$$A^{(r)}(\theta, \phi) = \frac{1}{\pi |\Omega^{(r)}|} \int_0^{\infty} dk k^2 \int_{\Omega^{(r)}} dx e^{-i\mathbf{k}\cdot\mathbf{x}} \int_{\Omega^{(r)}} dx' e^{-i\mathbf{k}\cdot\mathbf{x}'} \tag{78}$$

where k, θ and ϕ are the spherical coordinates in $\mathbf{k}$ space, and k_i the Cartesian components of $\mathbf{k}$. $A^{(r)}$ represent a shape/orientation factor independent of the elastic constant.

The tensor $\mathbf{G}^{(r)}$ can also be expressed by the Eshelby (1957) tensor of an ellipsoid, $\mathbf{S}^{(r)}$, given by (Torquato, 2002)

$$\mathbf{G}^{(r)} = -\mathbf{S}^{(r)}\mathbf{S}^{(0)}. \tag{79}$$

In the case a matrix material containing spheroidal inclusions with semiaxies $a_1^{(r)} = a_2^{(r)} = a_r$ and $a_3^{(r)} = b_r$ and whose symmetry axis is aligned in the x_3-direction, the Eshelby's tensor (which generally is given in terms of elliptic integrals) can be evaluated analytically (Mura, 1982). If the matrix material is isotropic then the components of $S_{ijkl}^{(r)}$ are given by (Torquato, 2002)

$$S_{1111}^{(r)} = S_{2222}^{(r)} = \frac{3}{8(1-\nu)} \frac{\alpha_r^2}{\alpha_r^2 - 1} + \frac{1}{4(1-\nu)} \left[1 - 2\nu - \frac{9}{4(\alpha_r^2 - 1)}\right] q, \tag{80}$$

$$S^{(r)}_{3333} = \frac{1}{2(1-\nu)}\left\{1-2\nu+\frac{3\alpha_r^2-1}{\alpha_r^2-1}-\left[1-2\nu+\frac{3\alpha_r^2}{\alpha_r^2-1}\right]q\right\}, \tag{81}$$

$$S^{(r)}_{1122} = S^{(r)}_{2211} = \frac{1}{4(1-\nu)}\left\{\frac{\alpha_r^2}{2(\alpha_r^2-1)}-\left[1-2\nu+\frac{3}{4(\alpha_r^2-1)}\right]q\right\}, \tag{82}$$

$$S^{(r)}_{1133} = S^{(r)}_{2233} = \frac{1}{2(1-\nu)}\left\{\frac{-\alpha_r^2}{\alpha_r^2-1}+\frac{1}{2}\left[\frac{3\alpha_r^2}{\alpha_r^2-1}-(1-2\nu)\right]q\right\}, \tag{83}$$

$$S^{(r)}_{3311} = S^{(r)}_{3322} = \frac{1}{2(1-\nu)}\left\{2\nu-1-\frac{1}{\alpha_r^2-1}+\left[1-2\nu+\frac{3}{2(\alpha_r^2-1)}\right]q\right\}, \tag{84}$$

$$S^{(r)}_{1212} = \frac{1}{4(1-\nu)}\left\{\frac{\alpha_r^2}{2(\alpha_r^2-1)}+\left[1-2\nu-\frac{3}{4(\alpha_r^2-1)}\right]q\right\}, \tag{85}$$

$$S^{(r)}_{1313} = S^{(r)}_{2323} = \frac{1}{4(1-\nu)}\left\{1-2\nu-\frac{\alpha_r^2+1}{\alpha_r^2-1}-\frac{1}{2}\left[1-2\nu-\frac{3(\alpha_r^2+1)}{\alpha_r^2-1}\right]q\right\} \tag{86}$$

where ν is the Poisson ratio of the matrix, $\alpha_r^2 = b_r/a_r$ is the aspect ratio f the rth spheroid, and q is given by

$$q = \frac{\alpha_r}{(1-\alpha_r^2)^{3/2}}[\cos^{-1}\alpha_r - \alpha_r(1-\alpha_r^2)^{1/2}], \tag{87}$$

when $\alpha_r \leq 1$.

For an sphere ($\alpha_r =$ and $q = 3/2$) the components of the Eshelby's tensor simplifies even more

$$S^{(r)}_{ijkl} = \frac{5\nu-1}{15(1-\nu)}\delta_{ij}\delta_{kl} - \frac{4-5\nu}{15(1-\nu)}(\delta_{ik}\delta_{jl}+\delta_{il}\delta_{jk}) \tag{88}$$

The above expressions for the $\mathbf{G}^{(r)}$ tensor can also be used to evaluate the $\mathbf{G}_d^{(rs)}$ tensor and the tensor $\mathbf{G}^{(r)}$ is identical to $-\mathbf{P}^{(r)}$, where $\mathbf{P}^{(r)}$ is a tensor well known for the works of Willis and his associates (see e.g. Ponte Castaneda and Willis, 1995).

C Derivation of the equations for a single communicating cavity

The derivation is taken from Jakobsen and Hudson (2003) and Jakobsen et al. (2003b). The t-matrix in Appendix A can be expressed with a K-tensor which relates the strain, $\epsilon^{(r)}$, within an inclusion to the imposed stress at infinity (Jakobsen et al., 2003b; Jakobsen and Hudson, 2003)

$$\epsilon^{(r)} = \mathbf{K}^{(r)}\sigma^{(0)}, \tag{89}$$

where the K-tensor can be written as (Jakobsen et al., 2003b)

$$\mathbf{K}^{(r)} = [\mathbf{I}_4 - \mathbf{G}^{(r)}(\mathbf{C}^{(r)} - \mathbf{C}^{(0)})]^{-1}\mathbf{S}^{(0)}, \tag{90}$$

such that the t-matrix is

$$\mathbf{t}^{(r)} = (\mathbf{C}^{(r)} - \mathbf{C}^{(0)})\mathbf{K}^{(r)}\mathbf{C}^{(0)}. \tag{91}$$

By linear superposition (Jakobsen et al., 2003b), the strain inside a fully saturated cavity of type r with pore fluid pressure $p_f^{(r)}$, under imposed stress $\sigma^{(0)}$, is given by the strain of the same dry cavity minus the strain within a similarly shaped and oriented cavity with hydrostatic stress $\mathbf{I}_2 p_f^{(r)}$ applied both at infinity and inside the cavity. $\mathbf{I}_2$ is the second-rank identity tensor. By this argument and Equations (89) and (90) we get (Jakobsen et al., 2003b; Jakobsen and Hudson, 2003)

$$\mathbf{K}^{(r)}\boldsymbol{\sigma}^{(0)} = \mathbf{K}_d^{(r)}(\boldsymbol{\sigma}^{(0)} + \mathbf{I}_2 p_f^{(r)}) - \mathbf{S}^{(0)}\mathbf{I}_2 p_f^{(r)}. \tag{92}$$

Here $\mathbf{K}_d^{(r)}$ is the dry response of the K-tensor.

Following Hudson et al. (1996), we require that the fluid mass in an arbitrary volume is conserved and that the average flow of fluid is regulated by Darcy's law (Jakobsen et al.,

2003b)

$$\frac{\partial m_f}{\partial t} = \nabla \left(\frac{\rho_f}{\eta_f} \Gamma \cdot \nabla p_f \right). \tag{93}$$

Here m_f is the total fluid mass, ρ_f is the fluid mass density, η_f is the viscosity of the fluid, Γ is a second-rank tensor of permeability parameters and p_f is the average fluid pressure. The fluid pressure and density of the r'th cavity are related by (Hudson et al., 1996; Jakobsen et al., 2003b; Jakobsen and Hudson, 2003)

$$\frac{\rho_0}{\rho_f^{(r)}} = 1 - \frac{p_f^{(r)}}{\kappa_f}, \tag{94}$$

where ρ_0 is the density of the unstressed fluid and κ_f is the fluid bulk modulus. The mass flow out of the r'th set of cavities is assumed to be controlled by the expression (Hudson et al., 1996; Jakobsen et al., 2003b; Jakobsen and Hudson, 2003)

$$\frac{\partial(\rho_f^{(r)} \bar{v}^{(r)})}{\partial t} = \frac{v^{(n)} \rho_0}{\kappa_f \tau} \left(p_f^{(r)} - p_f \right), \tag{95}$$

where τ is the relaxation time constant.

The changes in the porosity can be be found from Equations (89) and (92) (Jakobsen et al., 2003b; Jakobsen and Hudson, 2003)

$$\frac{\bar{v}^{(r)} - v^{(r)}}{v^{(r)}} = (K_d)_{uupq} \left(\sigma_{pq}^{(0)} + \delta_{pq} p_f^{(r)} \right) - S_{uupq}^{(0)} \delta_{pq} p_f^{(r)}. \tag{96}$$

Here $v^{(r)}$ is the unstressed porosity of the r'th cavity set.

By introducing a second-rank tensor Ψ which relate the average fluid pressure and applied stress by (Jakobsen et al., 2003b; Jakobsen and Hudson, 2003)

$$p_f = \Psi \sigma^{(0)}, \tag{97}$$

and assuming the propagating plane wave has frequency ω, we find from Equations (94) - (97) that (Jakobsen et al., 2003b; Jakobsen and Hudson, 2003)

$$\Psi^{(r)} = \frac{\Psi - i\omega\tau\kappa_f \mathbf{I}_2 \mathbf{K}_d^{(r)}}{1 + i\omega\gamma^{(r)}\tau}, \tag{98}$$

$$\gamma^{(r)} = 1 + \kappa_f \left(K_d^{(r)} - S^{(0)} \right)_{uuvv}, \tag{99}$$

to first order in $p_f^{(r)}/\kappa_f$ and $\left(\bar{v}^{(r)} - v^{(r)}\right)/v^{(r)}$. After some manipulation the above equations can be written as (Jakobsen et al. 2003b; Jakobsen and Hudson, 2003)

$$\Psi = -\Theta \sum_{r=1}^{N_c} \frac{v^{(r)} \mathbf{I}_2 \mathbf{K}_d^{(r)}}{1 + i\omega\gamma^{(r)}\tau}, \tag{100}$$

where

$$\Theta = \kappa_f \left[(1 - \kappa_f S^{(0)}_{uuvv}) \sum_{r=1}^{N_c} \frac{v^{(r)}}{1 + i\omega\gamma^{(r)}\tau} + \kappa_f \sum_{r=1}^{N_c} \frac{v(r) \left(K_d^{(r)} \right)_{uuvv}}{1 + i\omega\gamma^{(r)}\tau} - \frac{i k_u k_v \Gamma_{uv} \kappa_f}{\eta_f \omega} \right]^{-1}. \tag{101}$$

Here k_u and k_v are components of the wave number vector. The summation is over all the cavities ($r = 1, ..., N_c$). From these equations the t-matrix for a single communicating cavity (listed in papers 1-4) is given as

$$\mathbf{t}^{(r)} = \mathbf{t}_d^{(r)} + \frac{\Theta \mathbf{Z}^{(r)} + i\omega\tau\kappa_f \mathbf{X}^{(r)}}{1 + i\omega\gamma^{(r)}\tau}, \tag{102}$$

$$\mathbf{X}^{(r)} = \mathbf{t}_d^{(r)} \mathbf{S}^{(0)} (\mathbf{I}_2 \otimes \mathbf{I}_2) \mathbf{S}^{(0)} \mathbf{t}_d^{(r)}, \tag{103}$$

$$\mathbf{Z}^{(r)} = \mathbf{t}_d^{(r)} \mathbf{S}^{(0)} (\mathbf{I}_2 \otimes \mathbf{I}_2) \mathbf{S}^{(0)} \Big(\sum_{n=1}^{Nc} \frac{v^{(n)} \mathbf{t}_d^{(n)}}{1 + i\omega\gamma^{(n)}\tau} \Big). \tag{104}$$

References

Adam, L., Batzle, M. and Brevik, I. 2006. Gassmann's fluid substitution and shear modulus variability in carbonates at laboratory seismic and ultrasonic frequencies. *Geophysics*, **71**, F173–F183.

Agersborg, R., Jakobsen, M., Ruud, B.O. and Johansen, T.A. 2007a. Effect of pore fluid pressure on the seismic response of a fractured carbonate reservoir. *Studia Geophysica et Geodaetica*, **51**, 89-118.

Anselmetti, F.S. and Eberli, G.P. 1999. The velocity-deviation log: A tool to predict pore type and permeability trends in carbonate drill holes from sonic and porosity or density logs. *AAPG Bulletin*, **83**, 450–466.

Anselmetti, F.S., Luthi, S. and Eberli, G.P. 1998. Quantitative characterization of carbonate pore systems by digital image analysis. *AAPG Bulletin*, **82**, 1815–1836.

Assefa, S., McCann, C. and Sothcott, J. 2003. Velocities of compressional and shear waves in limestones. *Geophysical Prospecting*, **51**, 1–13.

Avseth, P., Mukerji, T. and Mavko, G. 2005. Quatitative seismic interpretation. *Cambridge University Press*, ISBN 100521816017.

Baechle, G.T., Weger, R.J., Eberli, G.P., Massaferro, J.-L. and Sun, Y.-F. 2005. Changes of shear moduli in carbonate rocks: Implications for Gassmann applicability. *The Leading Edge*, **24**, 507–510.

Batzle, M.L., Han, D.-H. and Hofmann, R. 2006. Fluid mobility and frequency-dependent seismic velocity - Direct measurment. *Geophysics*, **71**, N1-N9.

Biot, M.A. 1956a. Theory of propagation of elastic waves in a fluid saturated porous solid I. Low frequency range. *The Journal of the Acoustical Society of America*, **28**, 168–178.

Biot, M.A. 1956b. Theory of propagation of elastic waves in a fluid saturated porous solid II. High frequency range. *The Journal of the Acoustical Society of America*, **28**, 179–191.

Chapman, M. 2003. Frequency-dependent aniotropy due to meso-scale fractures in the presence of equant porosity. *Geophysical Prospecting*, **51**, 369–379.

Chapman, M., Zatsepin, S.V., and Crampin, S. 2002. Derivation of a microstructural poroelastic model. *Geophysical Journal International*, **151**, 427–451.

Castagna, J.P. 1993. AVO analysis - turtorial and review. In offset dependent reflectivity - theory and practice of AVO analysis, Investigations in geophysics, No 8 (eds. J.P. Castagna and M. Backus). *SEG*, ISBN 1560800593, 3-36.

Choquette, P.W. and Pray, L.C. 1970. Geologic nomenclature and classification of porosity in sedimentary carbonates. *AAPG Bulletin*, **54**, 207–250.

Dunham, R.J., 1962. Classification of carbonate rocks according to texture. In: Classification of carbonate rocks - a symposium, AAPG Memoir 1 (ed. W.E.Ham). *AAPG*, ISBN 0891812768, 108-121.

Eberli, G.P., Baechle, G.T., Anselmetti, F.S. and Incze, M. 2003. Factors controlling elastic properties in carbonate sediments and rocks. *The Leading Edge*, **22**, 654–660.

Eshelby, J.D. 1957. The determination of the elastic field of an ellipsoidal inclusion, and related problems. *Proceedings of the Royal Society of London*, **A 241**, 376-396.

Gassmann, F. 1951. Über die elastizität poröser medien. *Viereljahrscrift der Naturforschende Gesellschaft in Zürich*, **96**, 1–23.

Hay, S.J., Hall, J., Simmons, G. and Russell, M.J. 1988. Sealed microcracks in the Lewisian of NW Scotland: A record of 2 billion years of fluid circulation. *Journal of the Geological Society*, **145**, 819–830.

Hudson, J.A. 1988. Seismic wave propagation through material containing partially saturated cracks. *Geophysical Journal*, **92**, 33–37.

Hudson, J.A., Liu, E. and Crampin, S. 1996. The mechanical properties of materials with interconnected cracks and pores. *Geophysical Journal International*, **124**, 105–112.

Jakobsen, M. and Hudson, J.A. 2003. Visco-elastic waves in rock-like composites. *Studia Geophysica et Geodaetica*, **47**, 793–826.

Jakobsen, M., Hudson, J.A. and Johansen, T.A. 2003a. T-matrix approach to shale acoustics. *Geophysical Journal International*, **154**, 533–558.

Jakobsen, M., Johansen, T.A. and McCann, C. 2003b. The acoustic signature of fluid flow in complex porous media. *Journal of Applied Geophysics*, **54**, 219–246.

Jakobsen, M. and Johansen, T.A. 2005. The effect of drained and undrained loading on visco-elastic waves in rock-like composites. *International Journal of Solids and Structures*, **42**, 1597–1611.

Kuster, G.T. and Toksöz, M.N. 1974. Velocity and attenuation of seismic waves in two-phase media: Part I. Theoretical formulations. *Geophysics*, **39**, 587–606.

Mavko, G., Mukerji, T. and Dvorkin, J. 1998. The rock physics handbook, tools for seismic analysis in porous media. *Cambridge University Press*, ISBN 0521620686.

Mavko, G.M. and Nur, A. 1979. Wave attenuation in partially saturated rocks. *Geophysics*, **44**, 161–178.

Mura, T. 1982. Micromechanics of defects in solids. *Nijhoff, Zoetermeer, Netherlands*, ISBN 9024725607.

Nemat-Nasser, S. and Hori, M. 1993. Micromechanics: overall properties of heterogeneous materials. *Applied Mathematics and Mechanics*, Vol. 37, North-Holland, New York, ISBN 0444898816.

Nur, A. and Simmons, G. 1969. The effect of saturation on velocity in low porosity rock. *Earth and Planetary Science Letters*, **7**, 183–193.

O'Connell R. and Budiansky, B. 1977. Viscoelastic properties of fluid-saturated cracked solids. *Journal of Geophysical Research*, **82**, 5719-5735.

Pointer, T., Liu, E. and Hudson J.A. 2000. Seismic wave propagation in cracked porous media. *Geophysical Journal International*, **142**, 199–231.

Ponte Castaneda, P. and Willis, J.R. 1995. The effect of spatial distribution on the effective behaviour of composite materials and cracked media. *Journal of the Mechanics and Physics of Solids*, **43**, 1919–1951.

Rossebø, Ø.H., Brevik, I., Gholam, R.A. and Adam, L. 2005. Modeling of acoustic properties in carbonate rocks. *75th Annual International Meeting, SEG, Expanded Abstracts*, 1505–1508.

Sayers, C.M. 2002. Fluid-dependent shear-wave splitting in fractured media. *Geophysical Prospecting*, **50**, 393-401.

Tod, S. 2001. The effect on seismic waves of interconnected nearly aligned cracks. *Geophysical Journal International*, **146**, 249–263.

Toksöz, M.N., Cheng, C.H. and Timur A. 1976. Velocity of seismic waves in porous rocks. *Geophysics*, **41**, 621–645.

Torquato, S. 2002. Random heterogeneous materials: Microstructure and macroscopic properties. *Springer Verlag, New York*, ISBN 0387951679.

Tucker, M.E. 2001. Sedimentary petrology. *Blackwell Science Ltd*, ISBN 0632057351.

Walsh, J.B. 1965. Seismic attenuation in partially saturated rock. *Journal of Geophysical Research*, **100**, 15407–15424.

Wang, Z. 1997. Seismic properties of carbonate rocks. In: Carbonate seismology, Geophysical Developments Vol 6 (eds.: I. Palaz and K.J. Marfurt). 29–52.

Wang, Z., 2000. The Gassmann equation revisited: Comparing laboratory data with Gassmann's prediction. In: Seismic and acoustic velocities in reservoir rocks, Recent developments Vol 3 (eds. Z. Wang, and A.Nur). SEG, 8–23.

Wyllie, M.R.J., Gregory, A.R. and Gardner, L.W. 1956. Elastic wave velocities in heterogeneous and porous media. *Geophysics*, **21**, 41-70.

Zeller, R. and Dederich, P.H. 1977. Elastic constants of polycrystals. *Phys. Status Solidi, B Basic Res.*, **55**, 831–843.